Electron Dynamics of Interatomic Coulombic Electron Capture in Artificial and Real Atoms

Inaugural Dissertation
to obtain the academic degree
Doctor rerum naturalium (Dr. rer. nat.)

submitted to the
Department of Biology, Chemistry and Pharmacy
of Freie Universität Berlin

by

Axel Molle

2019

1. Gutachter:	Dr. Annika Bande Junior Research Group on Theoretical Chemistry Department Locally Sensitive and Time-Resolved Spectroscopy Helmholtz-Zentrum Berlin für Materialien und Energie GmbH Hahn-Meitner-Platz 1, 14109 Berlin, Germany
2. Gutachter:	Prof. Dr. Beate Paulus Institute of Chemistry and Biochemistry – Physical and Theoretical Chemistry Freie Universität Berlin Arnimallee 22, 14195 Berlin
Disputation am:	6. November 2019

To Mimi, curious adventurer
and Cinderella, captain of the High Seas,
with gratitude for their patient support to
Annika, Beate and Katharina
and with love to Justine,
Ellen and David.

Electron Dynamics of Interatomic Coulombic Electron Capture in Artificial and Real Atoms

Axel Molle

Abstract

Interatomic coulombic electron capture is a non-local process involving the environment-assisted attachment of a free electron with implied consequences for various systems. Starting from the established numerical model of quantum confinements in a nanowire, this dissertation sets out to deduce model-independent hypotheses for future investigations of theoretical or experimental nature and develops a generalised adaptation of the model to test whether the effective-two-electron treatment suffices to successfully capture a free electron in the experimentally motivated system of a barium (II) cation engulfed in a Bose-Einstein-condensate of neutral rubidium atoms.

Appearing associated to differing electronic states of the confinement region, two subprocesses can contrast in spatial preferences and resonant energies. For the investigated range of parameters, the energy levels of these associated states suggest to provide a starting point for a more comprehensive description beyond the particular parameters of an individual model. A rather simple electric dipole-dipole coupled adaptation of the model is then able to successfully show environment assisted electron attachment to a barium (II) cation aided by a surrounding cloud of ultracold rubidium atoms in typical experimental conditions.

Zusammenfassung

Der interatomare Coulombische Elektroneneinfang ist ein nicht-lokaler Prozess die umweltgestützte Anlagerung eines freien Elektrons mit impliziten Konsequenzen für verschiedene Systeme. Von einem etablierten Modell für Quantenpunktpaare in Nanodrähten ausgehend, entwickelt diese Dissertation modellunabhängige Hypothesen für zukünftige Untersuchungen theoretischer oder experimenteller Natur und entwickelt eine verallgemeinerte Abwandlung des Modells zum Test der Limitationen einer Beschreibung durch effektive zwei-Elektronen-Näherung im experimentell motivierten System eines Barium-II-Kations in ein Bose-Einstein-Kondensat neutraler Rubidiumatome. Zwei Unterprozesse treten in Verbindung mit unterschiedlichen elektronischen Zuständen des einfangenden Potenzialtopfes auf und können sich voneinander abgrenzende räumliche Präferenzen und Resonanzenergien zeigen. Für den untersuchten Parameterbereich erscheinen die assoziierten Energieniveaus einen vielversprechenden Ausgangspunkt für eine aufschlussreichere Beschreibung jenseits der spezifischen Parameter des einzelnen Modells darzustellen. Eine eher vereinfachte elektrische Dipol-Dipol-gekoppelte Anpassung des etablierten Modells ist dann erfolgreich in der Lage eine Elektronenanlagerung an ein Barium (II) Kation durch interatomare Coulombwechselwirkung zu Elektronen einer umgebende Wolke ultrakalter Rubidiumatome unter typischen experimentelle Bedingungen zu durchlaufen.

Contents

I Motivation 10

1 Relevance of the Interatomic Electron Capture 11
- 1.1 Dissociative Electron Attachment in Biological Systems . . . 12
- 1.2 Commercial Electronics on the Scale of Human DNA . . . 13
- 1.3 Individual Ions in Clouds of Ultracold Atoms . . . 15

2 Available Investigative Methods 17

II Theory 19

3 Theoretical Background 19
- 3.1 General Concepts and Notation . . . 19
  - 3.1.1 Scattering Quantum States . . . 21
- 3.2 The Quantum Harmonic Oscillator . . . 23
  - 3.2.1 Gaussian Functions . . . 24
  - 3.2.2 Characteristic Scales of Length, Momentum and Energy . . . 25
- 3.3 The Gaussian Potential Well . . . 25
- 3.4 Asymmetric Pairs of Gaussian Wells . . . 32
- 3.5 The Hydrogen Problem in Various Coordinate Systems . . . 33
  - 3.5.1 Atomic Hartree and Rydberg units . . . 34
  - 3.5.2 Normalised Wavefunctions . . . 36

4 Non-Interactive Dynamics 38
- 4.1 A Free Electron (Gaussian Wavepacket) . . . 38
  - 4.1.1 Energy Distribution Density . . . 40
  - 4.1.2 Time Evolution in one Dimension . . . 40
- 4.2 Free Electrons in three Dimensions . . . 42
  - 4.2.1 Energy Distribution Density . . . 43

5 A Model of Ions in Ultracold Atoms 46
- 5.1 A long-range Interaction . . . 47

III Applications 50

6 Artificial Atoms in Nanoelectronics 52
- 6.1 Computational Details . . . 53
- 6.2 Results . . . 56
  - 6.2.1 Electrodynamic Impulse and Interatomic Coulombic Decay . . . 56
  - 6.2.2 The Influence of the Quantum Size Effect . . . 65
  - 6.2.3 Capture Efficiency . . . 83
- 6.3 Conclusion . . . 95

7 Electron Capture in Ultracold Atoms **97**
7.1 Computational Details 98
7.2 Results 102

IV Conclusion **111**

Part I

Motivation

This Inaugural Dissertation investigates whether the dynamics of electrons undergoing *interatomic coulombic electron capture* (ICEC) in real and in artificial atoms can be sufficiently numerically modelled by a two-electron description and whether these computations propose model-independent hypotheses for future investigations may they be of theoretical or experimental nature. Interatomic coulombic electron capture is a non-local process that has been theoretically proposed by various methods to be involved to some extent in the biologically relevant system of a magnesium (II) cation in water,[1] in the commercially important system of nanowire-embedded regions of quantum confinement,[2,3] and will be shown here to possibly play a role in the experimentally important system of trapped ions in ultracold atom clouds.[4,5] Therefore suggesting to be a universal process triggered by a free electron in a nearly arbitrary environment of atoms, this work reviews the established dynamical model for a nanowire-contained pair of quantum dots also known as artificial atoms,[6] and presents the first numerical model to investigate ICEC dynamics of a barium (II) cation in a surrounding cloud of ultracold rubidium atoms at typical experimental conditions.

Toward the central goal of deriving educated directives from numerical modelling of interatomic coulombic electron capture to guide future investigations and to strengthen the footing for a broader field of applications, this dissertation is composed in four parts: the motivation for this study arising from the fundamental nature of ICEC, the mathematical and physical background of the established model and suggestive concepts guiding the following numerical analysis and leading to the proposed generalised model for ultracold atoms, the numerical applications to artificial confinements in nanowires as well as to a barium (II) cation in a cloud of ultracold rubidium atoms at typical experimental conditions, and eventually the conclusion of the findings from the analysis of the conducted electron dynamics computations. In order to motivate the undertaking of further investigations employing interatomic coulombic electron capture, particularly in view that experimental confirmation is yet lacking, this part will focus on the variety of contexts in which the process is bound to occur and to affect the physics and chemistry therein. In chronological order of their predictions, the potential role of ICEC will briefly described for biologically relevant metal-water clusters as consequence of the initial prediction of the process, for current development of gradually smaller electronic devices of nanometre scale which is the field of the established dynamical model to be used and generalised thereafter, and for trapped ions in clouds of cold atoms which represent an active experimental research setup and provide an alternative field of applications beyond the solid-state systems currently considered by the available model for ICEC dynamics.

1 Relevance of the Interatomic Electron Capture

Free electrons can attach to atoms, ions and molecules if they achieve to transfer some of their energy to their surrounding. This usually happens by emission of light, instigation of vibration and rotation or by excitation of other electrons within the encountered systems. This energy transfer is usually expected to occur over a short range which made the prediction of long-ranged interatomic coulombic electron capture in 2009 particularly puzzling.[1] It proved under the perturbative assumptions of scattering theory that under certain conditions, the electrons bound to atoms in the environment can significantly assist electron attachment despite their relatively large separation on an atomic scale. So-called *non-local processes* have won considerable attention over the last decades,[7] and ICEC has been shown to be a fundamental energy transfer process also expected to affect systems from modern nano-electronic devices,[2,8,9] to biological systems.[10] Nevertheless, ICEC has mostly eluded investigations by experiment or time-resolved theory so far.

Processes allowing to capture electrons on molecules usually involve the breaking of chemical bonds known as dissociative electron attachment, and consequently destroy molecules and as a particular example even destroy DNA. Particularly slow electrons which are the result of propagating irradiation damage in biological organisms are harmful and genotoxic.[10–12] To prove that ICEC is competitive with respect to usual electron attachment mechanisms, the noble gas ions He^+ and Ne^+ were theoretically investigated in proximity of the relatively small organic molecule benzene in 2010.[13] By asymptotic approximations common within the perturbative treatment of scattering theory, it was then possible to show that especially in the case of reaction partners allowing an interatomic transfer of a small amount of energy, ICEC will be efficient.[13] It has been established since then that ICEC can also be prevalent in solid-state systems,[3,9] and has been recently discussed to become of concern for modern electronic applications in the constant race for more minute components in integrated circuits.[2] As electronic components gradually shrink smaller and smaller, few-electron processes become obstacle and potential solution operating at the smallest possible energies. At this stage, quantum mechanics dictate the operational rules of modern applications as we play with single photons and single electrons.[14,15]

We redefine our surroundings in terms of tiniest units and count time, length, mass, and energy in quanta.[16] Modern experiments allow time-resolved investigation of matter interacting with light or with matter at quanta of energies. One immerses atoms and molecules in droplets of superfluid helium,[17] creates droplets of liquids thousand times more dilute than common gases,[18,19] and suspends clouds of atoms at close to absolute zero temperature in the laboratory equivalent of free space.[4] Despite their sparsity, theoretical studies on interatomic coulombic electron capture have particularly targeted systems of relevance within already available experimental techniques: atom-atom collisions of noble gases[13,20], biologically relevant magnesium ions in water,[1] atoms immersed in helium clusters,[21] and local quantum-confinements embedded in nanowires.[3] With this dissertation, I intend to add ions in ultracold atom clouds to this collection which are typically prepared in modern hybrid traps to

investigate state-to-state chemistry.[22–24] Although each publication predicted ICEC at various degrees of theory for experimentally relevant systems, observations of ICEC have not yet been reported and experimental efforts are yet to come.

Compared to other non-local processes which have gained considerable attention experimentally and theoretically, ICEC remains a novelty.[7,20,25] Challenging available theoretical approaches, it was shown only last year, however, that it might even prove to be more efficient than originally estimated.[21] At the same time, reaction processes as interatomic coulombic decay (ICD) and electron-transfer mediated decay (ETMD) which belong to the same family as ICEC, embody blooming research fields in their own right involving many top-level theoretical and experimental groups worldwide. In conjunction with the potential importance of ICEC in consequence of radiation damage, in context of current electronic research & development, as well as in ultracold gas experiments, it is expected to gain attention in the coming years. In light of the recently found amplification of the reaction cross section for proximities below the original long-distance approximations,[21] on the one hand, and in light of the possible increased range within a macroscopic assisting environment as is shown in this dissertation, ICEC is going to become more significant. This project is therefore at the forefront of a significant field of research and represents an original and essential step to advance our understanding of this important process.

1.1 Dissociative Electron Attachment in Biological Systems

One of the major research fields of importance to society is the field of life science. While interatomic coulombic electron capture was initially considered for a magnesium (II) cation in a water cluster which is of essential role in the human body,[1] it gained more relevance in context with recent findings on radiation-induced free electrons in biological systems. This shall be briefly explained here. Radiation from the Sun, radioactive substances, or X-rays can cause damage in the body. While Solar irradiation is mostly superficial, ingested radioactive substances and penetrating X-rays can affect internal body cells and organs. It has been found recently that afflicted radiation damage can spread exponentially through the human body by a cascade of decay processes of chemical compounds which release numerous slow electrons. Decay processes related to radiation damage include Auger decay, interatomic coulombic decay (ICD), superexchange ICD, and electron-transfer mediated decay (ETMD), which have attracted considerable attention over the last decade.[7] Free electrons can break up other chemical bonds by attaching themselves to encountered atoms and have thus been found to be genotoxic. This is called *dissociative electron attachment*.[10,11,26] A strong enhancement of electron attachment was predicted in 2009 for several systems thanks to interatomic coulombic electron capture (ICEC) which is an environment-assisted process in which a free electron can efficiently attach to an ion, atom or molecule.[1,13] The excess energy of the electron attachment is transferred to an ion, atom or molecule in proximity which is thus ionised. This process has been proven to be efficient even over long distances between reaction partners. Moreover, the energy of the emitted electron changes if the two involved species have different ionisation potentials. This suggests therefore that ICEC might be a general process which controls damage of living cells under ionising irradiation

and has a central impact on radiation damage in biological systems.

Particularly metal cations are biologically abundant and expected to be strongly ICEC-active owing to their large electron affinity. Overall, up to 60% of the adult human body consists of water and even the bones contain 31% water.[27] About 2% in total are composed of metals.[28] Dissolved in water, an individual metal ion is surrounded by numerous water molecules which each provide a potential reaction partner for interatomic coulombic electron capture by the metal ion. As they are all subject to the same electromagnetic field which transfers the excess energy from the captured electron, one would expect coherence and correlation to arise and lead to superradiance[29–32] and superabsorption,[33–35] a pair of fundamental phenomena resulting in increased intensity and reaction rates depending on the number of reaction partners. Particularly alkali metals and alkaline earth metals regulate fluid flow into and out of body cells, blood pressure, muscle contractions, nerve signals and heart activity. More importantly, metals are the key ingredient to complex chemical structures called coordination compounds in which a central metal atom is surrounded by groups of non-metal atoms, the ligands. Coordination compounds are vital to living organisms as the central metallic atom enables and determines their functionality in regulating biological processes. An important example for such complexes is haemoglobin which contains a central iron atom, gives blood its red colour and carries the vital oxygen through our body to the organs.

1.2 Commercial Electronics on the Scale of Human DNA

In modern technology, a very different aspect of society, phenomena summoned by artificially modified materials and control on the scale of a few nanometres are the centre of attention for research & development and provide the central ingredient to more efficiency.[36,37] Integrated electronic circuits and their components shrink continuously whereas electronic displays and mobile phones expand with each consecutive generation. As electronic components reduce to smaller and smaller size in order to allow for ever-increasing performance, quantum-mechanical phenomena complicate traditional working principles but offer interesting novel opportunities.[38] Relying inherently on the manipulation and transport of electric charges, interatomic coulombic electron capture may pose a potential complication as well as a possible solution to quantum-controlled charge transfer in future generations of commercial electronic devices.

Even before the 1960s, electronic technology relied increasingly on semiconducting materials which allowed to annually double the number of hosted transistors per integrated circuit.[39] Toward the end of 1989, computer companies raced to be the first to release the then revolutionary *486* personal computer incorporating commercial transistors of 800 nm size.[40,41] Since then, the electronics industry has continued to strive for continuously refined manufacturing techniques to increase the performance by increasing the electronic component density. Three times the size of the human DNA, fin-shaped structures nearing 7 nm thickness are etched into semiconducting materials in mass production to form the transistors integrated in today's mobile-phone processors.[42–44] As hundred millions of capacitors, diodes, resistors and

transistors occupy less than a square centimetre,[45] quantum-mechanical phenomena become integral constituents in current electronic devices.[46]

When any bulk of material is reduced in size, its quasi-continuous band structure splits into discrete increasingly separated energy levels.[47,48] This phenomenon has been termed *quantum size effect*,[49–51] and also implies that within one material, any impurities, crystal defects or atoms contrasting with their environment can produce quantum-mechanical phenomena which modify electrical and optical properties. The development of electronic elements for data storage,[52] displays,[53] lasers,[54] sensors[55] and solar cells[56] thus incorporate this realisation and consequent quantum effects into innovative nanostructured technology.

Striving toward the next milestone of yet more compact electronic device components which is known as the 5-nm node, nanowire structures run among the prospective solutions.[57–59] Controlled manipulations can create local regions of quantum confinement within such a nanowire. These are known as quantum dots.[60–63] The established model to describe the electron dynamics induced by ICEC thus considers a nanowire holding two such regions, A and B, which are able to quantum-mechanically confine otherwise transmitted electrons.[2,8,9,64] An electron transported through the nanowire to enter the confinement region A can exert momentum pressure by Coulomb interaction on an initially bound electron within the nearby charged region B^-. The long-distanced energy transfer between both electrons captures the incident electron to form a charged region A^- while its neighbour is ionised according to

$$e^-_{in} + \ A{+}B^- \longrightarrow A^-{+}B \ + e^-_{out}. \tag{1}$$

On the one hand, the choice of ingredient materials determines the optical and electrical properties of device. On the other hand, current production techniques allow to control the material composition and carefully selected concentrations of foreign elements, known as doping, are essential techniques to improve the performance of electronic devices. In commercial electronics, this choice is weighed, however, against the availability or natural abundance of a candidate material and by its robustness in a large-scale production process which is why selected components demanding higher performance are made of rarer but better performing materials whereas other less deciding parts will readily be made of more available thus less expensive standard materials if overall performance remains comparable. In a component of nanometre scale like the considered pair of quantum confinements embedded in a nanowire, the quantum size effect offers a complementary cost-effective way to optimise key properties which is readily portable to industrial scale. It was thus proposed to investigate the change in efficiency and working of the interatomic coulombic electron capture induced by variation of size of the capturing confinement region.[2]

The electron dynamics of ICEC in quantum-dots indicated a reaction pathway that selectively worked at a particular energy determined by the decay of a collective resonance state $(A^-B^-)^*$.[2,8] Also carried by Coulomb interaction between electrons localised at different partner sites at long distances, this decay is known as

interatomic coulombic decay (ICD). Equally fundamental as ICEC, it was found to be active in any combination of two nearby electron-binding subsystems beyond being limited to individual atoms. It has thus been observed in atomic and molecular systems,[20,65,66] as well as more exotic hollow atoms,[67] within helium droplets,[68] biological systems,[69,70] as well as quantum confined solid-state systems like fullerenes[71], quantum-dots,[72–74] or quantum films.[75,76] Honouring the universal nature of ICEC and ICD which can present an inter-atomic, inter-molecular, inter-quantum-dot or otherwise interactive nature between two spatially separated units depending on the involved subsystems, it has therefore been suggested to speak of an *inter-coulombic electron capture* and *inter-coulombic decay* generally. Consequently, this reaction pathway within the considered nanowire would follow[2]

$$e^-_{in} + \ A{+}B^- \xrightarrow{\text{ICEC}} (A^-{+}B^-)^* \xrightarrow{\text{ICD}} A^-{+}B \ + e^-_{out}. \tag{2}$$

Within the established model for pairs of charged quantum dots, it had been known from previous studies that meeting the conditions for a resonant decay via ICD can improve the probability of a successful interatomic electron capture.[3,8,9] In addition, a recent investigation in relation to this dissertation was able to report distinct energy signatures identifying two reaction pathways.[2] These suggested that a portion of the electron capture occurred due to a direct coulombic transfer of energy which echoed the energetically broad distribution of the incoming electron but another portion presented the features of the energy-selecting resonance criteria characteristic for ICD. Previously shown for ICD,[77,78] ICEC was bound to be tied to the implications of the quantum size effect. In collocation with an empirical high-throughput study on the maximal ICEC probability in quantum dots which was able to suggest limiting energetic conditions for the successful capture,[64] the electron flux associated with ICEC has provided the main quantity to study the particular interplay with ICD.[2]

Representing the primary system of investigated electron dynamics in context of interatomic coulombic electron capture, this dissertation will revisit the preceding increasingly multivariate numerical studies to complement previous observations by additional considerations. Although it has not yet found a realisation by experiment, this covers the range of available control over the capturing confinement from adapting the confinement's size, via varying and manipulating the capturing material, to optimising the distance to the partner confinement. Thereby providing an extended set of numerical findings gathered in a consistent manner, this will point to probable more generally applicable relations beyond the restrictions of the particular model. This will provide the foundation to compare this model with other systems and potentially help guiding future investigations and alternative realisations. Alas, the methodological analysis will provide a starting point for the generalisation and first application to study the electron dynamics of ICEC in ultracold atoms.

1.3 Individual Ions in Clouds of Ultracold Atoms

Physical experiments with ultracold atoms and ions are currently most promising to investigate time-resolved state-to-state chemical processes and interactions.[79,80]

Experimentally, entrapment of cold atoms and ions has been undertaken for some time. On the one hand, ions as well as individual charged particles can be contained and their properties as well as natural constants be measured to the highest precision by Paul traps and by Penning traps which merited the Nobel prize in 1989.[5] On the other hand, entire clouds of neutral atoms can be cooled down collectively to accumulate and then be held in their energetically lowest atomic state which is known as a Bose-Einstein condensate awarded for its scientific importance by the Nobel prize in 2001.[4] Building on these working principles, hybrid traps employ two different traps simultaneously. They represent the current state of the art and allow to investigate interactions of captured ions within ultracold atom clouds at real-time.[22–24]

Working at low temperatures, such experiments admit to study numerous phenomena and fundamental interactions with minimal thermal intervention. Concepts and questions of astrophysics, astrochemistry and selective state-to-state chemistry come into reach at laboratory conditions with time resolution. The need for dynamical descriptions and models of phenomena thus rises as time-resolved investigations are becoming the experimental standard where estimates of asymptotic quantities and behaviour do not suffice any longer. With respect to interatomic coulombic electron capture, the essential ingredient necessary missing from current ultracold atom-ion experiments is a source of electron. Although a directed electron source is in fact the oldest of the three components necessary for such a proposed ICEC experiment, it has so far been omitted from the experiments because hybrid-trap vacuum chambers are sensitive to disturbances. Assembling all experimental components to achieve a stable ultra-high vacuum ($< 10^{-6}$ Pa)[1] at low temperatures is a challenge in itself. It requires multi-stage pumping, ion gauge measurement, and particular procedures like the baking of the vacuum chamber to remove remaining traces of gases. Nevertheless, electron sources in the form of cathode rays have been known for nearly two centuries since Michael Faraday.[81] These streams of electrons within vacuum tubes have even been the central component in commercial screens for oscilloscopes and televisions. They are therefore conceptually simple enough to add onto modern experiments which follow a modular design.[22] As such, it can be considered a mere matter of time until the first realisation of such an ICEC experiment is being reported and a suitable dynamical model is inevitably being required.

Within the context of atomic systems, interatomic coulombic electron capture can bind a free electron spontaneously to an atom if an atom is present in its environment whose electrons can consume part of the free electron's energy. For this dissertation, ICEC shall be considered in the prototypical system of a barium (II) cation suspended in a cloud of ultracold neutral rubidium atoms at typical experimental hybrid-trap conditions. When a barium (II) cation Ba^{2+} is capturing an electron e^- with assistance from a nearby rubidium atom Rb, the atom can either be excited to Rb^* as

$$e^-_{in} + Ba^{2+} + Rb \longrightarrow \left(Ba^{1+}\right)^* + Rb^* \,, \tag{3}$$

[1] DIN 28400: Vakuumtechnik Bennenungen und Definitionen, 1972.

or can be ionised directly

$$e^-_{in} + Ba^{2+} + Rb \longrightarrow \left(Ba^{1+}\right)^* + Rb^{1+} + e^-_{out} \ , \tag{4}$$

depending on the amount of energy transferred to rubidium's electrons.

According to the experimentally known spectral lines of both reaction partners,[82–84] the incident electron can attach to an excited energy level in either case or can attach directly to the barium ground state which ionises rubidium as

$$e^-_{in} + Ba^{2+} + Rb \longrightarrow Ba^{1+} + Rb^{1+} + e^-_{out} \ . \tag{5}$$

Moreover, the interatomic coulombic electron capture into an excited state of the barium (II) offers the possibility of consecutive decay reactions towards the ground state. Denoting this Coulomb-coupled intermediate resonance state by $(Ba^{+}{+}Rb)^*$ in analogy to the previously described decaying macroscopic two-electron resonance state $(A^-B^-)^*$ in a pair of interacting charged quantum confinements, this reaction can then follow the path

$$e^-_{in} + Ba^{2+} + Rb \xrightarrow{\text{ICEC}} \left(Ba^{1+}{+}Rb\right)^* \xrightarrow{\text{ICD}} Ba^{1+} + Rb^{1+} + e^-_{out} \ . \tag{6}$$

Although to some extent analogous to the established model system of quantum-dot pairs in nanowires, the numerous electronic energy levels available within the involved atoms open up a myriad of possible reaction pathways but lack a control parameter equivalent to the variation of the confinement size. In addition with the multiplication in degrees of freedom, the electron dynamics are expected to become more nuanced, and an appropriate model to become more complicated and demanding.

2 Available Investigative Methods

Treating interatomic coulombic electron capture is methodologically difficult. First predictions have been made under strong perturbative assumptions within the approximative framework of scattering theory.[1] While sufficient to prove ICEC to be competitive, it provided a lower limit estimate and fails to evaluate the process accurately for reaction partners in closer proximity. After the original asymptotic predictions of ICEC, its electron dynamics were investigated successfully using *multi-configurational time-dependent Hartree(-Fock)* (MCTDH) computations for quantum-dots in nanowires.[3] The approach proved to be successful to establish ICEC as fundamental process beyond atomic or molecular systems and argued that it will play a role in modern nano-electronic applications.[2] Within atomic contexts, the MCTDH approach was also able to investigate the dependence on cluster size for its sister process ICD.[85] However, an atomistic description if ICEC with MCTDH remains challenging and numerically demanding. The modelling of a free electron asks simultaneously for an extended real-space in order to contain a region of decidedly low binding potential, and for a high number of basis-functions to simulate free states by a satisfyingly well resolved quasi-continuum. Attempts to increase the degrees of freedom by explicit treatment of further electrons are consecutively hindered by the requirements of satisfactory spatial and energetic resolution.

Prominent alternative approaches to many physical and chemical problems like Density Functional Theory which are able to deal with large numbers of electrons,[86] struggle however with the concept of particles entering and leaving the system and can fail in systems of strong correlation.[87,88] Eventually, the method of R-matrix theory generally divides a physical problem into two regions: an outer one where only the scattered particle – here the ICEC electron – is explicitly considered and an inner region of close distances where all particles are described with their more complex interactions and reactions.[89] The R-matrix approach, however, also struggles with systems of very large extension, particularly Rydberg states, and assumes a restricted interaction region.[89] Nevertheless, it was recently shown to allow some insight into ICEC for atoms at close distance.[21]

Calculating the full electron dynamics of the ICEC process in a charged quantum-dot-pair model of two Gaussian binding potentials is thus best established.[2,3,8,9,64] At a high level of numerical accuracy in electron-electron correlation, the multi-configurational time-dependent Hartree (MCTDH) approach[90,91] has been applied to this comparably small system with fermionic antisymmetrisation of a discrete-variable-represented (DVR) wavefunction as implemented in the Heidelberg software suite.[92,93] Offering access to the full electron dynamics by solving the time-dependent Schrödinger equation, this grid-like approach addresses bound and continuum states on the same footing. Since this is not usually accomplished with many other theoretical methods and interatomic coulombic electron capture has been considered for atomic and molecular systems only in the original two articles by Gokhberg and Cederbaum,[1,13] and the recent study by Sisourat et al.,[21] an adaptation of the affirmed approach for quantum dots to venture into electron dynamics of ICEC in atomic systems appears intriguing. It will thus be tested in this dissertation not least for its methodological consistence with the preceding investigations of ICEC dynamics, whether the quantum-dot-pair model may be expanded to an atomistic model of frozen-core pseudopotentials with effectively two electrons which will allow to retain the MCTDH approach to solve the time-dependent Schrödinger equation.

Part II
Theory

3 Theoretical Background

3.1 General Concepts and Notation

Throughout this work, the Dirac bra-ket notation shall be used. Considerations shall be limited to dynamics of few electrons. Such an electron can be found in an arbitrary quantum state $\big|\alpha\big\rangle$ while another occupies arbitrary quantum state $\big|\beta\big\rangle$. In contrast to some contexts, they shall not denote particular spin states here. An individual electron will be acted upon by a Hamiltonian operator $\hat{h}$ which governs its kinetic energy T and an external binding potential V induced by atoms or a collective cluster of atoms in the form of an effective binding potential. This (effective) single-electron Hamiltonian gives rise to a sequence of eigenstates which shall be labelled by a quantum number n and have an associated eigenenergy E_n according to the stationary Schrödinger equation

$$\hat{h}\big|n\big\rangle = E_n\big|n\big\rangle \ . \tag{7}$$

If the electron is not bound and localised within the potential such that the eigenenergies become a continuous band rather than discrete values then counting the eigenstates by the quantum number n becomes a poor description. This is thus called a continuum state where ε shall denote its energy and shall serve as substitute quantum label in the stationary Schrödinger equation

$$\hat{h}\big|\varepsilon\big\rangle = \varepsilon\big|\varepsilon\big\rangle \ . \tag{8}$$

Furthermore, a wavepacket of a free electron with spatial uncertainty Δ and group momentum p_0 shall be denoted by $\big|\phi\big\rangle$ such that unbound states are generally referred to by Greek and bound states by Roman labels. Considering two electrons in the same system, they will each be acted upon by a respective Hamiltonian $\hat{h}_k$ and feel an additional interaction V_{12} between each other such that the overall Hamiltonian of the system is

$$\hat{H} = \hat{h}_1 + \hat{h}_2 + V_{12} \ . \tag{9}$$

The overall quantum state of the system $\big|\Psi\big\rangle$ is governed by the equation of motion known as the time-dependent Schrödinger equation

$$i\hbar\big|\dot{\Psi}\big\rangle = \hat{H}\big|\Psi\big\rangle \tag{10}$$

where i denotes the imaginary unit, $\hbar$ is the reduced Planck constant and $\big|\dot{\Psi}\big\rangle$ denotes the partial derivative with respect to time of state $\big|\Psi\big\rangle$. Defining the exponential operator acting on an arbitrary operator $\hat{O}$ as

$$\exp(\hat{O}) := \sum_{k=0}^{\infty} (k!)^{-1} \hat{O}^k \tag{11}$$

where $k!$ denotes the factorial $1 \cdot 2 \cdot 3 \cdot \ldots \cdot k$, the formal solution to the time-dependent Schrödinger equation for a time-independent Hamiltonian is a state vector

$$\Big|\Psi\Big\rangle = \exp(-\tfrac{i}{\hbar}\hat{H}t)\Big|\Psi_0\Big\rangle =: \hat{U}_t\Big|\Psi_0\Big\rangle \tag{12}$$

at time t which is produced by action of the time-evolution operator $\hat{U}_t$ on an initial state vector $\Big|\Psi_0\Big\rangle$.

The bra-ket notation is independent of a particular representation of the state vector. However, the choice of a basis is usually necessary to analytically and numerically evaluate quantum operators and quantum states. One can for instance choose the continuous position basis $\big\{\Big|\vec{r}_1, \vec{r}_2\Big\rangle\big\}_{(\vec{r}_1,\vec{r}_1)\in\mathbb{R}^6}$ which is in this example generally consisting of three degrees of freedom per electron such that one arrives at a wavefunction

$$\Psi(\vec{r}_1, \vec{r}_2) = \Big\langle \vec{r}_1, \vec{r}_2 \;\Big|\; \Psi \Big\rangle \tag{13}$$

which is called a *probability amplitude* of the position.[94] It is generally a complex number and its absolute value is related to the *probability density*

$$P(\vec{r}_1, \vec{r}_2) := |\Psi(\vec{r}_1, \vec{r}_2)|^2 \; d^3\vec{r}_1 \; d^3\vec{r}_2 \tag{14}$$

of simultaneously finding one electron in the infinitesimal volume $d^3\vec{r}_1$ at position $\vec{r}_1$ while also finding the other electron in the infinitesimal volume $d^3\vec{r}_1$ at position $\vec{r}_1$.[94]

The action of an operator on the quantum state is interpreted as measurement of a physically observable quantity represented by the operator. The physics are thus given by the expectation value

$$\langle O \rangle := \Big\langle \Psi \;\Big|\; \hat{O} \;\Big|\; \Psi \Big\rangle \tag{15}$$

of observable $\hat{O}$ and the time-dependent Schrödinger equation is thus equivalent to operator equation

$$i\hbar \, \frac{d}{dt}\hat{O}(t) = \Big[\hat{O}(t), \hat{H}\Big] + i\hbar \left(\frac{\partial \hat{O}}{\partial t}\right)(t) \tag{16}$$

known as the Heisenberg equation of motion where the time-dependent interpretation of the operator is given by

$$\hat{O}(t) := \hat{U}_t^\dagger \hat{O} \hat{U}_t \text{ , where further} \tag{17}$$

$$\Big[\hat{A}, \hat{B}\Big] := \hat{A}\hat{B} - \hat{B}\hat{A} \tag{18}$$

is the commutator of two operators and $U_t^\dagger$ is the adjoint of the time-evolution operator such that

$$\Big\langle \hat{U}_t \Psi_0 \;\Big|\; \Psi_0 \Big\rangle =: \Big\langle \Psi_0 \;\Big|\; \hat{U}_t^\dagger \Psi_0 \Big\rangle \, . \tag{19}$$

The operator $\hat{U}_t^\dagger$ is also called the *Hermitian adjoint* operator of $\hat{U}_t$.[94] Moreover, if an operator and its adjoint are equal

$$\hat{A}^\dagger = \hat{A} \, , \tag{20}$$

it is called *self-adjoint* or *Hermitian*. This property is consequently the *Hermiticity*.

Under closer inspection of the Hamiltonian for two electrons in Eq. (9), one notices the first two terms $\hat{h}_1+\hat{h}_2$ together are describing the electrons in their respective environment as if they were independent whereas the last term represents the changing conditions as they interact with each other. Assuming they would not be interacting at all, the time evolution of observables would be entirely governed by[95]

$$\hat{O}_I(t) := \hat{U}_{0t}^{\dagger}\ \hat{O}\ \hat{U}_{0t} \tag{21}$$

where $\hat{U}_{0t}$ is the time-evolution operator related by Eq. (12) to the non-interactive Hamiltonian

$$\hat{H}_0 := \hat{h}_1 + \hat{h}_2 \tag{22}$$

which also implies an evolution of the electron interaction itself as

$$\hat{H}_I(t) := \hat{U}_{0t}^{\dagger}\ V_{12}\ \hat{U}_{0t}\,. \tag{23}$$

Further, let the adjoint time evolution operator of the non-interactive Hamiltonian act on the overall wavefunction be designated by[95]

$$\Big|\Psi_I\Big\rangle := \hat{U}_{0t}^{\dagger}\Big|\Psi\Big\rangle\,, \tag{24}$$

then the time evolution of the quantum system including the interaction can be expressed by the set of equations of motion

$$i\hbar\,\Big|\dot{\Psi}_I\Big\rangle = \hat{H}_I(t)\Big|\Psi_I\Big\rangle \ \text{ and} \tag{25}$$

$$i\hbar\,\frac{d}{dt}\hat{O}_I = \Big[\hat{O}_I(t), \hat{H}_0\Big] + i\hbar\left(\frac{\partial\hat{O}}{\partial t}\right)_I\!(t) \tag{26}$$

proposed by Dirac. It appears in the form of the Schrödinger equation of motion from Eq. (10) for an evolution of the quantum state induced by the interaction part of the Hamiltonian and in the form of its Heisenberg equivalent of Eq. (16) for an evolution of the operators by the interaction-free part of the Hamiltonian.[95]

3.1.1 Scattering Quantum States

Let $\Big|\mathtt{i}\Big\rangle$ represent a quantum state of interest to an investigation of a particular process involving two electrons, let it be characterised by a set of criteria on the initial conditions of the individual electrons and let $\Big|\mathtt{f}\Big\rangle$ represent a quantum state characterised by a set of criteria on the final conditions of the individual electrons after they successfully underwent the investigated process. This process is called a *scattering process* if the full description of the initial state reduces to a simpler non-interactive time-evolution in the past

$$\lim_{t\to-\infty}\hat{U}\Big|\mathtt{i}\Big\rangle = \lim_{t\to-\infty}\hat{U}_0\Big|\mathtt{i}\Big\rangle \tag{27}$$

and if this holds analogously for the final state at a time in the future

$$\lim_{t\to+\infty}\hat{U}\Big|\mathtt{f}\Big\rangle = \lim_{t\to+\infty}\hat{U}_0\Big|\mathtt{f}\Big\rangle\,. \tag{28}$$

In the case of a two-electron scattering, this means that the two electrons were separated over a very large distance at some point in the past where the electron-electron interaction was negligible such that they were initially acting as independent particles in state $\left|\mathtt{i}\right\rangle$. As they approach each other, the interaction potential increases, they interact in some way, and they separate again with increasing time. As they grow gradually further apart, the interaction strength diminishes until they appear as independent particles in the final state $\left|\mathtt{f}\right\rangle$.[96] Because the time evolution operator is unitary which means that the product with its adjoint $\hat{U}^\dagger\hat{U} = \mathbb{1} = \hat{U}\hat{U}^\dagger$ commutes and provides the identity operator, the above equations are equivalent to

$$\left|\mathtt{i}\right\rangle = \lim_{t\to-\infty} \hat{U}^\dagger\hat{U}_0\left|\mathtt{i}\right\rangle =: \hat{\Omega}_+\left|\mathtt{i}\right\rangle, \text{ and} \tag{29}$$

$$\left|\mathtt{f}\right\rangle = \lim_{t\to+\infty} \hat{U}^\dagger\hat{U}_0\left|\mathtt{f}\right\rangle =: \hat{\Omega}_-\left|\mathtt{f}\right\rangle \tag{30}$$

which introduces the so-called Møller operators $\Omega_\pm$.[95–97] The quantity of interest in such a scattering is the probability amplitude of a transition from the initial quantum state $\left|\mathtt{i}\right\rangle$ to the final quantum $\left|\mathtt{f}\right\rangle$ which are equivalent to the unpropagated interaction states $\left|\mathtt{i}_I(0)\right\rangle$ and $\left|\mathtt{f}_I(0)\right\rangle$ and relates similarly to the defining equations of the Møller operators as

$$\left\langle \mathtt{f}_I(0) \,\middle|\, \mathtt{i}_I(0)\right\rangle = \left\langle \mathtt{f} \,\middle|\, \mathtt{i}\right\rangle = \left\langle \mathtt{f} \,\middle|\, \lim_{t\to+\infty} \hat{U}_0{}^\dagger\hat{U} \;\lim_{t\to-\infty} \hat{U}^\dagger\hat{U}_0 \,\middle|\, \mathtt{i}\right\rangle. \tag{31}$$

Here, the right hand side can be attributed to the interaction time evolution propagator $\hat{U_I}_t$ employing the unitarity of $\hat{U}_t$ such that one arrives at

$$\left\langle \mathtt{f} \,\middle|\, \mathtt{i}\right\rangle = \lim_{t\to+\infty}\left\langle \mathtt{f}_I(+t) \,\middle|\, \hat{U}_{I+t}\;\hat{U}_{I\text{-}t} \,\middle|\, \mathtt{i}_I(-t)\right\rangle = \left\langle \mathtt{f}_I(\infty) \,\middle|\, \hat{S} \,\middle|\, \mathtt{i}_I(-\infty)\right\rangle \tag{32}$$

which relates the transition probability amplitude between the two states to the asymptotic large time limit of the interaction propagated states. At this limit, the two representations $\left|\mathtt{i}_I(-\infty)\right\rangle$ and $\left|\mathtt{f}_I(+\infty)\right\rangle$ are simplest and for the example of the two-electron scattering, they represent independent electrons long before, respectively long after a collision. It therefore suffices to work with these simpler descriptions at the respective limit if an operator $\hat{S}$ can be found which transports the aspects of the multi-faceted real-world scattering to this simple-world asymptotic picture which is why the operator is called the *scattering operator*.[95,96]

Since the system Hamiltonian is a superposition of operator V_{12} describing the interaction between the electrons of interest and operators $\hat{h}_{1/2}$ describing the simpler aspects of the system acting only on each electron individually, the latter is often denoted as the free part $\hat{H}_0$ in literature while the additional interaction between the described particles is considered an interaction Hamiltonian $\hat{H}'$.[95]

When evaluating energy exchange processes like the interatomic coulombic electron capture, it is thus of interest to study the interaction-free Hamiltonians, their eigenstates and the evolution of initial quantum states in order to evaluate the contributions arisen from the specific interaction under investigation. Of particular value are the well-known solutions of the quantum harmonic oscillator and the hydrogen problem which shall be summarised for completeness.

3.2 The Quantum Harmonic Oscillator

The quantum harmonic oscillator is a central concept of quantum mechanics thanks to its numerous applications. A potential of the form

$$V_{HO} = \tfrac{1}{2} m\omega^2 x^2 \tag{33}$$

shall be given where ω denotes the system parameter of angular frequency related to the oscillator strength, m denotes the oscillator mass and x denotes an independent variable of position. The harmonic oscillator Hamiltonian in position basis representation in one dimension then reads

$$\hat{H}_{HO} = \frac{\hat{p}^2}{2m} + \frac{m\omega^2 \hat{x}^2}{2} \tag{34}$$

where $\hat{p}$ is the momentum operator and $\hat{x}$ is the position operator. The canonical momentum operator in position basis representation is given by $\hat{p} = -i\hbar\partial_x$ where ∂_x is abbreviating $\partial/(\partial x)$ denoting the partial derivative with respect to x.

Introducing the so-called annihilation operator

$$\hat{a}_{HO} := \sqrt{\frac{m\omega}{2\hbar}}\hat{x} + \frac{i\hat{p}}{\sqrt{2m\hbar\omega}} \tag{35}$$

and its adjoint the creation operator

$$\hat{a}^\dagger_{HO} := \sqrt{\frac{m\omega}{2\hbar}}\hat{x} - \frac{i\hat{p}}{\sqrt{2m\hbar\omega}} \,, \tag{36}$$

the Hamiltonian can be expressed as[98]

$$\hat{H} = \hbar\omega(\hat{a}^\dagger\hat{a} + \tfrac{1}{2}) \,. \tag{37}$$

Known as the *number operator*, $\hat{a}^\dagger\hat{a}$ produces dimensionless integer number eigenvalues

$$\hat{N}_{HO}\psi^{HO}_n := \hat{a}^\dagger_{HO}\hat{a}_{HO}\ \psi^{HO}_n = n\ \psi^{HO}_n \tag{38}$$

for an eigenfunction ψ^{HO}_n and is interpreted as the amount of stored quanta of $\hbar\omega$ in the oscillator system. While the amount of stored quanta can be zero, the energy eigenvalue remains a finite value which is thus called the zero-point energy as

$$\hat{H}_{HO}\ \psi^{HO}_0 = \tfrac{\hbar\omega}{2}\ \psi^{HO}_0 \,. \tag{39}$$

The eigenfunction ψ^{HO}_0 corresponding to the zero-point energy is called the ground state function, the lowest energy state. Furthermore the creation operator raises the eigenfunction to the next higher one such that any nth eigenfunction can be created from the ground state by n consecutive operations of the creation operator

$$\sqrt{n!}\ \psi^{HO}_n = (\hat{a}^\dagger_{HO})^n\ \psi^{HO}_0 \tag{40}$$

which is the reason why the creation and annihilation operator are also called raising and lowering operator or ladder operators. The ground state function is given by[98]

$$\psi^{HO}_0 = \left(\tfrac{m\omega}{\pi\hbar}\right)^{\frac{1}{4}} \exp\left[-\tfrac{m\omega}{2\hbar}\ x^2\right] \tag{41}$$

which is a Gaussian function.

3.2.1 Gaussian Functions

Known as *normal distribution*, Gaussian functions of the form

$$G(x) = (2\pi\Delta^2)^{-\frac{1}{2}} \exp\Big[-\tfrac{1}{2}(\tfrac{x-x_m}{\Delta})^2\Big] \tag{42}$$

with mean position x_m and standard deviation Δ are important classical probability distributions.[99,100] They are also of central value for numerous numerical applications because they offer a well-defined integral

$$\int_{-\infty}^{\infty} dx \ \exp\Big[-(x/\Delta)^2\Big] = \sqrt{\pi\Delta^2} \ . \tag{43}$$

Moreover, its cumulative distribution function is given by the error function[100]

$$\operatorname{erf} z := \tfrac{2}{\sqrt{\pi}} \int_0^z dx \ \exp\Big[-x^2\Big] \tag{44}$$

and the complementary error function

$$\operatorname{erfc} z = \tfrac{2}{\sqrt{\pi}} \int_z^{\infty} \exp\Big[-x^2\Big]\, dx = 1 - \operatorname{erf} z \tag{45}$$

which has no analytical representation itself but in turn gives rise to the Hermite polynomials H_n as[100]

$$H_n(z) := \tfrac{\sqrt{\pi}}{2}(-1)^n \exp[z^2] \ \frac{d^{n+1}}{dz^{n+1}} \operatorname{erf} z = \tfrac{\sqrt{\pi}}{2}(-1)^{n+1} \exp[z^2] \ \frac{d^{n+1}}{dz^{n+1}} \operatorname{erfc} z \ . \tag{46}$$

Eventually, these polynomials form an orthogonal set of functions with respect to the Gaussian function as weight

$$\int_{-\infty}^{\infty} dx \ \exp[-x^2] \ H_m(x)\, H_n(x) = \sqrt{\pi} \ 2^n n! \ \delta_{nm} \tag{47}$$

which makes the eigenfunctions of the quantum harmonic oscillator an orthonormal basis with elements of the form[98]

$$\psi_n^{HO} = \left(\frac{m\omega}{\pi\hbar}\right)^{\frac{1}{4}} \frac{H_n\Big(\sqrt{\frac{m\omega}{\hbar}}x\Big)}{\sqrt{2^n n!}} \ \exp\Big[-\tfrac{m\omega}{2\hbar}x^2\Big] \ . \tag{48}$$

Gaussian functions as well as the error functions and Hermite polynomials play an important role in numerous problems in probability theory, statistics, combinatorics, economics, physics, numerical modelling and analysis in form of Gaussian quadrature and electrical engineering as Gaussian noise and random matrix theory. Eventually, the complex version of the -1st Hermite polynomial is nowadays known as Faddeeva function[100]

$$w(z) := \exp((iz)^2)) \operatorname{erfc}(-iz) = H_{-1}(-iz) \tag{49}$$

and has the important integral relation[100]

$$w(z) = -\frac{i}{\pi} \int_{-\infty}^{\infty} dt \ \frac{\exp[-t^2]}{t-z} = -\frac{2iz}{\pi} \int_{-\infty}^{\infty} dt \ \frac{\exp[-t^2]}{t^2-z^2} \tag{50}$$

and is also related to Voigt functions which play an important role in spectral analysis and spectral line broadening.

3.2.2 Characteristic Scales of Length, Momentum and Energy

In each quantum-mechanical problem, operators represent measurements of observable quantities through their expectation value although the solution of the Schrödinger equation itself usually depends on dimensionless quantities. Owing to this aspect, characteristic scales arise from fundamental constants and system parameters for each observable and form a characteristic set of units. As the system energy of stationary states of the harmonic oscillator is given in half-integer values of $\hbar\omega$ and represented by the Hamiltonian operator, its energetic contributions from kinetic and potential energy operator must also each be scaling with this characteristic energy. Identifying $\frac{\hbar\omega}{2}$ as factor in the potential energy operator thus implies the remaining factors to form a dimensionless factor

$$V_{HO} = \frac{\hbar\omega}{2}\left(\sqrt{\frac{m\omega}{\hbar}}\hat{x}\right)^2 \tag{51}$$

which sets the characteristic length

$$d = \sqrt{\frac{\hbar}{m\omega}} \tag{52}$$

Factorising the kinetic energy operator equally

$$\hat{T}_{HO} = \frac{\hbar\omega}{2}\left(\frac{\hat{p}}{\sqrt{m\hbar\omega}}\right)^2 , \tag{53}$$

suggests the characteristic momentum

$$\check{p} = \sqrt{m\hbar\omega} . \tag{54}$$

The wavefunction in position basis representation is thereby only a function of the ratio x/d, not the position itself while annihilation, creation and number operator consistently prove to be dimensionless.

3.3 The Gaussian Potential Well

Gaussian potential wells and potential barriers are commonly used to model smooth local changes in a potential usually due to some average cumulative many-body interaction. While step functions tend to be more appealing from a qualitative perspective describing an encountered surface of some kind, they fail to account for the fact that surfaces affect close-by regions on either side of the surface thus leading to a smoothing out of the effective potential over space. Gaussian potentials on the other hand are analytically challenging but numerically fast. They are thus more common in numerical investigations and modelling than in analytical ones. As such, they are commonly used to model atomic wavefunctions and effective atomistic binding potentials on valence electrons, assuming that the core electrons tend to stay in the ground state while the valence electrons are actively participating in physical and chemical processes.

While there are a few numerical investigations of the eigenvalues and eigenfunctions of the Schrödinger equation for a Gaussian potential well on the one hand and entire fields of Gaussian variate dynamics including an expansion mechanism of a multivariate Gaussian function into sums of products of single-variate Gaussians on the other hand, a simple and clear expression of the stationary Schrödinger problem appears to be missing so far. This section shall therefore outline concepts and stationary solution of the Gaussian well which will be shown to have the Quantum Harmonic Oscillator solution as limit on the one side and the free particle solution as limit on the other side.

Generally speaking, a Gaussian potential has a pair of parameters defining it's potential strength and it's spatial extent. Commonly numerically given as a pair (D, b) in units of energy and reciprocal area. In analogy with the probability function also sometimes given as an equivalent pair (D, Δ) in units of energy and length directly, referring to the maximal potential depth and spatial standard deviation of the potential. It can further be shifted on the energy axis by a constant value to either define the continuum threshold as $E = 0$ or the potential's extremal point. These definitions are equivalent, as is the following definition seeking maximal analogy with the quantum harmonic oscillator description.

Let κ be a positive real number here to be called *harmonic parameter* and let the one-dimensional Gaussian potential in position basis representation be given by

$$V_G(x) := \frac{\hbar\omega}{2}\kappa\left(1 - \exp\left[-\tfrac{m\omega}{\kappa\hbar}\ x^2\right]\right)\ , \tag{55}$$

where m is a mass and ω is an angular frequency, both system parameter known from the harmonic oscillator.

This definition can also be expressed in the infinite polynomial series of the exponential function as

$$V_G(x) = \frac{m\omega^2}{2}\hat{x}^2 - \frac{m^2\omega^3}{2\kappa\hbar}\frac{\hat{x}^4}{2!} + \frac{m^3\omega^4}{2\kappa^2\hbar^2}\frac{\hat{x}^6}{3!} - \ldots + \ldots\ . \tag{56}$$

The first summand is independent of the harmonic parameter κ such that the Gaussian potential tends to the harmonic oscillator potential if κ becomes very large

$$\lim_{\kappa\to\infty} V_G(x) = V_{HO}(x)\ . \tag{57}$$

At the same time, the characteristic length scale is given by the standard deviation of the potential

$$\Delta_G = \sqrt{\frac{\kappa\hbar}{2m\omega}} \tag{58}$$

which is proportional to the square root of the harmonic parameter and implies that it becomes narrower and simultaneously loses potential strength as κ tends to vanish

$$\lim_{\kappa\to 0} V_G(x) = 0\ . \tag{59}$$

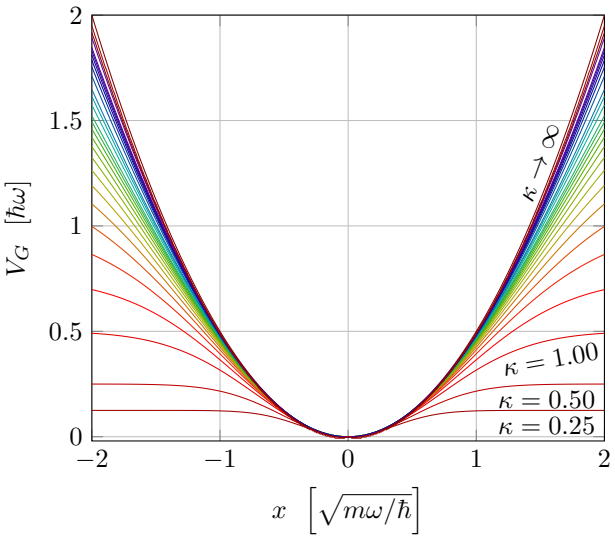

Figure 1: The Gaussian potential well for varying harmonic parameters κ. For $\kappa \to \infty$, the harmonic potential is recovered, whereas for $\kappa = 1$ the potential is limited by $(\hbar\omega)/2$. For decreasing κ, the potential shrinks and flattens to zero, while retaining the harmonic behaviour around zero.

The Gaussian potential well thus vanishes with the harmonic parameter κ where bound states must reduce in number and eventually disappear such that the eigenvalue problem goes over to that of a free-particle. It is thus essential that a solution to the stationary Schrödinger equation tends to the discrete harmonic oscillator solution for large κ and to the continuous spectrum of free-particle eigenfunctions if κ vanishes. At a finite non-vanishing harmonic parameters κ, however, bound solutions of discrete eigenenergies E_n^G can only occur in the energy interval

$$0 < E_n^G < \frac{\hbar\omega}{2}\kappa \tag{60}$$

between the potential minimum at zero and the continuum threshold which is thereby proportional to κ.

Let $A((m\omega/\hbar)^{\frac{1}{2}}\ x)$ be a polynomial in the dimensionless equivalent of x known from the harmonic oscillator,

$$A((m\omega/\hbar)^{\frac{1}{2}}\ x) := \sum_{k=0}^{\infty} a_k \left(\sqrt{\tfrac{m\omega}{\hbar}}x\right)^k \ . \tag{61}$$

The Hamiltonian operator is of units $(\hbar\omega)/2$ which can thus be factored out to arrive at the following expression in position basis representation

$$\hat{H}_G := \frac{\hbar\omega}{2}\left(\frac{\hat{p}^2}{m\hbar\omega} + \frac{m\omega}{\hbar}\hat{x}^2 + \sum_{k=2}^{\infty}\frac{(-\kappa)^{1-k}}{k!}\left(\tfrac{m\omega}{\hbar}\hat{x}^2\right)^k\right) \ . \tag{62}$$

Assuming a function of the form equivalent to the harmonic oscillator ground state

$$\psi := \left(\frac{m\omega}{\pi\hbar}\right)^{\frac{1}{4}} \exp\Big[A((m\omega/\hbar)^{\frac{1}{2}}x)\Big] \ , \tag{63}$$

is a solution to the stationary Schrödinger equation with canonical momentum $\hat{p} = -i\hbar\partial_x$ and eigenvalue $\hbar\omega\lambda/2$, the eigenvalue problem is given by

$$\frac{\hbar\omega}{2}\left(-A'' - A'^2 + \tfrac{m\omega}{\hbar}\hat{x}^2 + \sum_{k=2}^{\infty}\frac{(-\kappa)^{1-k}}{k!}\left(\tfrac{m\omega}{\hbar}\hat{x}^2\right)^k\right)\psi = \frac{\hbar\omega}{2}\,\lambda\psi \tag{64}$$

where A' and A'' denote the first and second derivative of the polynomial $A(x/d)$. Since a non-trivial solution is not vanishing for all x values, the polynomial A has to fulfil

$$A'' + A'^2 + \lambda\delta_{0,k} - \tfrac{m\omega}{\hbar}\hat{x}^2 - \sum_{k=2}^{\infty}\frac{(-\kappa)^{1-k}}{k!}\left(\tfrac{m\omega}{\hbar}\hat{x}^2\right)^k = 0 \tag{65}$$

where $\delta_{0,k}$ shall be the Kronecker delta. As the powers of x are linearly independent, this becomes a system of quadratic equations in a_k

$$\left((2k{+}2)(2k{+}1)a_{(2k+2)} + \sum_{j=0}^{2k+1} j(2k{+}2{-}j)a_j a_{(2k+2-j)} + \right. \\ \left. + (\lambda-\kappa)\,\delta_{0,k} - \frac{(-\kappa)^{1-k}}{k!}\right)\left(\tfrac{m\omega}{\hbar}\hat{x}^2\right)^k = 0 \tag{66}$$

$$\left((2k{+}3)(2k{+}2)a_{(2k+3)} + \sum_{j=0}^{2k+2} j(2k{+}3{-}j)a_j a_{(2k+3-j)}\right)\left(\tfrac{m\omega}{\hbar}\hat{x}^{2k}\right)^{k+\frac{1}{2}} = 0 \tag{67}$$

for each power where the potential itself only contributes to the even powers and one arrives at a recursive definition for even and another for odd powers. Explicitly, these are

$$(2k{+}2)(2k{+}1)a_{(2k+2)} := -\sum_{j=0}^{2k+1} j(2k{+}2{-}j)a_j a_{(2k+2-j)} + (\kappa-\lambda)\delta_{0,k} + \frac{(-\kappa)^{1-k}}{(k!)} \tag{68}$$

for even coefficients, and

$$(2k{+}3)(2k{+}2)a_{(2k+3)} := -\sum_{j=0}^{2k+2} j(2k{+}3{-}j)a_j a_{(2k+3-j)} \quad \text{for odd ones.} \tag{69}$$

Although the index k is an integer number from zero to infinity, a_0 and a_1 are not defined by these recursion relations. Moreover, the sequence of a_k will be alternating polynomials of a_1 which can be seen in the first 5 terms

$$2\cdot 1\; a_2 = \; -\lambda - a_1^2\,, \tag{70}$$

$$3\cdot 2\; a_3 = 2\lambda a_1 + 2a_1^3\,, \tag{71}$$

$$4\cdot 3\; a_4 = -\left(\lambda^2 - 1\right) - 4\lambda a_1^2 - 3a_1^4\,, \tag{72}$$

$$5\cdot 4\; a_5 = \left(\frac{4}{3}\lambda^2 - \frac{2}{3}\right)a_1 + \frac{14}{3}\lambda a_1^3 + 3a_1^5\,, \text{ and} \tag{73}$$

$$6\cdot 5\; a_6 = -\left(\frac{2}{3}\lambda^3 - \frac{2}{3}\lambda + \frac{1}{2\kappa}\right) - \left(5\lambda^2 - 1\right)a_1^2 - \lambda a_1^4 - \frac{9}{2}a_1^6\,. \tag{74}$$

Notably, odd-numbered coefficients a_{2k+1} are functions of only odd powers of a_1 up to order $2k+1$ whereas even-numbered coefficients a_{2k} are functions of only even powers of a_1 up to order $2k$. Furthermore, a_6 is the first coefficient to explicitly include an order of the harmonic parameter κ. Demanding that in the large limit, the harmonic oscillator ground state is recovered, λ must tend to unity and the sequence elements $a_{k\neq 1}$ vanish. This implies a_1 and all odd-numbered coefficients vanish at least in the harmonic oscillator limit.

$$\lim_{\kappa\to\infty} \lambda = 1 \implies \lim_{\kappa\to\infty} a_k = \begin{cases} -\frac{\lambda}{2}, \text{ for } & k = 2 \\ 0, \text{ for } & k \neq 2 \end{cases} \tag{75}$$

Since real non-zero coefficients a_1 do not allow the norm of the wavefunction to remain finite, they are generally not a physical solution to the eigenvalue problem even outside the harmonic oscillator limit and a formal solution is found for the ground state. Then there is an operator $\hat{a}_G^\dagger$ that raises the ground state up to the first excited state and which can be used with its adjoint operator $\hat{a}$ to create the Hamiltonian up to a constant. Let $\hat{a}_G^\dagger$ be given in analogy to the harmonic oscillator solution by

$$\hat{a}_G^\dagger := \frac{1}{\sqrt{2}} B((m\omega/\hbar)^{\frac{1}{2}}\ \hat{x}) - \frac{i\hat{p}}{\sqrt{2m\hbar\omega}} \tag{76}$$

where B is a real polynomial in the dimensionless position operator, then its adjoint operator is

$$\hat{a}_G = \frac{1}{\sqrt{2}} B((m\omega/\hbar)^{\frac{1}{2}}\ \hat{x}) + \frac{i\hat{p}}{\sqrt{2m\hbar\omega}}\ . \tag{77}$$

The operator product which produced the number operator for the harmonic oscillator $\hat{a}^\dagger\hat{a}$ is supposed to make up the Hamiltonian operator up to the zero-point energy of the ground state

$$\frac{\hat{H}}{\hbar\omega} - \frac{\lambda}{2} = \hat{a}^\dagger\hat{a} = \frac{\hat{p}^2}{2m\hbar\omega} + \frac{B^2}{2} - \left[\frac{i\hat{p}}{\sqrt{2m\hbar\omega}}, \frac{B}{\sqrt{2}}\right] = \frac{\hat{p}^2}{2m\hbar\omega} + \frac{B^2}{2} + \frac{B'}{2}\ . \tag{78}$$

Connecting this with the definition of the Hamiltonian leads to the first order quadratic differential equation in B

$$0 = B' + B^2 - \frac{2V_G}{\hbar\omega} + \lambda \tag{79}$$

which has already been solved above in terms of the polynomial A if one identifies $B = A'$. This implies the solution to the Schrödinger equation has indeed given rise to a raising operator and a lowering operator which produce a polynomial sequence $c_n(x)$ from the ground state solution equivalent to the Hermite polynomials in the harmonic oscillator which will be the asymptotic limit for infinitely large κ by construction

$$c_n(x) := \exp(-A(x))\,[A' + \partial_x]^n \exp(A(x))\ . \tag{80}$$

Although the Schrödinger equation is thereby formally solved with appropriate boundary conditions determining a_0 and a_1 which fixes the formal solution of the wavefunction

$$\psi_n^G(x) = \left(\frac{m\omega}{\pi\hbar}\right)^{\frac{1}{4}} c_n((m\omega/\hbar)^{\frac{1}{2}}x) \exp(A(m\omega/\hbar)^{\frac{1}{2}}x)\ , \tag{81}$$

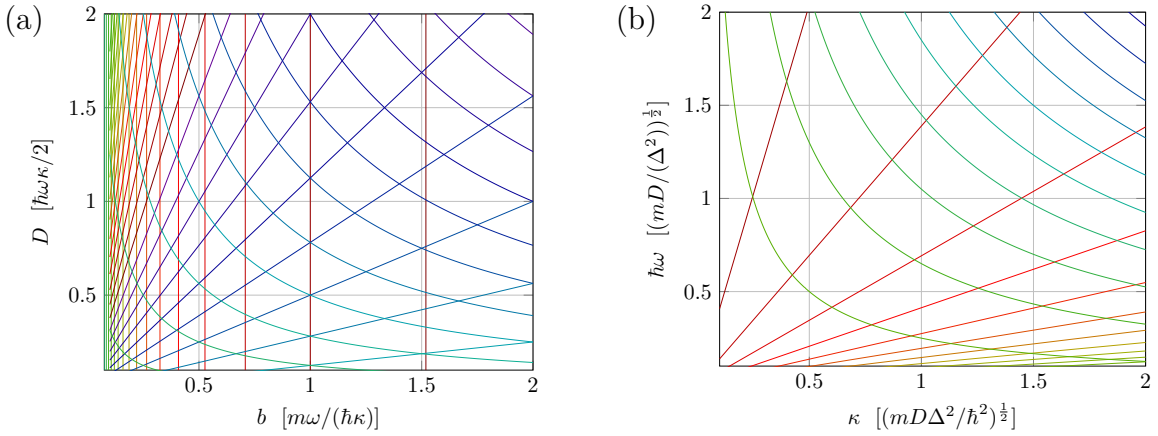

Figure 2: The relation between Gaussian well parameters. a) Contour lines against the description by threshold energy D and exponential coefficient b. Lines of equidistant constant harmonic oscillator energy $\hbar\omega$ show $1/b$ behaviour, lines of equidistant constant harmonic parameter κ show linear behaviour in b but their slope grows quadratically with κ, equidistant lines of constant standard deviations Δ represent lines of constant D but grow quadratically in distance. b) Respective contour lines in the Gaussian well description through harmonic oscillator energy $\hbar\omega$ and harmonicity parameter κ. Lines of constant equidistant threshold energy D show a $1/\kappa$ behaviour proportional to D, lines of constant equidistant Gaussian standard deviation Δ are linear in κ but quadratically grow in their ascent.

the zero-point and excitation energies have to depend to some extent on the harmonic parameter κ which indicates how strongly the potential resembles a harmonic oscillator. This dependence has not been determined at this point, nor do we know here how many eigenvalues we would expect to find below the continuum threshold.

It is further noteworthy, that while derived here with respect to parameter pair $(\hbar\omega, \kappa)$ representing the harmonic oscillator energy the resemblance factor of the Gaussian potential well with the harmonic oscillator, it is often numerically more straightforward to consider a tuple of continuum threshold energy and exponential coefficient (D, b). From a statistical viewpoint on Gaussian functions, one may also specify the same potential in terms of threshold energy and length scale of standard deviation (D, Δ). While they are all equivalent

$$V_G(x) = \frac{\hbar\omega\kappa}{2}(1-\exp(-(m\omega/(\kappa\hbar))x^2)) = D(1-\exp(-bx^2)) = D(1-\exp(-\tfrac{1}{2}(x/\Delta)^2)) \tag{82}$$

and the pair (D, b) is numerically most straightforward, they form curvilinear parameter systems with respect to each other. These relations are depicted in Figure 2 where the parameter systems $(\hbar\omega, \kappa)$ and (D, Δ) are drawn in the coordinate system of (D, b) and vice versa. If one of the two describing parameters is kept constant while the other is varied, this results in a motion along the depicted lines in parameter space. Any analysis of processes in dependence of Gaussian well parameters depends thereby strongly on the choice of parameter which means in turn that investigating a phenomenon with respect to one description might complicate its un-

derstanding, while the same phenomenon might show a straightforward behaviour in another representation. This will show the case in the analysis of numerical applications in Part III, where an alternative interpretation of the results is presented in terms of single-electron eigenfunctions which will then appear to primarily determine the efficiency of interatomic coulombic electron capture in a pair of quantum dots.

As it has just been shown, the Gaussian potential well is at least for large harmonic parameters κ closely resembling a harmonic oscillator potential and remains harmonic around the origin even for finite κ. The number of eigenlevels for a specific realisation of such a potential may thus be approximated quasi-classically to some reasonable extent by the so-called Wentzel-Kramers-Brillouin approximation which was named after the contributions of Wentzel,[101] Kramers,[102] and Brillouin,[103], sometimes also referencing Jeffreys who had studied a general approximation method two years earlier before the advent of the Schrödinger equation.[104] The approximation is, however, mathematically also known after the classical mathematicians Liouville and Green.[105,106] It reasons that a stationary solution to the Schrödinger equation needs to represent a standing wave of the form $\sin(px/\hbar)$ between the classical turning points x_1 and x_2 defined by the intersection of its eigenenergy with the potential

$$E_n - V(x_{1/2}) := 0 \,, \tag{83}$$

such that the closed integral over the momentum needs to be an integer multiple of 2π apart from a zero-point correction[107]

$$\sqrt{\tfrac{2m}{\hbar^2}} \oint\limits_{x_1,x_2} dx \, \sqrt{E_n - V(x)} = 2\pi \left(n + \tfrac{\lambda}{2}\right) \,. \tag{84}$$

This is known as the corrected Born-Sommerfeld condition, where $\frac{\lambda}{2}$ is the correction term arising from the purely quantum-mechanical phenomenon of the zero-point energy. Even though the system has not stored any quantum of energy, the quantum-mechanical limit to energetic and temporal resolution

$$\Delta_E \Delta_t \geq \frac{\hbar}{2} \tag{85}$$

known as Heisenberg's uncertainty relation dictates that the system energy is non-vanishing. The harmonic oscillator solution of $\lambda = 1$ in particular, is known as Maslov correction.[107]

For a Gaussian potential well, the turning points must be within $(-\infty, +\infty)$ and the eigenenergy is limited by the continuum threshold D. The maximal number $n_{\max}$ of bound eigenstates is thus estimated by the Gaussian integral

$$n_{\max} + \frac{\lambda}{2} \leq \sqrt{\tfrac{2m}{\pi\hbar^2}} \int\limits_{-\infty}^{\infty} dx \, \sqrt{D \exp[-bx^2]} = \sqrt{\tfrac{2mD}{\hbar^2 b}} = \kappa \tag{86}$$

which recovers the previously introduced harmonic parameter κ and offers an alternative interpretation as upper limit to the number of bound solutions ψ_n where

$$\left\{ n \in \mathbb{N} \mid n \leq \kappa - \tfrac{\lambda}{2} \right\} \,. \tag{87}$$

3.4 Asymmetric Pairs of Gaussian Wells

In non-local phenomena like interatomic coulombic electron capture, energy is transferred between particles over a certain distance. It is therefore of interest to consider a pair of Gaussian potential wells as host to such an exchange. While Gaussian functions find many numerical applications particularly due to their relatively fast decay in magnitude compared with a simple exponential function, they are analytically not vanishing for any finite distances from their centre. This implies that two Gaussian potential wells

$$V_{2G}(x) := -\frac{\hbar\omega_L\kappa_L}{2}\exp\left(-\frac{m\omega_L}{\kappa_L\hbar}\left(x+\frac{\mathscr{R}}{2}\right)^2\right) - \frac{\hbar\omega_R\kappa_R}{2}\exp\left(-\frac{m\omega_R}{\kappa_R\hbar}\left(x-\frac{\mathscr{R}}{2}\right)^2\right) \tag{88}$$

with threshold energies $\hbar\omega_L\kappa_L/2$ and $\hbar\omega_R\kappa_R/2$ at finite centre-to-centre distance $\mathscr{R}$ will have a potential barrier between each which is energetically lower than the respective continuum threshold energy.

Generally, the potential barrier is not situated at the centre of both wells. Moreover, it can be shown that in the harmonic limit, the barrier vanishes and the potential will asymptotically tend to the behaviour of a harmonic oscillator

$$V_{2HO}(x) = \frac{m}{2}\left(\omega_L^2+\omega_R^2\right)\left(x+\frac{\omega_L^2-\omega_R^2}{\omega_L^2+\omega_R^2}\frac{\mathscr{R}}{2}\right)^2 \tag{89}$$

with modified oscillator frequency

$$\omega_{2HO} = \sqrt{\omega_L^2+\omega_R^2} \tag{90}$$

and its central position shifted along the x axis to

$$x_0 = \frac{\omega_R^2-\omega_L^2}{\omega_R^2+\omega_L^2}\frac{\mathscr{R}}{2}\,. \tag{91}$$

Avoiding the analytically challenging treatment of the pair of Gaussians wells, it is possible, however, to identify two competing length scales in the exponential function. On the one hand, there is the characteristic distance from the centre of a Gaussian function over which it reduces to approximately 61% ($e^{-1/2}$) of it's maximal value at the centre, the standard deviation Δ. In a distance of 2Δ from the Gaussian centre, the exponential has decayed to 14% ($e^{-1/8}$), and at 3Δ to a remaining 1.1% ($e^{-1/18}$) of continuum threshold energy. The distance $\mathscr{R}$, on the other hand, sets the two potential wells apart from each other. It is thus straightforward to study the ratio between the distance over which the potentials reach continuum and the distance over which a particle must travel from one potential to the other. Going over to the equivalent description by threshold energy $D_{L/R}$ and standard deviation Δ and factoring out the centre-centre distance, the double potential becomes a function of the rescaled position $x/\mathscr{R}$

$$V_{2G}(x) = -D_L\exp\left(-\tfrac{1}{2}\left(\tfrac{\mathscr{R}}{\Delta_L}\right)^2\left(\tfrac{x}{\mathscr{R}}+\tfrac{1}{2}\right)^2\right) - D_R\exp\left(-\tfrac{1}{2}\left(\tfrac{\mathscr{R}}{\Delta_R}\right)^2\left(\tfrac{x}{\mathscr{R}}-\tfrac{1}{2}\right)^2\right)\,. \tag{92}$$

The distance $\mathscr{R}$ can then be partitioned equally in both standard deviations Δ_L and Δ_R such that

$$\mathscr{R} = \eta(\Delta_L + \Delta_R) \tag{93}$$

where η is a positive real number. Let $\Delta_\pm$ denote the sum and difference

$$\Delta_\pm := \Delta_L \pm \Delta_R \tag{94}$$

between both standard deviations respectively and the potential at that position of equal partition in both deviations is given by

$$V_{2G}\left(\tfrac{\mathscr{R}}{2}\tfrac{\Delta_-}{\Delta_+}\right) = -(D_L + D_R)\ \exp[-\eta^2/2]\ . \tag{95}$$

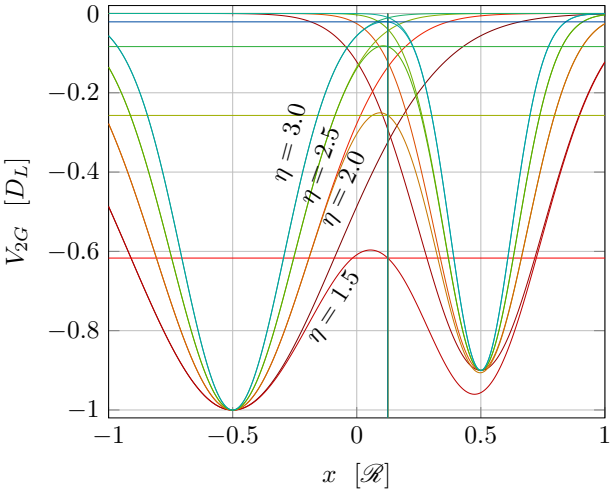

Figure 3: Asymmetric pairs of Gaussian wells and their potential barrier height in dependence on the ratio η between well-to-well distance $\mathscr{R}$ and sum of individual standard deviations Δ_L and Δ_R. The approximated barrier height according to the description in the main text is indicated by horisontal coloured lines. The estimates for barrier position and height improve with increasing η.

As depicted in Figure 3 for one example of varying η at increasing separation, the barrier position and its difference with respect to the continuum threshold can be well estimated by Eq. (95). It appears obvious that one can only talk of well separated potentials if $\eta > 2$ which still corresponds to 14% remaining difference between barrier and continuum. One might therefore even consider $3\Delta_+$ to be a suitable lower bound in centre-to-centre distance, corresponding to a remaining barrier-continuum difference of about 2.2% of the average threshold energy of 0.5 $(D_L{+}D_R)$.

3.5 The Hydrogen Problem in Various Coordinate Systems

The second fundamental problem of quantum mechanics lying at the heart of a dynamical description of interatomic coulombic electron capture is the hydrogen problem. Known in classical mechanics and electrodynamics as a centrally symmetric potential field, the Coulomb potential[108]

$$V_C(r) = -\frac{Ze^2}{4\pi\varepsilon r} \tag{96}$$

describes the potential energy of an elementary charge e at distance r from a central charge $-Ze$ where Z is the charge number, and ϵ is the electric permittivity in medium usually given by the product of ϵ_0, the electric permittivity in vacuum and ϵ_r, the relative permittivity of a medium.

The radial distance r is given in three-dimensional Cartesian space by the vector length of the position vector $\vec{r} = (x, y, z)$ as $r = \sqrt{x^2 + y^2 + z^2}$ but is a vector component itself in spherical polar coordinates where $\vec{r} = (r, \vartheta, \varphi)$ is given by the vector length r and its direction via polar angle ϑ and azimuthal angle φ. The kinetic energy operator in position basis representation of spherical polar coordinates is written as[109,98]

$$-\frac{2m}{\hbar^2}\hat{T} = \frac{1}{r}\,\partial_r^2\; r - r^{-2}\hat{\ell}^2 \tag{97}$$

where the angular momentum operator is[109]

$$\hat{\ell}^2 = -\frac{1}{\sin\vartheta}\;\partial_\vartheta\;\sin\vartheta\;\partial_\vartheta - \frac{1}{\sin^2\vartheta}\;\partial_\varphi^2\,. \tag{98}$$

3.5.1 Atomic Hartree and Rydberg units

In analogy to the characteristic units of the harmonic oscillator, the energy of the system is expected to be some multiple of $\hbar\omega$ for some appropriate angular frequency. Then the potential energy is

$$V_C(r) = -\hbar\omega\left(\frac{Ze^2}{4\pi\epsilon\hbar\omega r}\right) \tag{99}$$

where the ratio within the brackets is dimensionless and according to Eq. (52) equivalent to

$$\left(\frac{Ze^2}{4\pi\epsilon\hbar\omega r}\right)^2 = \left(\frac{\hbar}{m\omega}\frac{1}{r^2}\right) \tag{100}$$

which implies a characteristic mass m and a characteristic energy of

$$E_H := \hbar\omega = m\left(\frac{Ze^2}{4\pi\epsilon\hbar}\right)^2\,. \tag{101}$$

This reintroduced into the Coulomb potential

$$V_C(r) = -\hbar\omega\left(\frac{4\pi\epsilon\hbar^2}{mZe^2}\;r^{-1}\right) =: -\hbar\omega\left(\frac{a_B}{r}\right) \tag{102}$$

leads to the characteristic length

$$a_B = \frac{4\pi\epsilon\hbar^2}{mZe^2}\,. \tag{103}$$

In the case of hydrogen, the nuclear charge number is $Z = 1$, the electric permittivity is that of the vacuum ϵ_0 and the mass relates to the electron rest mass m_e. The characteristic length a_B is then called the Bohr radius. However, for various systems, an analogue to the Bohr radius remains a suitable unit of length which incorporates

a modified mass, charge number or permittivity giving rise to an effective Bohr radius. As a result, this redefines the characteristic energy as

$$E_H = \frac{\hbar^2}{m\ {a_B}^2}\,. \tag{104}$$

which is known as the Hartree energy. Together, they make up the natural units of the hydrogen problem and are thus often abbreviated by 'a.u.' for atomic units of time, energy, length or other quantities. The quantum mechanical equations are often transformed into atomic units by formally setting the four constants $\hbar = m_e = (4\pi\epsilon)^{-2} = e = 1$ to unity. This gravely simplifies the physical equations but demands care in interpretation of the respective quantities. For example, the canonical kinetic energy-momentum relation $\hat{T} = \hat{p}^2/(2m)$ implies a characteristic momentum scale of

$$\check{p} = \frac{\sqrt{2\hbar^2}}{a_B} = \sqrt{2mE_H} \tag{105}$$

while the full kinetic energy operator in spherical polar position basis representation is

$$\hat{T} = \hbar\omega \left(\left(\frac{a_B}{\sqrt{2\hbar^2}}\ \hat{p}_r \right)^2 + \left(\frac{a_B}{r} \right)^2 \frac{\hat{\ell}^2}{2} \right)\,. \tag{106}$$

This is expressed in atomic (Hartree) units with omitted unit constants as

$$\hat{T} = \frac{\hat{p}_r^2}{2} + \frac{\hat{\ell}^2}{2r^2}\,. \tag{107}$$

However, there is a second system of atomic units, both of which have developed from historical reasons. While the above are the atomic Hartree units, one can alternatively use half-integers of energy quanta $\hbar\omega$ as reference in analogy to the harmonic oscillator zero-point energy. This defines a Rydberg energy as

$$\mathrm{Ry} = \frac{\hbar\omega}{2} = \frac{m}{2} \left(\frac{Z(2e^2)}{8\pi\epsilon\hbar} \right)^2\,. \tag{108}$$

The potential Coulomb potential is then given in terms of the Rydberg energy as

$$V_C(r) = -2\mathrm{Ry} \left(\frac{a_B}{r} \right)\,. \tag{109}$$

This gives rise to the system of atomic Rydberg units which arise formally by assigning the units of reference $\hbar = m_e/2 = (4\pi\epsilon)^{-2} = 2e^2 = 1$ If the kinetic energy operator in spherical polar position representation is given in atomic Rydberg units,

$$\hat{T} = \hat{p}_r^2 + \hat{\ell}^2 r^2 \tag{110}$$

it differs from the expression in the atomic Hartree units by a factor of one half. This explains why care has to be taken when dealing with equations in atomic units. Although they allow to omit most natural constants which simplifies equations, the physical interpretation of an entity can be complicated when its units cannot be sufficiently deduced from the surrounding constants in an equation. Furthermore,

both unit systems are a special case of Coulomb units where mass, length and time are respectively set to units of m, $\hbar^2/(m\alpha)$ and $\hbar^3/(m\alpha^2)$ for appropriate constants α.[109] To make use of the atomic units particularly during the numerical applications in Part III while retaining the clarity in interpretation, the atomic units of length, energy and action shall be presented in scales of by the (effective) Bohr radius a_B, the Hartree energy E_H and the reduced Planck constant $\hbar$ rather than using the common but nondescript 'a.u.' for all entities.

3.5.2 Normalised Wavefunctions

Since the Coulomb potential does not depend on the angular components of the position vector, a stationary solution of the angular momentum operator is a free-particle solution of the angular coordinates

$$\hat{\ell}^2 \; Y_\ell^{m_\ell}(\vartheta,\varphi) = \ell(\ell+1) Y_\ell^{m_\ell}(\vartheta,\varphi) \tag{111}$$

with eigenvalue $\ell(\ell+1)$ and gives rise to the spherical harmonic functions with angular-momentum quantum number ℓ and magnetic quantum number m_ℓ. The stationary wavefunction of the Coulomb potential in position basis representation of spherical polar coordinates is thereby a product of a radial function $R_{n,l}(r)$ depending only on the radial distance r for a given angular momentum ℓ and an angular function $Y_\ell^{m_\ell}(\vartheta,\varphi)$ independent of r

$$\psi^C_{n,\ell,m_\ell}(r,\vartheta,\varphi) = R_{n,\ell}(r) Y_\ell^{m_\ell}(\vartheta,\varphi) \; . \tag{112}$$

Spherical polar coordinates are an example of an orthogonal non-Cartesian coordinate system. This means the Jacobian determinant

$$|\mathscr{J}_s|^2 := \det\left(\frac{\partial(x,y,z)}{\partial(r,\vartheta,\varphi)}\right) = r^2 \sin\vartheta \tag{113}$$

is not a constant but rather depends on the position itself. As the differential volume element

$$d^3\vec{r} = dx \; dy \; dz = |\mathscr{J}|^2 dx_1 \; dx_2 \; dx_3 \; , \tag{114}$$

in any three-dimensional system of general coordinates $\vec{r} = (x_1, x_2, x_3)$ dependent on the Jacobian

$$|\mathscr{J}|^2 := \det\left(\frac{\partial(x,y,z)}{\partial(x_1,x_2,x_3)}\right) \; , \tag{115}$$

the norm of a wavefunction in that coordinate representation

$$\Big\langle \psi \;\Big|\; \psi \Big\rangle = \iiint d^3\vec{r} \; \psi^*\psi = \iiint dx_1 \; dx_2 \; dx_3 \; (\psi\mathscr{J})^* \; (\mathscr{J}\psi) \tag{116}$$

suggests a substitution

$$u_{\mathscr{J}}(x_1,x_2,x_3) := \mathscr{J}(x_1,x_2,x_3)\psi(x_1,x_2,x_3) \tag{117}$$

which incorporates the non-Cartesian aspect of the volume element into the new wavefunction $u_{\mathscr{J}}$ as

$$\Big\langle \psi \;\Big|\; \psi \Big\rangle = \iiint dx \; dy \; dz \; |\psi(x,y,z)|^2 = \iiint dx_1 \; dx_2 \; dx_3 \; |u_{\mathscr{J}}(x_1,x_2,x_3)|^2 \; . \tag{118}$$

The wavefunction $u_{\mathscr{J}}(x_1, x_2, x_3)$ is often called the *normalised wavefunction* of the problem. At the same time, the expectation values of operators must remain conserved under this transformation. This necessitates an associated transformation of an operators $\hat{O}$. Their action on a normalised wavefunction

$$\mathscr{J}\,(\hat{O}\psi) =: \hat{O}_{\mathscr{J}}(\,\mathscr{J}\,\psi) = \hat{O}_{\mathscr{J}}\,u_{\mathscr{J}} \tag{119}$$

thereby defines a *normalised operator*

$$\hat{O}_{\mathscr{J}} := \mathscr{J}\,\hat{O}\,\mathscr{J}^{-1} \tag{120}$$

which conserves the expectation values

$$\left\langle \psi \;\middle|\; \hat{O} \;\middle|\; \psi \right\rangle = \iiint dx\ dy\ dz\ \psi^*\ \hat{O}\psi = \iiint dx_1\ dx_2\ dx_3\ u^*_{\mathscr{J}}\ \hat{O}_{\mathscr{J}}\,u_{\mathscr{J}} \tag{121}$$

and more generally conserves the matrix elements. For spherical polar coordinates, the normalised kinetic energy operator is therefore

$$-\frac{2m}{\hbar}\hat{T}_s = \partial_r^2 + r^{-2}\underbrace{\left(\partial_\vartheta^2 + \tan\vartheta\ \partial_\vartheta + \frac{1}{\sin^2\vartheta}\partial_\varphi^2\right)}_{=-\hat{\ell}_s^2}\,. \tag{122}$$

The radial Schrödinger equation for the Coulomb potential is then[109]

$$\frac{d^2u_{n,\ell}(r)}{dr^2} + \frac{2m}{\hbar^2}\left(E_n + \frac{\kappa}{r} - \frac{\ell(\ell+1)}{r^2}\right)u_{n,\ell}(r) = 0 \tag{123}$$

which is related to the associated Laguerre differential equation[109,110]

$$0 = xu'' + (x+1)u' + \left(n + \tfrac{\ell}{2} + 1 - \frac{\ell^2}{4x}\right)u\,, \text{ with solutions of the form} \tag{124}$$

$$u = L_n^\ell(x)x^{\frac{\ell}{2}}\exp[-x] \tag{125}$$

where $L_n^\ell(x)$ are the associated Laguerre polynomials

$$L_n^\ell(x) = \frac{1}{n!}\sum_{i=0}^{n}\frac{n!}{i!}\binom{\ell+n}{n-i}(-x)^i \tag{126}$$

for different boundary conditions given by quantum number ℓ. The associated Laguerre polynomials and the functions u provide essential ingredients to the numerical implementation in spherical and cylindrical coordinates which is used later in Part III.

The alternative normalised wavefunction for a spherical polar description is thus composed as

$$\psi_s(r,\theta,\varphi) = u_{n,\ell}(r)Y_\ell^{m_\ell}(\theta,\varphi)\ , \text{ with} \tag{127}$$

$$u_{n,\ell}(r) = r\ R_{n,\ell}(r) \text{ and} \tag{128}$$

$$Y_\ell^{m_\ell}(\theta,\varphi) = \sqrt{\sin\theta}\ Y_\ell^{m_\ell}(\theta,\varphi) \tag{129}$$

which swallows the spherical volume element $r^2\sin\theta$.

As opposed to the harmonic oscillator in one Cartesian coordinate, the hydrogen problem offers three degrees of freedom and stationary states are thus characterised by three quantum numbers. Furthermore, the stationary states of the Coulomb field are $(2\ell+1)$-fold degenerate, which means linearly independent solutions of same eigenvalue arise. This generally indicates the presence of an additional conserved quantity of which the representing operator does not commute with those defining the stationary solutions of the problem.[109]

4 Non-Interactive Dynamics

It has been shown briefly that a scattering process like interatomic coulombic electron capture is partly governed by the independent dynamics of the involved particles giving rise to free Hamiltonian and partly by the interaction between those particles which gives rise to an interaction Hamiltonian. It was further shown, that Gaussian functions arise naturally from the harmonic oscillator problem and may describe a normal distributed probability distribution in space. Similarly, they may present a many-body averaged potential acting on a remaining particle which in the case of the established quantum-dot system describes a cumulative effective confinement potential exerted from the multiatomic region of varying material composition onto an incident electron.[8] Eventually, the normalisation of wavefunctions and operators with respect to chosen coordinate systems has been discussed in order to account for the appearing volume elements and has been applied to sketch the separation of variables and the solution of the hydrogen problem which also introduced the Coulomb potential.

In light of these concepts, the independent dynamics of a free electron wavepacket shall be considered here in a single dimension and then later be generalized to describe the dynamics of a cylindrical electron distribution moving along the cylinder axis. It will be derived how a wavepacket is distributed in momentum and energy space and how it evolves in time time. This will provide the foundation to the analysis of flux density spectra associated with interatomic coulombic electron capture in quantum dot systems and ultracold atoms which will be discussed in Part III.

4.1 A Free Electron (Gaussian Wavepacket)

Assuming a motion along a single axis which shall be denoted by z, a free electron may generally be found at time $t = 0$ with some uncertainty spatial Δ_z around a position z_0 moving at a group velocity p_0/m. Then the wavefunction may be estimated by a Gaussian function

$$\phi_0(z) := \mathscr{N}_\phi \exp\left[-\frac{(z-z_0)^2}{4\Delta_z^2} + ik_0(z-z_0)\right] \tag{130}$$

where $\mathscr{N}_\phi$ is a normalisation factor and k_0 is the wavenumber related to the group velocity by $\hbar k_0/m = p_0/m$. The Fourier transformation with respect to position of the initial state in position basis representation that is the wavefunction $\left\langle z \,\middle|\, \phi_0 \right\rangle = \phi_0(z)$ transforms the expression into the momentum basis representation of the free

electron state which shall be denoted by $\left\langle p/\hbar \,\middle|\, \phi_0 \right\rangle =: A(k)$ and expressed in terms of the wavenumber $k = p/\hbar$. As the wave packet is initially centered at z_0, we may shift the axis linearly by $+z_0$ such that the Fourier transform into k-space may be written as

$$A(k) := \frac{\mathscr{N}_A}{\mathscr{N}_\phi} \int_{-\infty}^{\infty} dz \;\; \phi(z) \;\; \exp[-ik(z - z_0)] \,, \tag{131}$$

such that we can then identify $z' := z - z_0$ and substitute $dz = dz'$.

$$A(k) = \mathscr{N}_A \int_{-\infty}^{\infty} dz \;\; \exp\left[-\frac{(z - z_0)^2}{4\Delta_z^2} + i(k - k_0)(z - z_0) \right] \tag{132}$$

$$= \mathscr{N}_A \int_{-\infty}^{\infty} dz' \;\; \exp\left[-\frac{(z')^2}{4\Delta_z^2} + i(k - k_0)(z') \right] \tag{133}$$

As we complete the square in the form of $-a(x+b)^2 + c = -ax^2 - 2abx - ab^2 + c$ with

$$-\frac{1}{4\Delta_z^2} z'^2 - i(k - k_0)z' = -\frac{1}{4\Delta_z^2} \left(z' + i2\Delta_z^2(k - k_0) \right)^2 - \Delta_z^2 (k - k_0)^2, \tag{134}$$

we find

$$A(k) = \mathscr{N}_A \exp\left[-\Delta_z^2 (k - k_0)^2 \right] \int_{-\infty}^{\infty} dz' \;\; \exp\left[-\frac{1}{4\Delta_z^2} \left(z' + i2\Delta_z^2(k - k_0) \right)^2 \right] \tag{135}$$

and substitute $z' \mapsto z'' := z' + i2\Delta_z^2(k - k_0)$, and consequently $dz'' = dz'$.

$$\begin{aligned} A(k) &= \mathscr{N}_A \exp\left[-\Delta_z^2 (k - k_0)^2 \right] \underbrace{\int_{-\infty}^{\infty} dz'' \;\; \exp\left[-\frac{1}{4\Delta_z^2} (z'')^2 \right]}_{\cdot \sqrt{4\pi\Delta_z^2}} \\ &= \mathscr{N}_A \exp\left[-\Delta_z^2 (k - k_0)^2 \right] \end{aligned} \tag{136}$$

In consequence, the wavefunction in the so-called k-space can be written as

$$\boxed{A(k) = \mathscr{N}_A' \exp\left[-\Delta_z^2 (k - k_0)^2 \right] = \left(\tfrac{2\Delta_z^2}{\pi} \right)^{\frac{1}{4}} \exp\left[-\Delta_z^2 (k - k_0)^2 \right]} \tag{137}$$

where we identify the normalisation factor

$$\mathscr{N}_A' = \left(\frac{2\Delta_z^2}{\pi} \right)^{\frac{1}{4}} \tag{138}$$

from the normalisation condition of

$$1 \stackrel{!}{=} \int_{-\infty}^{\infty} dk \;\; |A(k)|^2 = |\mathscr{N}_A'|^2 \int_{-\infty}^{\infty} dk \;\; \exp\left[-2\Delta_z^2 (k - k_0)^2 \right] = |\mathscr{N}_A'|^2 \sqrt{\tfrac{\pi}{2\Delta_z^2}} \,. \tag{139}$$

4.1.1 Energy Distribution Density

In the following, the energy distribution of the free electron wavepacket shall be found. Relating energy $E = \hbar\omega$ with momentum $p = \hbar k$ by the dispersion relation $E = \frac{p^2}{2m}$ for a massive particle, a second order Taylor expansion leads to the expression,

$$\omega(k) = \omega|_{k_0} + \left.\frac{d\omega}{dk}\right|_{k_0}(k-k_0) + \frac{1}{2}\left.\frac{d^2\omega}{dk^2}\right|_{k_0}(k-k_0)^2 \quad \text{which equates to} \tag{140a}$$

$$\omega(k) = \frac{\hbar k_0^2}{2m} + \frac{\hbar k_0}{m}(k-k_0) + \frac{\hbar}{2m}(k-k_0)^2 \quad \text{and transforms into} \tag{140b}$$

$$(k-k_0) = \pm\sqrt{\tfrac{2m}{\hbar}\omega} - k_0\,. \tag{140c}$$

Assuming wavenumbers $k, k_0 \in \mathbb{R}$ to be real numbers, $\omega = k^2/(2m)$ implies the angular frequency is positive $\omega > 0$. Identifying the infinitesimal change in wavenumber by

$$dk = \pm\frac{1}{2}\sqrt{\frac{2m}{\hbar\omega}}d\omega, \text{ for } k \gtrless 0\,, \tag{141}$$

the normalisation condition of the momentum distribution $A(k)$ can be expressed in terms of angular frequency via

$$1 = \int_{-\infty}^{\infty} dk\ \Big|A(k)\Big|^2 \tag{142}$$

$$= \int_0^{\infty}\frac{d\omega}{\sqrt{\omega}}\sqrt{\frac{2m}{\hbar}}\frac{1}{2}\Big|A\Big(-\sqrt{2m\omega/\hbar}\Big)\Big|^2 + \int_0^{\infty}\frac{d\omega}{\sqrt{\omega}}\sqrt{\frac{2m}{\hbar}}\frac{1}{2}\Big|A\Big(+\sqrt{2m\omega/\hbar}\Big)\Big|^2 \tag{143}$$

$$= \int_0^{\infty} d\omega\ \underbrace{\sqrt{\frac{2m}{\hbar\omega}}\left(\tfrac{1}{2}\Big|A\Big(-\sqrt{2m\omega/\hbar}\Big)\Big|^2 + \tfrac{1}{2}\Big|A\Big(+\sqrt{2m\omega/\hbar}\Big)\Big|^2\right)}_{\Big|D(\omega)\Big|^2} \tag{144}$$

$$= \int_0^{\infty} d\omega \overbrace{\sqrt{\frac{2m}{\hbar\omega}}\left(\frac{2\Delta_z^2}{\pi}\right)^{\frac{1}{2}}\begin{pmatrix}\frac{1}{2}\exp\Big[-2\Delta_z^2\Big(k_0+\sqrt{2m\omega/\hbar}\Big)^2\Big] \\ +\frac{1}{2}\exp\Big[-2\Delta_z^2\Big(k_0-\sqrt{2m\omega/\hbar}\Big)^2\Big]\end{pmatrix}}^{} \tag{145}$$

Consequently, the normalised energy distribution $D(\omega)$ is given by

$$\boxed{\Big|D(\omega)\Big|^2 = \sqrt{\tfrac{m\Delta_z^2}{\pi\hbar\omega}}\left(\exp\Big[-2\Delta_z^2\Big(k_0+\sqrt{2m\omega/\hbar}\Big)^2\Big] + \exp\Big[-2\Delta_z^2\Big(k_0-\sqrt{2m\omega/\hbar}\Big)^2\Big]\right)} \tag{146}$$

4.1.2 Time Evolution in one Dimension

Eventually, the evolving wavefunction in space and time $\phi(z,t)$ represents the Fourier transform of the wavefunction $A(k)$ in k-space with the approach

$$\phi(z,t) = \frac{\mathscr{N}_\phi}{\mathscr{N}_A}\int_{-\infty}^{\infty} A(k)\,\exp\Big[i(k(z-z_0)-\omega(k)t)\Big]dk\,. \tag{147}$$

Using the Taylor expansion of $\omega(k)$ according to Eq. (140), it follows that

$$\phi(z,t) = \mathscr{N}_\phi \int_{-\infty}^{\infty} dk \exp\Big[-\Delta_z^2(k-k_0)^2 + ik(z-z_0) - i\left(\omega_0 + \tfrac{\hbar k_0}{m}(k-k_0) + \tfrac{\hbar}{2m}(k-k_0)^2\right)t\Big] \tag{148}$$

where a first substitution of $k' := k - k_0$ and $dk' = dk$ leads to

$$f(z,t) = \mathscr{N}_\phi \exp\left[i(k_0(z-z_0) - \omega_o t)\right] \int_{-\infty}^{\infty} dk' \exp\Big[-\left(\Delta_z^2 + \tfrac{i\hbar}{2m}t\right)k'^2 + i\left(z - z_0 - \tfrac{\hbar k_0}{m}t\right)k'\Big] \,. \tag{149}$$

From where further substitution with

$$\Delta_z\alpha := \Delta_z^2 + \frac{i\hbar}{2m}t \tag{150}$$

$$x := z - z_0 - \frac{\hbar k_0}{m}t \tag{151}$$

$$k'' := k' - \frac{ix}{2\Delta_z\alpha} \tag{152}$$

introduces a complex time-dependent quantity α, a time-dependent position x and a time-dependent wavenumber k'' such that the wavefunction is expressed in

$$f(z,t) = \mathscr{N}_\phi \exp\left[i(k_0 x + \omega_0 t) - \frac{x^2}{4\Delta_z\alpha}\right] \int_{-\infty}^{\infty} dk'' \exp\left[-\Delta_z\alpha k''^2\right] \tag{153}$$

which involves a Gaussian integral in k'' and thereby reduces to

$$= \mathscr{N}_\phi \exp\left[i(k_0 x + \omega_0 t) - \frac{x^2\alpha^*}{4\Delta_z|\alpha|^2}\right] \sqrt{\frac{\pi\alpha^*}{\Delta_z|\alpha|^2}} \,. \tag{154}$$

It is noteworthy that $\alpha(t)$ is a complex number growing with time and its real part $\Re(\alpha) = \Delta_z$ represents the initial standard deviation in the electron's spatial probability density. Deducing at last the factor $\mathscr{N}_\phi$ from the normalisation condition.

$$1 \overset{!}{=} \int_{-\infty}^{\infty} dz \; |f(z,t)|^2 = \int_{-\infty}^{\infty} dz \; f^* f(z,t) \tag{155}$$

$$= \left|\mathscr{N}_\phi\right|^2 \sqrt{\tfrac{\pi^2}{\Delta_z^2|\alpha|^2}} \int_{x=-\infty}^{\infty} dx \; \exp\left[-\tfrac{\Delta_z x^2}{2\Delta_z|\alpha|^2}\right] = \left|\mathscr{N}_\phi\right|^2 \sqrt{\tfrac{\pi^2}{\Delta_z^2|\alpha|^2}} \sqrt{2\pi|\alpha|^2} \tag{156}$$

yields a time-independent normalisation factor which depends solely on the initial spatial uncertainty by

$$\left|\mathscr{N}_\phi\right|^2 = \sqrt{\frac{\Delta_z^2}{2\pi^3}} \,. \tag{157}$$

Summarising, the Gaussian wavepacket describing a free electron moving in one direction increases monotonously with time in its spatial uncertainty given by $|\alpha(t)| \geq \Delta_z$ and in its central position $Z(t)$ which is moving with group velocity $\hbar k_0/m$ through space from its initial position z_0 at time $t = 0$:

$$\alpha(t) = \Delta_z + i\frac{\hbar t}{2m} \tag{158a}$$

$$Z(t) = z_0 + \frac{\hbar k_0}{m} t \tag{158b}$$

$$f(z,t) = \frac{1}{(2\pi)^{\frac{1}{4}}\alpha(t)} \exp\left[-\frac{(z-Z(t))^2}{4\Delta_z \alpha(t)} + i\left(k_0(z-Z(t)) + \tfrac{\hbar k_0^2}{2m}t\right)\right] \tag{158c}$$

$$\left|f(z,t)\right|^2 = \frac{\exp\left[-\frac{(z-Z(t))^2}{2|\alpha(t)|^2}\right]}{\sqrt{2\pi|\alpha(t)|^2}} \tag{158d}$$

At initial time $t = 0$ the uncertainty is thus at a minimum which is why it is known as a minimum-uncertainty wavepacket such that the Heisenberg uncertainty relation $\Delta_z \Delta_k \geq \frac{1}{2}$ is fulfilled for all time.

4.2 Free Electrons in three Dimensions

In the following, the free electron shall be able to move in three directions but remain described by a Gaussian wavepacket at time $t = 0$. This generalizes the previous considerations and will allow to move from the established quasi-one-dimensional model for ICEC in quantum dots to a higher dimensional description of a free electron heading for an ion in a cloud of ultracold atoms. Primary quantities of interest are the independent evolution of the wavepacket and its energy distribution. For determining the momentum an energy distribution attached to a free three-dimensional wavepacket representing a freely moving electron in space, three-dimensional vectors need to be Fourier transformed as

$$A(\vec{k}) := \frac{\mathscr{N}_A}{\mathscr{N}_\phi} \iiint_{\mathbb{R}^3} d^3\vec{x}\ \ \phi(\vec{x}) \exp\left[-i\vec{k}\cdot(\vec{x}-\vec{x}_0)\right] . \tag{159}$$

The volume element $d^3\vec{x}$ in Euclidean space is dependent on the chosen coordinate system which was discussed in context of the hydrogen problem. The initial wavefunction $\phi(\vec{x})$ of position vector $\vec{x}$ shall now be assumed to compose from a Hartree product of functions with single degrees of freedom

$$\phi(\vec{x}) = f_{x_1}(x_1) f_{x_2}(x_2) f_{x_3}(x_3) . \tag{160}$$

Under this assumption of separability of the initial wavefunction, the momentum distribution density $A(\vec{k})$ is also a Hartree product from functions with single degrees of freedom. In Cartesian coordinates $\vec{x} = (x, y, z)$, the wavefunction in k-space

constitutes of

$$A(\vec{k}) = \underbrace{\int_{-\infty}^{\infty} dx\ f_x(x) \exp[-ik_x(x-x_0)]}_{A_x(k_x)} \underbrace{\int_{-\infty}^{\infty} dy\ f_y(y) \exp[-ik_y(y-y_0)]}_{A_y(k_y)} \underbrace{\int_{-\infty}^{\infty} dz\ f_z(z) \exp[-ik_z(z-z_0)]}_{A_z(k_z)} . \tag{161}$$

For which a spherical initial wavepacket with group velocity along the z-axis is described by

$$f_x(x) := \mathscr{N}_f^{-\frac{1}{3}} \exp\left[-\tfrac{(x-0)^2}{4\Delta_z^2}\right], \tag{162a}$$

$$f_y(y) := \mathscr{N}_\phi^{-\frac{1}{3}} \exp\left[-\tfrac{(y-0)^2}{4\Delta_z^2}\right] \text{ and} \tag{162b}$$

$$f_z(z) := \mathscr{N}_\phi^{-\frac{1}{3}} \exp\left[-\tfrac{(z-z_0)^2}{4\Delta_z^2} + ik_0(z-z_0)\right] . \tag{162c}$$

This implies a momentum distribution density as product of component-wise contributions according to Eq. (137).

$$A(\vec{k}) = \left(\tfrac{2\Delta_z^2}{\pi}\right)^{\frac{3}{4}} \exp\left[-\Delta_z^2\left(k_x^2 + k_y^2 + (k_z-k_0)^2\right)\right] \tag{163}$$

This solution is symmetric in x and y direction. In other words, it has cylindrical symmetry with respect to the z axis. In cylindrical coordinates $\vec{x} = (\rho, \varphi, z)$, then momentum distribution has two degrees of freedom and is independent of the angular component. Moreover for vanishing group velocity $k_0 = 0$, this $\left|A(\vec{k})\right|^2$ corresponds to a Maxwell-Boltzmann momentum distribution of temperature $T = \hbar^2/(4mk_B\Delta_z^2)$.

$$\boxed{A(\vec{k}) = \left(\frac{2\Delta_z^2}{\pi}\right)^{\frac{3}{4}} \exp\left[-\Delta_z^2\left(k_\rho^2 + (k_z-k_0)^2\right)\right]} \tag{164}$$

4.2.1 Energy Distribution Density

The analogous many-dimensional approach to derive the energy distribution density is formally given by the simple equation

$$d^3\vec{k}\ \left|A(\vec{k})\right|^2 = d\omega\ \left|D(\omega)\right|^2, \tag{165}$$

such that the normalisation is conserved as over the transformation between wavevector $\vec{k}$ and angular frequency ω

$$1 \overset{!}{=} \int_{\mathbb{R}^3} d^3\vec{k}\ \left|A(\vec{k})\right|^2 = \int_0^\infty d\omega\ \left|D(\omega)\right|^2, \tag{166}$$

where the generalised wavevector $\vec{k}$ has the magnitude $k = \sqrt{k_\rho^2 + k_z^2}$ in cylinder coordinates of reciprocal space. Assuming an angular vector component k_φ pointing in

azimuthal direction, one can translate the wavevector from a cylindrical coordinate system where $\vec{k} = (k_z, k_\rho, k_\varphi)$ into a spherical coordinate system $\vec{k} = (k, k_\vartheta, k_\varphi)$ such that

$$k_z = k \cos k_\vartheta \tag{167a}$$
$$k_\rho = k \sin k_\vartheta \tag{167b}$$
$$k_\varphi = k_\varphi \tag{167c}$$

Then the momentum distribution density $A(\vec{k})$ from Eq. (164) can be expressed as

$$A(k, k_\vartheta, k_\varphi) = \left(\tfrac{2\Delta_z^2}{\pi}\right)^{\frac{3}{4}} \exp\left[-\Delta_z^2 \left(k^2 - 2k_0 k \cos k_\vartheta + k_0^2\right)\right] \tag{168}$$

where the aim is to replace the magnitude k of the wavevector by a function of the angular frequency ω using the dispersion relation

---

$$2m\omega = \hbar k^2 \tag{169}$$
$$2m\, d\omega = 2\hbar k\, dk = 2\sqrt{2m\hbar\omega}\, dk \tag{170}$$
$$dk = \frac{1}{2}\sqrt{\frac{2m}{\hbar\omega}}\, d\omega \tag{171}$$

---

and one arrives at

$$A(\omega, k_\vartheta, k_\varphi) = \left(\tfrac{2\Delta_z^2}{\pi}\right)^{\frac{3}{4}} \exp\left[-\tfrac{\Delta_z^2}{\hbar^2}\left(2m\hbar\omega - 2\hbar k_0\sqrt{2m\hbar\omega}\, \cos k_\vartheta + \hbar^2 k_0^2\right)\right] \tag{172}$$

At the same time, the infinitesimal volume element $d^3\vec{k}$ in spherical coordinates is

$$d^3\vec{k} = dk_x\, dk_y\, dk_z \tag{173}$$
$$= \det\left(\frac{\partial(k_x, k_y, k_z)}{\partial(k, k_\vartheta, k_\varphi)}\right) dk\, dk_\vartheta\, dk_\varphi \tag{174}$$
$$= k^2 \sin k_\vartheta\ \ dk\, dk_\vartheta\, dk_\varphi \tag{175}$$
$$= \tfrac{2m}{\hbar}\omega\ \tfrac{1}{2}\sqrt{\tfrac{2m}{\hbar\omega}} d\omega\ \ \sin k_\vartheta\, dk_\vartheta\, dk_\varphi\,. \tag{176}$$

Hence, the energy distribution arising from the normailsation condition becomes

$$1 \overset{!}{=} \int_{\omega=0}^{\infty} d\omega \left|D(\omega)\right|^2 = \iiint_{\mathbb{R}^3} d^3\vec{k} \left|A(\vec{k})\right|^2 \tag{177}$$

$$= \int_{\omega=0}^{\infty} d\omega \int_{k_\vartheta=0}^{\pi} dk_\vartheta \int_{k_\varphi=0}^{2\pi} dk_\varphi \left(\tfrac{2\Delta_z^2}{\pi}\right)^{\frac{3}{2}} \exp\left[-\tfrac{2\Delta_z^2}{\hbar^2}\left(2m\hbar\omega - 2\hbar k_0\sqrt{2m\hbar\omega}\, \cos k_\vartheta + \hbar^2 k_0^2\right)\right] \left(\tfrac{2m}{\hbar}\right)^{\frac{3}{2}} \tfrac{\sqrt{\omega}}{2} \sin k_\vartheta \tag{178}$$

$$= \pi\left(\tfrac{4m\Delta_z^2}{\pi\hbar}\right)^{\frac{3}{2}} \int_{\omega=0}^{\infty} d\omega\ \sqrt{\omega} \exp\left[-\tfrac{2\Delta_z^2}{\hbar^2}\left(2m\hbar\omega + \hbar^2 k_0^2\right)\right] \int_{k_\vartheta=0}^{\pi} \sin k_\vartheta\ dk_\vartheta \exp\left[\tfrac{4\hbar k_0 \Delta_z^2}{\hbar^2}\sqrt{2m\hbar\omega}\, \cos k_\vartheta\right]. \tag{179}$$

It remains to integrate over the polar component k_ϑ of the wavevector. Where a substitution by $\cos k_\vartheta =: t$ appears suitable for that aim which implies $d(\cos k_\vartheta) = -\sin k_\vartheta \; dk_\vartheta = dt$.

$$\begin{aligned}\int_{k_\vartheta=0}^{\pi} \sin k_\vartheta \; dk_\vartheta \exp\left[\frac{4\hbar k_0 \Delta_z^2}{\hbar^2}\sqrt{2m\hbar\omega}\,\cos k_\vartheta\right] &= -\int_{t=1}^{-1} dt \exp\left[\frac{4\hbar k_0 \Delta_z^2}{\hbar^2}\sqrt{2m\hbar\omega}\,t\right] \\ &= \left[\left(\frac{4\hbar k_0 \Delta_z^2}{\hbar^2}\sqrt{2m\hbar\omega}\right)^{-1} \exp\left[\frac{4\hbar k_0 \Delta_z^2}{\hbar^2}\sqrt{2m\hbar\omega}\,t\right]\right]_{t=-1}^{1} \\ &= \frac{\exp\left[4\Delta_z^2\sqrt{2m\hbar\omega}\frac{k_0}{\hbar}\right] - \exp\left[-4\Delta_z^2\sqrt{2m\hbar\omega}\frac{k_0}{\hbar}\right]}{4\Delta_z^2\sqrt{2m\hbar\omega}\frac{k_0}{\hbar}} \\ &= \frac{\sinh\left(4\Delta_z^2\sqrt{2m\hbar\omega}\frac{k_0}{\hbar}\right)}{2\Delta_z^2\sqrt{2m\hbar\omega}\frac{k_0}{\hbar}} \end{aligned} \tag{180}$$

And an expression for the absolute squared energy distribution is found as

$$\boxed{|D(\omega)|^2 = 2\left(\frac{4m\Delta_z^2}{\hbar}\right)^{\frac{3}{2}}\sqrt{\frac{\omega}{\pi}}\exp\left(-2\Delta_z^2\left(2m\omega/\hbar + k_0^2\right)\right)\frac{\sinh\left(4\Delta_z^2\, k_0\sqrt{2m\omega/\hbar}\right)}{4\Delta_z^2\, k_0\sqrt{2m\omega/\hbar}}} \tag{181}$$

If $k_0 = 0$, Eq. (180) reduces to $\int \sin k_\vartheta \; dk_\vartheta = 2$ and

$$\left|D(\omega)\right|^2\Big|_{k_0=0} = 2\left(\tfrac{4m\Delta_z^2}{\hbar}\right)^{\frac{3}{2}}\sqrt{\frac{\omega}{\pi}}\exp\left[-\tfrac{4m\Delta_z^2}{\hbar}\omega\right]. \tag{182}$$

This corresponds to a Maxwell-Boltzmann energy distribution of temperature $T = \hbar^2/(4mk_B\Delta_z^2)$ in three dimensions, while Eq. (146) reduces to the Maxwell-Boltzmann energy distribution for a single degree of freedom. They are thus consistent.

The time evolution of the three-dimensional wavepacket follows directly from the solution of the one-dimensional one. The coordinates are separable according to Eqs. (162) and the solution of Eq. (158) holds for each individual component. This means the wavefunction will spread equally in time into all directions, while its centre will move with group velocity $\frac{\hbar k_0}{m}$ along the z direction:

$$f(z,\rho,\varphi,t) = \frac{\exp\left[-\frac{\rho^2+(z-Z(t))^2}{4\Delta_z\alpha(t)} + i\left(k_0(z-Z(t)) + \frac{\hbar k_0^2}{2m}t\right)\right]}{(2\pi)^{\frac{3}{4}}\alpha^3(t)}\,, \tag{183a}$$

$$\text{with complex standard deviation } \alpha(t) = \Delta_z + \frac{i\hbar t}{2m\Delta_z}\,, \tag{183b}$$

$$\text{centre position } Z(t) = z_0 + \frac{\hbar k_0}{2m}t\,, \tag{183c}$$

$$\text{and absolute value squared } f^* f = \frac{\exp\left[-\frac{\rho^2+(z-Z(t))^2}{2\,|\alpha(t)|^2}\right]}{\left(2\pi\,|\alpha(t)|^2\right)^{\frac{3}{2}}}\,. \tag{183d}$$

5 A Model of Ions in Ultracold Atoms

While all ingredients where layed out to understand and analyse the established quasi-one-dimensional model of interatomic coulombic electron capture in nanowire-embedded quantum dots, the generalisation to cover ICEC by a trapped cation in a Bose-Einstein condensate of neutral atoms needs slightly more consideration. Particularly the numerous many-body interactions and subsystems involved in heavy metals typically trapped to the millions within a typical diameter of about 20 μm,[22] need some further approximation in order to arrive at a computable system of only a few degrees of freedom. A typical density for ultracold clouds of atoms is $\varrho_m = 10^{13} cm^{-3} = 10 \mu m^{-3}$.

Under the assumption of a Gaussian density distribution $\varrho_x(x)$ of atoms in spherical symmetry, the distribution can be expressed as

$$\varrho(r) = \varrho_m \exp\left[-\frac{1}{2}\left(\frac{r}{\Delta}\right)^2\right] \tag{184}$$

where ϱ_m is the maximal atom density and *Delta* is the standard deviation of the distribution. In the interval up to Δ, 68% of the total distribution are contained whereas 95% of atoms are contained within 2Δ. Therefore the spatial standard deviation can be estimated as 5 μm such that the typical diameter covers about

$$20\ \mu\text{m} \mathrel{\hat{=}} 4\Delta\ \ (95\%)\,. \tag{185}$$

Let the electron capturing cation to be at the centre of the spherical atomic distribution. Then, the average atom number $N(r)$ can be determined in the ball of radius r and the average atom number $n(r)$ in the infinitesimal shell between radius r and $r+dr$. For that purpose, the infinitesimal change in atom number shall be identified in dependence on the volume element $d^3\vec{r} = dr\ d\vartheta\ d\varphi\ \ r^2 \sin\vartheta$ by

$$dN(r) = d^3\vec{r}\ \varrho(r) = dr\ d\vartheta\ d\varphi\ \ \varrho(r)\ r^2 \sin\vartheta \tag{186}$$

which directly implies an average radial atom density

$$n(r) = \iint\limits_{(\vartheta,\varphi)=(0,0)}^{(\pi,2\pi)} \frac{dN}{dr} = 4\pi r^2 \varrho_m e^{-\frac{1}{2}\left(\frac{r}{\Delta}\right)^2}\,. \tag{187}$$

As result, the average cumulative atom number in a ball of radius r will be given by

$$N(r) = \int\limits_{r'=0}^{r} dr\ n(r') \text{ which is} \tag{188}$$

$$N(r) = 4\pi\Delta^3 \varrho_m \left(\sqrt{\tfrac{\pi}{2}}\,\mathrm{erf}\!\left(\tfrac{r}{\sqrt{2\Delta^2}}\right) - \tfrac{r}{\Delta} e^{-\frac{1}{2}\left(\frac{r}{\Delta}\right)^2}\right)\,. \tag{189}$$

Similarly, one can estimate the average radial distance $\bar{R}(r)$ from the central ion to the surrounding atoms in a ball of radius r with

$$\bar{R}(r) = \frac{\int\limits_{r'=0}^{r} dr'\ r' n(r')}{\int\limits_{r'=0}^{r} dr'\ n(r')} = \sqrt{2\Delta^2}\,\frac{1 - \left(1 + \frac{1}{2}\left(\frac{r}{\Delta}\right)^2\right) e^{-\frac{1}{2}\left(\frac{r}{\Delta}\right)^2}}{\frac{\sqrt{\pi}}{2}\,\mathrm{erf}\!\left(\frac{r}{\sqrt{2\Delta^2}}\right) - \frac{r}{\sqrt{2\Delta^2}}\, e^{-\frac{1}{2}\left(\frac{r}{\Delta}\right)^2}}\,. \tag{190}$$

The maximum radial atom density is given by the extremum condition of $dn/dr = 0$. Since this implies

$$0 = 4\pi\varrho_m r\left(2 - \tfrac{r^2}{\Delta^2}\right) e^{-\frac{r^2}{2\Delta^2}} \,, \tag{191}$$

the maximal atom density is $n|_{\max} = 8\pi\Delta^2\varrho_m \exp[-1]$ and is situated at a radius of $r|_{n=\max} = \sqrt{2\Delta^2} \approx 9.25\,\Delta^2\varrho_m$ which is about 2.31 nm^{-1}. The absolute atom number of the entire distribution is

$$N(\infty) = \lim_{r\to\infty} N(r) = 4\pi\Delta^3\sqrt{\tfrac{\pi}{2}}\varrho_m \tag{192}$$

with average distance to the electron capturing ion of

$$\bar{R}(\infty) = \lim_{r\to\infty} \bar{R}(r) = \sqrt{\tfrac{8}{\pi}}\,\Delta \,. \tag{193}$$

One can then identify the typical atom density $\bar{\varrho} = 3\sqrt{\frac{\pi}{2}}\varrho_m$ such that the overall atom number $N_\infty = \frac{4\pi}{3}\Delta^3\bar{\varrho}$. Last but not least, one can estimate typical volume radii and average distances of exactly 1,2 or 3 reaction partners. The volume containing exactly one neighbouring atom is given by the radius $r|_{N=1} \approx 289\,\mathrm{nm}$ with average distance of $\bar{R}(r|_{N=1}) \approx 217\,\mathrm{nm}$. A volume containing exactly two neighbouring atoms will have to radius of $r|_{N=2} \approx 363\,\mathrm{nm}$ with an average radial distance of $\bar{R}(r|_{N=2}) \approx 272\,\mathrm{nm}$ to the central ion.

5.1 A long-range Interaction

The Coulomb potential governing the interaction between two charged particles of respective charges q_1 and q_2 at positions $\vec{r}_1$ and $\vec{r}_2$ in space

$$V_C(r) = -\frac{q_1 q_2}{4\pi\varepsilon}|\vec{r}_1 - \vec{r}_2|^{-1} \tag{194}$$

was already introduced in the form of a central potential for the hydrogen problem. It can be expanded into a Taylor series known as multipole expansion. In the considered setup, a free electron approaches a cation while at some distance, a neutral atom can interact with the electron and the cation. The Coulomb attraction which the incident electron feels from the direction of the neighbouring atom is counteracted over large distances by the repulsion from the atom's electrons. The neutral atom and its electron does not have a net charge to interact with the incident electron on the cation. Let the atom be an alkali metal, then it offers a single electron in the outermost valence shell. In an effective treatment, the remaining inner electrons may be approximated to be frozen in place to form an effective binding potential together with the attraction by the nucleus. The effective binding potential for the remaining outer-valence electron may then be expressed as[111]

$$\frac{4\pi\epsilon}{e^2}\,V(r) = -\frac{Z}{r} + \frac{\alpha_D}{2r^4}\left(1 - \exp\left[-\left(\tfrac{r}{\delta_D}\right)^2\right]\right)^2 + \sum_\ell B_\ell \exp\left[-\left(\tfrac{r}{b_\ell}\right)^2\right] \tag{195}$$

which is a sum of a Coulomb attraction term stemming from the remaining effective net charge Ze, an effective polarisation potential with dipole polarisability α_D and additional potential terms to correct for relativistic effects in dependence on the

angular momentum ℓ. This approach relies thereby on Gaussian functions with respective radial extension δ_D and b_ℓ to model the net effect of the multi-electronic nature of the atom by a pseudopotential of frozen a inner valence and core charge distribution. Applying this to both the neighbouring atom as well as the electron capturing cation, it is possible to reduce the number of involved bodies significantly.

In this effective frozen-core treatment, the incident electron on the capturing ion and the outer-valence electron bound to the assisting atom form two electric dipoles. Let the atom be a rubidium atom due to its prominence in ultracold atom experiments.[22–24] Let the capturing species be a barium (II) cation for the moment which admits to neglect an additional outer valence electron present in the barium (I) cation which is usually used for trap experiments.[22] Then one can express the position of the incident electron with respect to the barium (II) ion as $\vec{x}_{Ba^+}$ and the position of the treated rubidium electron with respect to the rubidium core as $\vec{x}_{Rb}$. As a particular result of the multipole expansion of the Coulomb potential, the interaction energy between two electric dipoles $q_i\,\vec{x}_i$ is given by[108]

$$\mathscr{R}^3 V_{12} = \frac{q_1 q_2}{4\pi\epsilon}\left(\vec{x}_1\cdot\vec{x}_2 - 3\left(\vec{x}_1\cdot\frac{\vec{\mathscr{R}}}{\mathscr{R}}\right)\left(\frac{\vec{\mathscr{R}}}{\mathscr{R}}\cdot\vec{x}_2\right)\right). \tag{196}$$

where $\mathscr{R}$ is the distance between the dipoles. For large distances between the two nuclei in comparison with their distance to the respective electron, the dipole distance is approximating to the distance between the nuclei. This allows to treat the two electrons in local coordinates with respect to their nucleus of reference. A graphical representation of the system coordinates thus introduced is given by Figure 4.

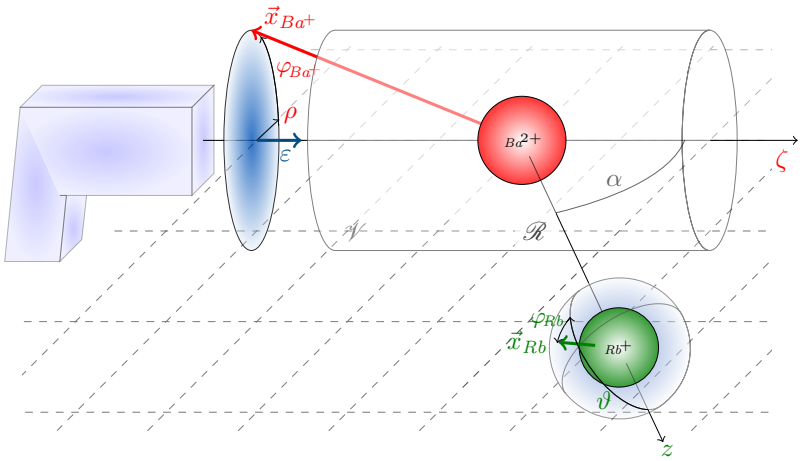

Figure 4: The coordinate system of an electron beam incident on a barium (II) cation with a rubidium atom at distance $\mathscr{R}$ and angle α between incident electron beam and interatomic axis.

It arises from the initial conditions of a longitudinally approaching electron wavepacket that the incident electron on the barium (II) cation might be expressed advantageously in local cylindrical coordinates whereas the outer-valence electron

on rubidium shows the spherical polar probability density of the $5s$ orbital. This results in the normalised spherical polar kinetic energy operator

$$\hat{T}_{Rb} = -\tfrac{\hbar^2}{2m}\left(\partial_r{}^2 + r^{-2}\hat{\ell}^2_{(\theta,\varphi_{Rb})}\right) \tag{197}$$

for the rubidium electron which was already given in equation (122). The incident electron in the barium reference frame, on the other hand, is to be expressed in terms of cylindrical coordinates of position ζ along the cylinder axis, transverse distance ρ from the axis and azimuthal angle φ_{Ba^+} with respect to the plane spanned by the cylinder axis and the atom-atom axis. The normalised kinetic energy operator for the incident electron in the cylindrical local coordinates is then

$$\hat{T}_{Ba^+} = -\tfrac{\hbar^2}{2m}\left(\partial_\zeta{}^2 + \partial_\rho{}^2 + \rho^{-2}(\partial_{\varphi_{Ba^+}}{}^2 + \tfrac{1}{4})\right) \tag{198}$$

whereas the binding potential is not separable

$$\frac{4\pi\epsilon}{e^2}\, V_{Ba^+} = -\frac{2}{\zeta^2+\rho^2} + \frac{\alpha_D}{2(\zeta^2+\rho^2)^2}\left(1-\exp\left[-\tfrac{\zeta^2+\rho^2}{\delta_D^2}\right]\right)^2 + \sum_\ell B_\ell \exp\left[-\tfrac{\zeta^2+\rho^2}{b_\ell}\right]. \tag{199}$$

At this point, all ingredients have been introduced to model the dynamics of interatomic coulombic electron capture by a trapped cation in an ultracold cloud of neutral atoms. It is noteworthy, however, that the model has so far not taken much heed of the spatial distribution of the assisting atom cloud nor of the large number of reaction partners available. Simultaneously, the average distance to the first atom is typically orders of magnitude larger than the atomic scale dipole-dipole interaction which is inverse proportional to the cube of the distance between the electron-capturing ion and the assisting atom. It shall thus be proposed to introduce the multi-atomic distribution of reaction partners into an effective interaction description in order to counteract the available distances between ion and atom in the order of $10^5\ a_B$ by the available number of reaction partners in the order of 10^6 atoms.

Toward this goal, the experimentally-induced potential preparing and holding the macroscopic atomic distribution shall be given by a harmonic potential acting on a rubidium atom. The simple Hamiltonian

$$\hat{h}_{\mathscr{R}} = -\frac{\hbar}{2M_{Rb}}\partial^2_{\mathscr{R}} + \frac{\hbar}{4M_{Rb}\Delta^2_{\mathscr{R}}}\mathscr{R}^2 \tag{200}$$

shall be introduced where M_{Rb} is the mass of a rubidium atom, $\Delta_{\mathscr{R}}$ is the standard deviation of the spatial distribution of the atom cloud determined by the experimental conditions and $\mathscr{R}$ has become an additional degree of freedom, describing the distance of the rubidium atom with respect to the central barium (II) cation. This gives rise to the normalised probability density of the ground state function for the effective rubidium position as

$$\left|\psi^{(0)}_{\mathscr{R}}\right|^2 = (2\pi\Delta^2_{\mathscr{R}})^{-1/2}\ \exp\left[-\frac{\mathscr{R}^2}{2\Delta^2_{\mathscr{R}}}\right] \tag{201}$$

which correlates to the assumed spatial density distribution from (184) up to the normalisation factor.

The spatial atom density is then scaled as

$$\varrho(\mathscr{R}) := N_{Rb} \left|\psi_{\mathscr{R}}^{(0)}\right|^2 \tag{202}$$

where N_{Rb} is the total amount of trapped rubidium atoms. Similarly, taking the many-partner interaction into account, the barium (II) cation feels at a given distance $\mathscr{R}$ and angle α to the incident electron axis the effective potential

$$V_{\text{eff}} = N_{Rb} \left|\psi_{\mathscr{R}}^{(0)}\right|^2 V_{12}\,. \tag{203}$$

By integrating over the polar angle α between incident electron axis and atom-atom axis under the assumption of a constant distribution of rubidium atoms, one thus arrives at the effective potential

$$\frac{4\pi\epsilon}{e^2}\frac{\mathscr{R}^3}{N_{Rb}}V_{\text{eff}} = \rho\cos\varphi_{Ba^+}\, r\sin\vartheta\cos\varphi_{Rb} - 4\rho\sin\varphi_{Ba^+}\, r\cos\vartheta - 2\zeta\, r\sin\vartheta\sin\varphi_{Rb} \tag{204}$$

where it is apparent that the number of atoms N_{Rb} can successfully compensate the large distances between electron capturing ion and the assisting electron on a neutral atom at distance $\mathscr{R}$ in this effective description. Consequently, an effective model of seven spatial degrees of freedom has been derived here in order to study the electron dynamics of interatomic coulombic electron capture at near experimental conditions for ions in ultracold assisting clouds of atoms. Apparent from the onset, the range of the dipole-dipole interaction proposed to admit the introduction of two local subsystems would be numerically restricted to closer ranges than the expected 200 nm typical for the distance between the central ion and the next atom. The introduction of the large number of available atoms in the surrounding, however, enabled to stabilise this in an effective treatment accounting for a net interaction with the distributed large number of assisting atoms.

Within this chapter, a model was thereby derived for the description of interatomic coulombic electron capture by a barium (II) cation assisted by a surrounding ultracold cloud of neutral rubidium atoms which had been motivated and inspired by available experimenting techniques. On the one hand, a theoretical simulation of electron dynamics is quickly challenging computational resources such that numerical implementations need to employ simplifications by appropriate approximations and exploitation of available symmetries. The fewer interacting bodies involved in a particular system, the easier it is to handle and to simulate. On the other hand, investigations by experiment approach the same process always from a macroscopic perspective of feasibility. While aiming to study the smallest possible entities, they have to realise the experiment in a macroscopic sometimes large-scale apparatus. Realising a setup with fewer interacting bodies increases the necessary efforts which is perhaps one of the reasons why ICEC has not yet been reported by experiments. Nevertheless, both systems discussed theoretically within this dissertation, nanowire-embedded quantum dots and ultracold atoms, may eventually find experimental application to which the provided insight gathered from the performed numerical simulations can assist.

Part III
Applications

The previous part has introduced the necessary mathematical concepts to model and analyse the electron dynamics involved in an interatomic coulombic electron capture. An essential ingredient in the established model of nanowire-embedded quantum confinements and in its generalisation to Bose-Einstein-condensate embedded ultracold ions are Gaussian functions. They come into play as many-body averaged potentials and as spatial probability distributions for various degrees of freedom contributing to the overall wavefunction. As such, they have been used to approximate the multi-atomic nature of solid-state quantum confinements such that the effective longitudinal potential in the quantum dots is modelled by Gaussian wells whereas a harmonic lateral confinement from the nanowire itself induces a transversally Gaussian probability density in the ground state. Owing to this transverse restriction, a modified effective Coulomb potential allows a description of electronic motion along a single spatial dimension, the axis of the nanowire.[8]

On the same footing, the multi-electronic nature of atoms and ions was approximated by effective Gaussian potential wells to account for the closed electronic shells of core and inner-valence electrons which partially shield and modify the attraction toward the multiply charged nucleus experienced by an additional external or outer-valence electron.[111] In either case, the effective potential in the form of a Gaussian well allowed to reduce the number of treated degrees of freedom. The generalisation to ultracold atoms followed thereby naturally and smoothly from the established dynamic model and its concepts for quantum dots. Moreover, the macroscopic confinement of a multi-atomic Bose-Einstein condensate was introduced as spherically harmonic nuclear potential which induces an effective radial probability density of surrounding atoms able to assist in an interatomic coulombic electron capture by the central ion. The approximation by an effective radial distribution allows to stabilise the model against the numerical difficulty arising from the difference in orders of magnitude between electronic interaction potentials of a few bohr radii and an average distance between capturing ion and assisting atom at orders above 100 nm in a typical experiment.[22]

Introducing the incident electron by an initial Gaussian wavepacket of one or more dimensions, the dynamical and kinematic implications were discussed such that this part will present numerical applications in two steps to test the portability of the model. First, the application to quantum confinements in nanowires is going to revisit different aspects of electronic dynamics in a methodological and consistent manner. Then, the generalized model is applied to compute the electron dynamics of interatomic coulombic electron capture by a barium (II) cation assisted by an ultracold cloud of neutral rubidium atoms which will test efficacy and impediments of the adapted model and its numerical implementation with respect to ICEC. To help the reader by providing a self-consistent discussion within the respective chapter, central equations and parameters necessary for the computational implementation shall be briefly paraphrased where spoken of although mainly subject of Part II and

covered therein. The used parameters employed in the individual application are summarized for clarity in Table 1 and Table 2.

6 Artificial Atoms in Nanoelectronics

The numerical investigations of interatomic coulombic electron capture have been successfully tackling the question of electronic dynamics already very shortly after the first prediction of the process in general and were able to simultaneously expand the scope of interatomic coulombic electron capture by its introduction into solid-state systems. Nevertheless, these studies shed spotlights onto particular setups of the model and were to some extent not yet able to enlighten a broader conceptual understanding. This difficulty was not least arising from the amount of parameters available to be chosen freely although electronic motion was described to occur along a single axis. Mostly predetermined by the partaking species for ICEC in atoms, a solid-state system can in fact be adapted freely and quasi-continuously in size, and within intervals, it can be varied in its material composition or doping. The quantum dot binding potential alone provides thus more control parameters than actual electronic degrees of freedom.

Although Gaussian potential wells had already been used beforehand to describe quantum dots,[112] employing the MCTDH approach for an efficient electron-dynamical treatment of quantum dot pairs was proposed in (2011) in order to study interatomic coulombic decay, which proved adaptable to cover a larger spatial domain in order to present the first electron scattering with interatomic coulombic electron capture by (2013).[3] Describing the same physical systems by the same methodological approach, the numerical studies of both processes were able to synergise their efforts and research questions such that the investigation in (2013) was already indicating that met conditions for an interatomic coulombic decay could enable an increase in efficiency for the interatomic coulombic electron capture.[3] As they had initially been implemented for electronic triplet configurations, the singlet analogon was soon presented for ICD which proved equivalent in its electron dynamics for singlet as for triplet configuration and additionally made use of the effective quasi-one-dimensional approximation of the Coulomb interaction.[74] Eventually, this reduction in degrees of freedom admitted to reduce computational resources for studies of ICEC which in turn afforded an increase in the longitudinal numerical grid.[8]

Although piecewise ventures into the unknown had succeeded, it was yet unclear from these attained glimpses how these pieces would fit into a bigger picture. Particularly the question of well-suited descriptors for what determined ICEC dynamics alluded the investigators where the quasi-one-dimensional model appears overdetermined by its amount of parameters in contrast to the time-resolved Schrödinger equation which provides only two independent spatial degrees of freedom. There must be a smaller set of quantities that act as parameters and determine key features of the electron dynamics. To alleviate the gaps between the individual studies, recent investigations attacked the system parameters and the resulting dynamical quantities of ICEC methodically over a broader domain.[2,64]

Building upon its predecessors, this work revisits key quantities of ICEC dynamics in quantum dot pairs in a systematic approach and adds previously unconsidered aspects. In particular, it will advance in four logical steps: At first, it will revisit a singular setup which stood out during a recent investigation,[2] to which it will add the consideration of directionality in electron dynamics of ICEC. It will therefore investigate and compare the ICEC-associated spectrum of electron flux density in both available directions, those of reflection and transmission. Moreover, this shall be compared with a computation of non-interactive electron dynamics to determine the proportions of directional dependence arising from the quantum dot potential itself and those proportions which emerge from the interatomic coulombic electron capture. In a next step, the capturing confinement size will be varied at constant parameters for material and centre-to-centre distance. This study will add insight into the directionality of ICEC in its key entities where it is going to validate whether the transmission direction is in fact dominating over the previously unpublished ICEC associated flux density into reflection direction. Furthermore, an upper limit in ICEC flux density as function of energy will be found in the form of an envelope function which will also relate to the variation in capture size and shall reflect the evolution of the flux density into both emission directions which is necessary to potentially understand how to optimise a hypothetical ICEC applying device. Then a simultaneous variation of material composition with capture size revisiting a related recent study,[64] shall generalize the findings induced from the investigation of the quantum size effect. It will be suggested that while both parameters modify the single-electron eigenenergies of the quantum-dot potential, the actual eigenenergies describe and modify the electron dynamics if ICEC qualitatively simpler than the parameters themselves.

While previously successful in ascribing limiting kinematic conditions restricting the parameter domain of ICEC,[64] the observation that trends in ICEC probability appear to follow trends in single-electronic eigenenergies has not been yet expressed but will provide a practical guideline for future studies. It will thus eventually be tested here for several quantum-dot distances over which it will be presented to remain valid for each distance individually, but will be modified in the range of covered eigenenergies from one inter-quantum-dot distance to the next. Incidentally, two energy levels appear to dominate the trends in ICEC probability while two subprocesses will have been consistently found in the individual flux density spectra. It will thus suggest the final hypothesis for the system that prospective investigations might describe ICEC dynamics better if resolved by these two energy levels. Using these as descriptive parameters appears at currently available resolution to simplify the behaviour of interatomic coulombic electron capture. This description would also be portable to other systems, other potentials, and eventually also to experimental investigations.

6.1 Computational Details

In line with the preceding studies, the multi-configurational time-dependent Hartree (MCTDH) approach was applied here to compute the interatomic coulombic electron capture dynamics by propagating the quantum-mechanical two-electron wavefunc-

tion composed by[90,91]

$$\Psi(z_1, z_2, t) := \sum_{j_1, j_2 = 1}^{N_1, N_2} A_{j_1 j_2}(t) \chi_{j_1}(z_1, t) \chi_{j_2}(z_2, t) \tag{205}$$

which constitutes superposed Hartree products of time-dependent functions $\chi_j(z,t)$ of position z along the axis of motion. These lower-dimensional but flexible functions known as single-particle functions (SPFs)

$$\chi_j(z,t) := \sum_{m=1}^{M} c_j^{(m)}(t) b_m(z). \tag{206}$$

are themselves formed from a set of functions $\{b_m(z)\}_{m=1}^{M}$, the primitive basis which is given for this application by a discrete variable representation of 431 grid points in sine (Chebyshev) form. Each electronic z coordinate is thereby governed from $z = -270.0\ a_B$ to $+270.0\ a_B$. Initiated on a configuration space $N_1 \times N_2$ of 14×14 single-particle functions, enforcing the identical nature of both electrons in spatial antisymmetrisation of triplet states by persistently antisymmetric coefficients

$$A_{j_2 j_1}(t) := -A_{j_1 j_2}(t)\ \forall t. \tag{207}$$

allows to reduce the configuration space and computational resources. See Table 1 for a concise summary of the employed numerical parameters.

The initial wavefunction is prepared by a one-dimensional Gaussian wavepacket in the form

$$\phi_0(z) = \left(2\pi\Delta_z^2\right)^{-\frac{1}{4}} \exp\left[-\left(\frac{z - z_0}{2\Delta_z}\right)^2 + \frac{i}{\hbar} p_0 \left(z - z_0\right)\right] \tag{208}$$

introduced in Section 4.1, Eq. (130) representing the free electron which is approaching the quantum-dot potential from the *left* in antisymmetric superposition with the single-electron eigenfunction of the quantum-dot binding potential localized on the right and represented by state $\left|R_0\right\rangle$. The binding potential itself is modelled by an asymmetric pair of Gaussian wells in the established form of[2,72,113]

$$V_{2G}(z) = -D_L \exp\left[-2\left(\frac{\mathscr{R}}{\mathscr{L}_L}\right)^2 \left(\frac{z}{\mathscr{R}} + \frac{1}{2}\right)^2\right] - D_R \exp\left[-2\left(\frac{\mathscr{R}}{\mathscr{L}_R}\right)^2 \left(\frac{z}{\mathscr{R}} - \frac{1}{2}\right)^2\right] \tag{209}$$

which was analogously introduced in Section 3.4, Eq. (92). The energetic parameters $D_{L/R}$ represent the energy threshold from the minimum of the respective left or right potential well to continuum. The length scale $\mathscr{L}_{L/R}$ represents a characteristic diametric confinement size amounting to twice the root-mean-square (rms) width $\Delta_{L/R}$ of the respective Gaussian well.

The incident electronic wavepacket is initially centred along the z-axis at $z_0 = -125\ a_B$ and moves with group momentum $p_0 = 355 \times 10^{-3}\ E_H$ and is spread along the axis with an rms width of $\Delta_z = 10.0\ a_B$. At first separated by a large distance, the electron interaction is negligible and the wavefunction is well-described by a

single configuration. With the evolution in time, the electrons approach each other and their increasing interaction will induce a wider population over the configuration space. One of the advantages of this model is here the material-independent description by effective atomic units which can be scaled according to the effective electron mass of the particular nanowire material as described in Section 3.5.1.

The radial width of the nanowire is introduced into the model by interpretation as a transversal binding of both electrons by a general harmonic potential of characteristic length l (cf. Section 3.2.1, (52)) which is set to $l = 1.0\ a_B$ for the presented investigations. Under the assumption of a transversally occupied ground state, this implies an effective interaction potential between the electrons according to[8,74,114]

$$V_{12}(z_1, z_2) = \sqrt{2} E_H \tfrac{a_B}{l}\ H_{-1}\Big(\tfrac{|z_1 - z_2|}{\sqrt{2} l}\Big) \tag{210}$$

as introduced with Section 3.2.1 where $H_{-1}(x)$ is the -1$^{\text{st}}$ Hermite polynomial of an independent variable x according to Eq. (46).

To enforce a constant initial wavefunction for the sake of consistent comparability throughout the steps of this study, the right quantum dot remains unchanged in its parameters D_R and $\mathscr{L}_R$ which dominantly determines the properties of the quantum-dot eigenstate $\big|R_0\big\rangle$ localized on the right. It remains set at a continuum threshold of $D_R = 0.60\ E_H$ and a longitudinal length of $\mathscr{L}_R = 1.41\ a_B$. This chosen in agreement with previous investigations.[8,9] The remaining quantum-dot system parameter are addressed step-wise over this chapter.

Computational results will first be presented for a constant distance of $\mathscr{R} = 10.0 a_B$ between the two quantum-confinement centres and a constant left continuum threshold of $D_L = 0.71$. As instructing configuration ICEC dynamics will first be analysed in detail for a capture length of $\mathscr{L}_L = 2.83\ a_B$ before investigating the variation in quantum-dot eigenenergies and in the spectrum of ICEC-associated electron flux density and probability density within a range of confinement lengths from $\mathscr{L}_L = 1.83\ a_B$ to $4.71\ a_B$. This view is then expanded to a concerted variation in the two independent parameters $\mathscr{L}_L$ and D_L. In addition to the variation of confinement length over the same interval, the continuum threshold is also varied within a range from $D_L = 0.40\ E_H$ up to $1.10\ E_H$. Eventually, an additional variation of the distance $\mathscr{R}$ between the two confinement centres is added where the same domain of $(\mathscr{L}_L, D_L)$ is analysed over seven different distances from $\mathscr{R} = 6.0\ a_B$ up to $\mathscr{R} = 12.0\ a_B$.

Reflections of the eletron wavefunction occuring at the edges of the numerical grid would not represent an open system with entering and leaving electron probability density meaningfully and would even interfere with the remaining portions of the wavefunction. To prevent this non-physical behaviour, complex absorbing potentials $\hat{W}$ with

$$-i\hat{W} := -i\eta\ \left(\frac{|z - z_{cap}|}{a_B}\right)^n \times \Theta\left[-k\left(\frac{z - z_{cap}}{a_B}\right)\right] \tag{211}$$

Table 1: Collection of computational parameters of the system.

Incident electron parameters, see Eqs. (52) and (130)				
$p_0 = 0.335\,\hbar/a_B$	$z_0 = -125\,a_B$	$\Delta_z = 10.0\,a_B$	$l = 1.0\,a_B$	
Quantum-dot-pair parameters, see Eq. (92)				
$\mathscr{L}_L \in \{1.83\ a_B,\ \ldots,\ 4.71\ a_B\}$	$\mathscr{L}_R = 0.707\ a_B$			
$D_L \in \{0.40\,E_H,\ \ldots,\ 1.10\,E_H\}$	$D_R = 0.60\ E_H$			
$\mathscr{R} \in \{6.0\ a_B,\ \ldots,\ 12.0\ a_B\}$				
DVR type	grid points		z range	
Sine	431		$-270.0\,a_B$	$+270.0\,a_B$
SPF configurations			14×14, *id*	
CAP	n	k	z_{cap}	η
	2	± 1	$\pm 168.75\,a_B$	$5.79 \cdot 10^{-6}\,E_H$

of quadratic order, $n = 2$, have been employed where $\Theta(z)$ represents the Heaviside function which is positioned at $z_{cap} = \pm 168.75\,a_B$ in order to collect the outgoing fractions of the wavefunction.[115–118] The absorption strength η has been computed to absorb maximally and respectively reflect as little as possible from the grid's edges. See Table 1 for details.

6.2 Results

6.2.1 Electrodynamic Impulse and Interatomic Coulombic Decay

The two-electron probability densities related to the eigenfunctions of the numerical model system as depicted in Figure 5 offer a ground state and three bands of excited states before energy $E = 0$. In the background of the figure, the quantum confinement potential is indicated in black dotted lines, showing a centre-to-centre distance of $\mathscr{R} = 10\ a_B$ with the origin of the coordinate system centred equally between them. The left quantum dot in this figure has a potential depth of $D_L = 0.71\ E_H$ while the right reference dot has a potential depth of $D_R = 0.6\ E_H$. These are the potential depth parameters of highest probability in the six configurations reported in[8]. The right quantum well has a characteristic length of $\Delta_R = 1/\sqrt{2}\ a_B$ and the left quantum well a characteristic length of $\Delta_L = \sqrt{2}\ a_B$. The ground state of the two electrons is characterised by electron probability maxima in both potential wells speaking for both electrons being bound simultaneously to lowest states of the left and right quantum dot, L_0 and R_0 respectively. Its eigenenergy is $E_{L_0R_0} = -604.57 \times 10^{-3}\ E_H$.

The first band of excited states is formed by an electron bound to the lowest bound state offered by the double well, L_0 in this case, and an electron in the free continuum. It starts at $E_{L_0} = -454.67 \times 10^{-3}\ E_H$. The close energetic spacing between free electron states in their numerical representation forms the band of two-electron wavefunctions. The width of the band is determined by the included amount of continuum states within the computational model and would analytically be a continuous spectrum all the way from the first excited two-electron wavefunction through $E = 0$ which characterises both electrons to be free, to higher energies. The second band of excited two-electron states is consequently a combination of an

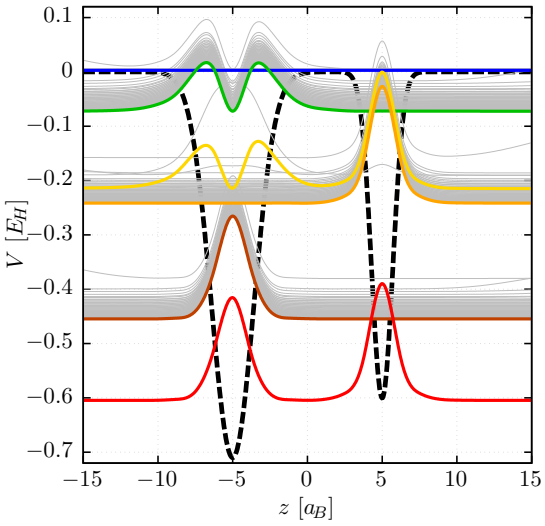

Figure 5: Two-electron probability densities $|\Psi_n(z)|^2$ of the wavefunctions in Gaussian binding potentials of a pair of quantum confinements in a nanowire. The binding potential is indicated in black dashed line, the grey solid lines indicate the first 150 eigenstates in the numerical representation of the system. The coloured eigenfunctions from the lowest energy up show the system's ground state with two captured electrons in red, the first band of excitations with one electron bound in the ground state of the left potential in dark orange, the second band of excited states with one electron bound in the right potential's ground state in orange, and a third band of excited states with an electron bound to the left confinement in an excited state in green, close to the two-electron continuum in blue. Within the second band of excited states, a state with two bound electrons one in the ground state of the right and one in the excited state of the left is indicated in yellow.

electron bound to state R_0 indicated by electron probability localised in the right potential well, and the other electron unbound. It begins at $E_{R_0} = -241.42 \times 10^{-3}\ E_H$. The energetic order of single-bound states is generally not fixed but a consequence of the combination of the five parameters $(D_L, \Delta_L, \mathscr{R}, D_R, \Delta_R)$ of the asymmetric quantum double well. Incidentally, the combination of two bound-electrons in the left-excited state L_1 and in the right R_0 lies energetically within the second band of excited states at $E_{L_1R_0} = -214.79 \times 10^{-3}\ E_H$. This makes a transition from the double-bound L_1R_0 to a single bound state of similar energy likely which would indicate decay by ionisation. The third band of excited states is already positioned energetically close to the double-ionisation threshold of $E = 0$ and indicates an electron bound in the left excited state L_1 recognisable by the two maxima in probability density located within the left quantum well and by a free electron. Its lower bound eigenenergy is $E_{L_1} = -72.34 \times 10^{-3}\ E_H$. The first fully unbound eigenenergy for two free electrons is numerically positioned at $E = +2.92 \times 10^{-3}\ E_H$ due to electron-electron repulsion on a finite grid of points in space.

Sending a free electron wavepacket onto a right bound electron in R_0 will thus be the initial condition of a numerical investigation of interatomic coulombic electron capture in a such system. This electron probability density in space and time and the electron flux density in time related to this study is graphically depicted in Figure 6. The left panel shows the full electron dynamics in the ICEC simulation, the centre panel shows the difference with respect to a simulation without electron interaction which is presented as reference in the right panel. Each bottom panel depicts the electron probability density $|\Psi(t,z)|^2$ to find an electron at time t in position z. Initially at $t = 0$, an electron is bound to the quantum-dot eigenstate R_0 with high electron probability indicated by yellow colouring at $z = 5\ a_B$. Another electron is initially normal-distributed with standard deviation of $\Delta = 10\ a_B$ resulting in an orange colouring of approximately 40 a_B diameter on the negative z-axis centred at $z = -125\ a_B$. The wavepacket has an initial momentum depicted by positive slope $\Delta z/\Delta t$ of $p_0 = 0.335\ \hbar a_B/E_H$. The simulation in Figure 6 (c) shows that without electron-electron interaction, a part of the free electron wavepacket is moving with constant momentum through the quantum dot potential which is apparent from the persistent slope $\Delta z/\Delta t$ in the graph. An equal part is reflected at the quantum dot potential and travelling back with equal but opposite momentum. The forward travelling wavefronts interfere with the already reflected wavefronts and form interference ridges particularly visible at negative z around $t = 400\ \hbar/E_H$. Moreover, the wavepacket broadens with time.

Since the reflected part of the wavepacket interferes with itself and gets distorted through the quantum confining potential, it broadens significantly more on negative z where its tail leaves the quantum dot system approximately 200 $\hbar/E_H$ after the transmitted portion and it shows a very low velocity which results in it having barely separated from the bound electron at $t = 1\,400\ \hbar/E_H$. Throughout the entire experiment, the bound electron in R_0 is visible by a bright electron probability density at $z = 5\ a_B$ and remains unperturbed by the motion of the free wavepacket. From about 1 000 $\hbar/E_H$ onwards, the probability density diminishes gradually which is a numerical phenomenon due to the wavepacket leaving the observation volume and being absorbed by the complex absorbing potential at the boundaries thus reducing the norm of the two-electron wavefunction within the volume which numerically affects the probability density of the bound electron but leaves it qualitatively intact.

The upper graphs in Figure 6 show the electron flux measured at $z_F^{\pm} = \pm 200\ a_B$ that correlates with an electron bound to the quantum confinement levels L_0, R_0 and L_1. This relates directly to the colour-coded electron probability density at z_F in the lower graphs of $|\Psi(t,z)|^2$. Therefore, the different contributions of electron flux density $F(t)$ for the reference case in Figure 6 (c) set on after $t = 500\hbar/E_H$. The largest flux contributions correspond to transmitted and reflected electron flux in correlation with an occupied quantum-dot state R_0 respectively denoted by $F_{R_0}^{\pm}$. These two contributions are 17 orders of magnitude bigger than electron flux density corresponding to an occupied energy level $L_{0/1}$ in the left quantum dot which can thus be considered numerical noise and appear to be in fact an echo at the computational accuracy limit of the flux density in channels $F_{R_0}^{\pm}$. The maximal flux density transmitted through the double well is measured with $\max F_{R_0}^{+} = 8.23 \times 10^{-4}\ E_H/\hbar$ at $t = 901\ \hbar/E_H$. The flux density maximum reflected by the potential is measured

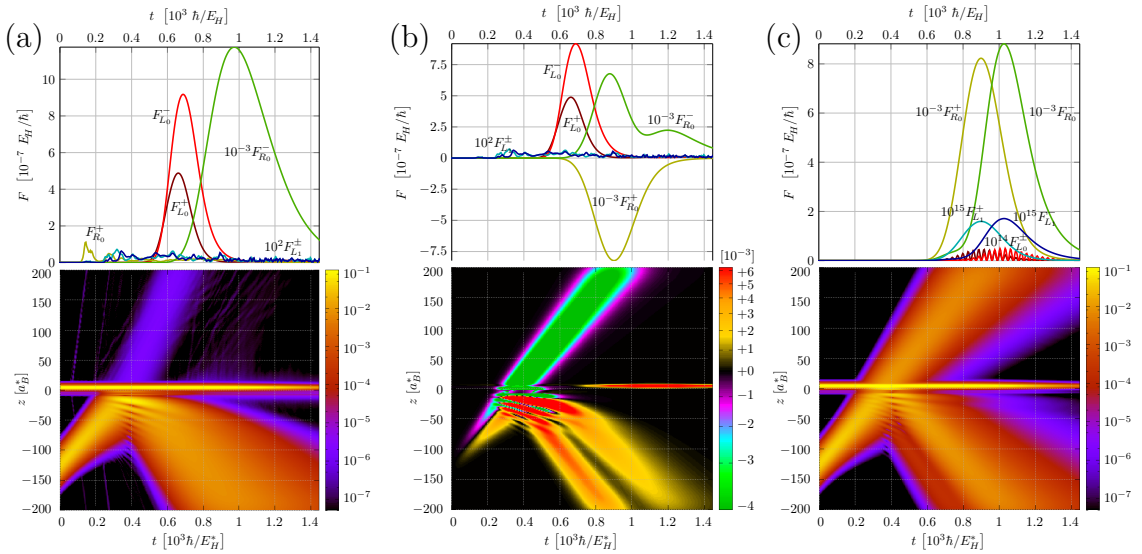

Figure 6: Dynamics of interatomic coulombic electron capture in a pair of quantum confinements within a nanowire. Lower panels: the evolution of electron probability density $|\Psi(t,z)|^2$ in position z and time t. Upper panels: the quantum flux density $F^{\pm}(t)$ measured at $z_F^{\pm} = \pm 200 a_B$ as function of time t and in correlation to an occupied state L_0, R_0 or L_1. (a) Full electron dynamics governed by electron-electron interaction with a large portion of reflected electron wavepacket and some transmitted flux correlating to electron capture into state L_0. (b) The difference to a non-interactive simulation. (c) The reference simulation of electrons at same initial conditions without electron interaction transmits and reflects comparable amounts of incident electron.

to be $\max F_{R_0}^{-} = 8.82 \times 10^{-4}\ E_H/\hbar$ at $t = 1\,025\ \hbar/E_H$. The full width at half maximum (FWHM) of $F_{R_0}^{+}(t)$ is 258 $\hbar/E_H$, the full width at half maximum of $F_{R_0}^{-}(t)$ is 269 $E_H/\hbar$ but both distributions are asymmetrical with an extended tail towards larger times and the full widths at tenth maximum (FWTM) read 478 $\hbar/E_H$ and 549 $\hbar/E_H$, respectively.

The full electron dynamics including electron-electron interaction is graphically presented analogously in Figure 6 (a). This is the actual interatomic coulombic electron capture simulation and shows considerable differences to the reference computation in Figure 6 (c). The initial conditions remain unchanged. An electron is bound in the state R_0 narrowly distributed around $z = 5\ a_B$ and a broader free electron wavepacket is moving towards it from $z = -125\ a_B$ and reaches the interaction region around $t = 200\ \hbar/E_H$. On impact, electron density is leaving the quantum confinement region with slightly higher momentum than the incoming wave packet indicated by an increase in slope $\Delta z/\Delta t$. At the same time, electron probability density becomes pronounced in the left quantum confinement around $z = -5\ a_B$ which shows two density maxima by two orange coloured ridges suggesting a partial occupation of eigenstate L_1. At approximately $t = 600\ \hbar/E_H$, major portions of the electron probability density separate again. The tail of the reflected part of the incoming wave packet leaves the quantum confinement region and gradually gains

momentum. The consistent stream of outgoing electron density towards positive z stops. Some weaker contributions appear to leave the confinement region in short spurts throughout the remaining time towards both sides. The electron probability density within the confinement region diminishes gradually from 1 000 $\hbar/E_H$ onwards.

In the upper panel of Figure 6 (a), the contributions of electron flux density at $z_F^{\pm} = \pm 200\ a_B$ are depicted as functions of time t in correlation with respective occupation of the states L_0, R_0 or L_1 within the confinement region. Electron flux measured at z_F^- is dominated by correlation with occupation of R_0 which is consistent with the interpretation of the electron probability density graph and suggests a strong reflectivity of the incoming wave packet due to the electron-electron repulsion. The maximum of reflected density is measured at $t = 971\ \hbar/E_H$ with $F_{R_0}^- = 11.75 \times 10^{-4}\ E_H/\hbar$ and a full width at half maximum of 391 $\hbar/E_H$ with trailing flux density at larger times. Nevertheless, a significant portion is observed to correlate with an occupied L_0 state in the left quantum confinement. This is masked in the probability density plot due to the convolution with the reflected incident wavepacket but shows a clear maximum in electron flux density of $F_{L_0}^- = 9.18 \times 10^{-7}\ E_H/\hbar$ at $t = 686\hbar/E_H$ with full width at half maximum of 177 $\hbar/E_H$. It is further showing two revivals with a temporary maximum flux density of $F_{L_0}^- = 8.26 \times 10^{-9}\ E_H/\hbar$ at $t = 1306\ \hbar/E_H$ and outside the depicted time frame at $t = 1632\ \hbar/E_H$ with a temporary maximum flux density of $F_{L_0}^- = 6.59 \times 10^{-9}\ E_H/\hbar$.

Electron flux density correlating with an occupied excited state L_1 does not contribute significantly and is only measured as numerical noise at peak flux density of $F_{L_1}^{\pm} \leq 7.20 \times 10^{-10}\ E_H/\hbar$ on either side. In the direction of transmission, the difference between the full electron dynamics in Figure 6 (a) and that without inter-electronic interaction in Figure 6 (c) is most apparent. Where a large portion of incoming wave packet was transmitted through the quantum confinement region in correlation with initially occupied state R_0, the electronic interaction obstructs nearly any electron transmission in correlation with R_0. The transmitted flux density has thus a maximum of $F_{R_0}^+ = 1.11 \times 10^{-7}\ E_H/\hbar$ at time $t = 144\ \hbar/E_H$ and shows a pronounced revival with peak at 272 $\hbar/E_H$ and flux density of $F_{R_0}^+ = 4.92 \times 10^{-8}\ E_H/\hbar$. Identifying these density flows in the lower panel points to jets of comparably high velocity emitted symmetrically to transmission and reflection direction from the occupied state R_0 itself. Those first two emissions correspond temporally with the instant of activation of the complex absorbing potential and with the impact of the incident wavefront on the right quantum confinement at $z = 0\ a_B$. Particular search for jets of equal slope $\Delta z/\Delta t \approx 2.9 a_B E_H/\hbar$ shows another emission at $t \approx 728\hbar/E_H$ which corresponds approximately with the instant when the tail of the reflected electron wavepacket is leaving the quantum confinement region. From there on, a gradually diminishing background of electron flux density in the order of $10^{-8}\ E_H/\hbar$ is measured with correlation to an occupied state R_0. Instead of electron flux in correlation with the initial state R_0, the dominant contribution in transmission direction is thus correlated to the energetically lower state L_0. This indicates a portion of a successful interatomic coulombic electron capture. The difference in energy between the bound states R_0 and L_0 adds to the kinetic energy of the incident electron such that the transmitted ICEC flux is indicated by a slightly increased slope $\Delta z/\Delta t$ with comparison to the incident wavepacket in the lower panel of Figure 6

(a). The maximum electron flux density is reached at $t = 661\ \hbar/E_H$ and amounts to $F^+_{L_0} = 4.88 \times 10^{-7}\ E_H/\hbar$ with a full width at half maximum of 156 $\hbar/E_H$. Similarly to the reflected flux in correlation with L_0, the transmitted ICEC flux undergoes two revivals, the first of which climaxes at $t = 1\,211\ \hbar/E_H$ at $F^+_{L_0} = 1.24 \times 10^{-8}\ E_H/\hbar$, while the second revival peaks at a flux density of only $F^+_{L_0} = 4.95 \times 10^{-9}$ at time $t = 1\,546\hbar/E_H$ outside the depicted time interval.

To expose the effect of electron interaction on the dynamics, Figure 6 (b) illustrates the difference between the computed full dynamics in a) and the reference simulation without interaction in c) for both the electron probability density in space and time (lower panel) and the correlated flux density at $z^{\pm}_F = \pm 200\ a_B$ (upper panel). The electron probability density is dominated by the contributions arising from the increased reflectivity and reduced transmittivity in the order of 10^{-3} to $10^{-2}\ a_B^{-1}$. Already at $t = 54\hbar/E_H$, the repulsive force between both electrons has delayed the incident wavepacket enough to display a lack of $\Delta_I|\Psi|^2 = -1.07 \times 10^{-4}\ a_B^{-1}$ at $z = -95\ a_B$ which has fallen behind by 21 a_B. This is recognisable in the lower panel of Figure 6 (b) by the early onset of magenta coloured density difference above $z = -100\ a_B$ indicating a deficiency of probability density in the full dynamics with respect to the reference computation in Figure 6 (c), and by the simultaneous onset of yellow coloured density difference below $z = -100\ a_B$ indicating a surplus of probability density. Similarly for the electron probability distribution initially bound to R_0 in the right quantum dot, $\Delta_I|\Psi|^2 = 0.38 \times 10^{-4}\ a_B^{-1}$ of electron probability density have been displaced a grid point off-centre towards the outside of the confinement region. Due to the difference in deviation magnitude of the probability density of the wavepacket and that within the confinement region, Figure 6 (b) can only depict changes in probability density above $10^{-4}\ a_B^{-1}$ and fails to graphically resolve the fractions arising from occupations of L_0. As time proceeds, the deviation in probability density evolves and enters orders of $10^{-2}\ a_B^{-1}$ by $t = 295\ \hbar/E_H$. In a compromise, colour resolution of deviations of that order and above has been neglected and falls within the representation in dark-green colour for density deficiencies of absolute magnitude above $-4\ a_B^{-1}$ or within the representation in red colour for density surplus above $6\ a_B^{-1}$. The interference behaviour in the fully interactive computation deviates particularly strongly from the reference simulation due to the large portion of reflected incident electron probability distribution. Setting on at $t = 200\ \hbar/E_H$, this governs the graph until $t = 600\ \hbar/E_H$ when the tail of the reflected wavepacket leaves the confinement region. At that instant in time, the left quantum-dot holds a surplus of $\Delta_I|\Psi|^2 = +0.48 \times 10^{-4}\ a_B^{-1}$ at its centre at $z = -5\ a_B$ with two local maxima on the neighbouring grid points on either side, measuring $+1.08 \times 10^{-4}\ a_B^{-1}$ at $z = -6.25\ a_B$ and $+1.28 \times 10^{-4}\ a_B^{-1}$ at $z = -3.75\ a_B$. This suggests a partial occupation of L_1. The right confinement shows a deficiency in electron probability density of $\Delta_I|\Psi|^2 = -1.02\ a_B^{-1}$ at its centre $z = +5.00\ a_B$ at time $t = 600\ \hbar/E_H$ and a surplus of $\Delta_I|\Psi|^2 = +1.20\ a_B^{-1}$ outward at $z = +6.25\ a_B$. At larger times, the deviation in electron probability density is dominated by 4 features: the deficiency of transmitted incident electron at constant momentum for positive z, a surplus of reflected incident electron of equal, constant momentum for negative z, a second stream of surplus reflected incident electron starting at lower velocity but gradually accelerated by electronic repulsion and a surplus of electron probability density in R_0 from $t \approx 700\ \hbar/E_H$ onwards as the electron interaction

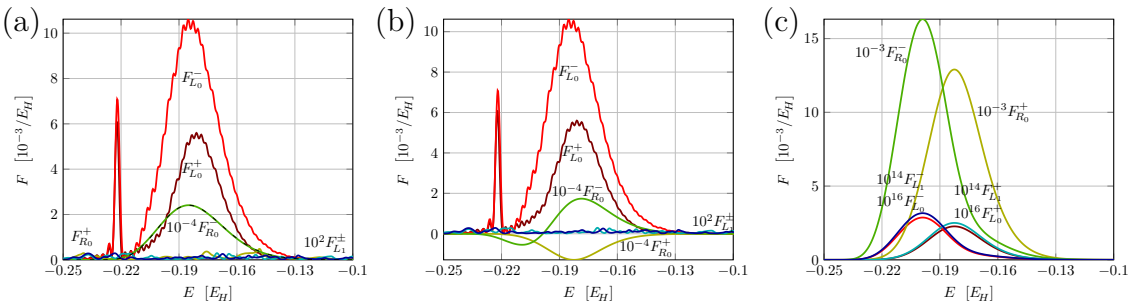

Figure 7: Electron flux density in correlation with occupied state L_0, R_0 or L_1 as function of incident energy. (a) Full dynamics with electron-electron interaction. (b) Difference in flux density with respect to non-interactive dynamics. (c) Reference flux density of electron dynamics without electron interaction.

prolongs longevity of the wavefunction norm within the numerical grid.

The difference in time-dependence of the flux density at $z_F = \pm 200\ a_B$ between the full electron dynamics and the reference simulation is drawn in the upper panel of Figure 6 (b) which allows to overcome some of the graphical difficulties the electron probability density posed. It shows that the deviation in flux density correlated to initially occupied state R_0 is in fact by a factor thousand larger than the flux density deviation correlated to occupied state L_0. The maximal deficiency in transmission direction reaches $\Delta_I F^+_{R_0} = -8.23 \times 10^{-4}\ E_H/\hbar$ at $t = 901\ \hbar/E_H$ with full width at half maximum of 258 $\hbar/E_H$ which is mainly reflected by electron repulsion climaxing at a surplus of $\Delta_I F^-_{R_0} = 6.77 \times 10^{-4}\ E_H/\hbar$ already at $t = 876\ \hbar/E_H$ and showing a full width at half maximum of 214 $\hbar/E_H$. Remaining above 13.5 % of its maximal value, at a temporal minimum with surplus flux density of $\Delta_I F^-_{R_0} = 0.92 \times 10^{-4}\ E_H/\hbar$ at $t = 1\,104\ \hbar/E_H$, it peaks again at $t = 1\,195\ \hbar/E_H$ in a surplus of flux density $\Delta_I F^-_{R_0} = 1.10 \times 10^{-4}\ E_H/\hbar$ before dying down below $10^{-9}\ E_H/\hbar$ outside the depicted time interval at $t = 2\,319\ \hbar/E_H$. The graph of the deviation in flux density further alludes that the flux densities correlating to an occupation of L_0 are a pure phenomenon of the electron interaction, as is the hundred times weaker temporally diffuse contribution in correlation with an occupied excited state L_1. They show thus the same characteristics as in Figure 6 (a).

The Fourier transform of the measured quantum flux density $F(t)$ with respect to time resolves the individual contributions to the flux density as functions of total energy E. This is illustrated in Figure 7 for the reference simulation in subfigure (c), for the full interactive case in subfigure (a) and highlighting the difference between both cases in subfigure (b).

In consequence of the time-dependent representation, the flux density as function of system energy in case of the reference simulation is dominated by the contributions correlated to the occupation of the initial bound state R_0. Figure 7 (c) shows further that transmission and reflection through the quantum-dot potential are energy selective. Higher energy contributions are transmitted through the potential while portions of lower energy are mainly being reflected. The energy difference between the flux density maxima is $16.5 \times 10^{-3}\ E_H$. The maximal flux density transmitted is thus $F^+_{R_0} = 12.90\ E_H^{-1}$ at a system energy of $E = -182.5 \times 10^{-3}\ E_H$ with a full

width at half maximum of $32.6 \times 10^{-3}\ E_H$. The maximal reflected flux density shows $F^-_{R_0} = 16.32\ E_H^{-1}$ at $E = -199.0 \times 10^{-3}\ E_H$ with full width at half maximum of $29.8 \times 10^{-3}\ E_H$. Contributions correlated to any occupied state on the left quantum dot are sixteen orders of magnitude smaller and show same maximum position and FWHM as the R_0 contributions supporting the hypothesis of echoing the main contributions at the numerical accuracy limit. The transmitted flux densities climax at $F^+_{L_0} = 2.27 \times 10^{-19}\ E_H^{-1}$ for the left ground state and at $F^+_{L_1} = 2.50 \times 10^{-17}\ E_H^{-1}$ for the left excited state. The reflected contributions peak for the left ground state at $F^-_{L_0} = 2.87 \times 10^{-19}\ E_H^{-1}$ and for the left excited state at $F^-_{L_1} = 3.16 \times 10^{-17}\ E_H^{-1}$.

The three main contributions in flux density for the case of full electron interaction as depicted in Figure 7 (a) have their maxima at other energies than for in the non-interactive case. The reflected wavepacket in correlation with R_0 occupation shows its maximum of $F^-_{R_0} = 24.10\ E_H^{-1}$ at system energy $E = -185.0 \times 10^{-3}\ E_H$ which is $14.0 \times 10^{-3}\ E_H$ higher than in the non-interactive case. It has a full width at half maximum of $39.0 \times 10^{-3}\ E_H$. The ICEC relevant L_0-correlated flux density shows two local maxima for the reflected and the transmitted flux density each. The maximal contribution of reflected wavepacket $F^-_{L_0} = 10.62 \times 10^{-3}\ E_H^{-1}$ in correlation with an occupied ground state L_0 is positioned at approximately equal energy $E = -185.2 \times 10^{-3}\ E_H$ as the reflected contribution correlated to R_0. Its full width at half maximum is $31.1 \times 10^{-3}\ E_H$. It has a pronounced narrow second peak of flux density $F^-_{L_0} = 7.08 \times 10^{-3}\ E_H^{-1}$ at $E = -222.0 \times 10^{-3}\ E_H$, however, which shows a full width at half maximum of only $2.7 \times 10^{-3}\ E_H$. The transmitted flux density $F^+_{L_0}$ correlated with left ground state L_0 exhibits also two peaks of similar characteristic, one narrow and on broad, but its broader contribution at FWHM of $26.6 \times 10^{-3}\ E_H$ reaches with $F^+_{L_0} = 5.60 \times 10^{-3}\ E_H^{-1}$ at $E = -181.0 \times 10^{-3}\ E_H$ only about half of its reflected equivalent and the narrow peak at FWHM of $2.5 \times 10^{-3}\ E_H$ dominates with $F^+_{L_0} = 6.08 \times 10^{-3}\ E_H^{-1}$ at $E = -222.3 \times 10^{-3}\ E_H$. The remaining contributions to the overall flux density show a diffuse spectrum at least one order of magnitude lower and appear to not exhibit any recognisable trends.

Investigating the deviation in flux density spectra between the fully interactive dynamics and the reference case without electron interaction as it is depicted in Figure 7 (b), one observes analogously to the representation of flux density deviation as function of time in Figure 6 (b) that contributions correlated to L_0 or L_1 are pure phenomena of interelectronic energy exchange. Moreover, the reaction channels related to the initially occupied state R_0 are being modulated. While the transmission channel $F^+_{R_0}$ is primarily characterised by a nearly complete deficiency in flux density with maximum of $\Delta_I F^+_{R_0} = -12.90\ E_H^{-1}$ at $E = -182.5 \times 10^{-3}\ E_H$ and full width at half maximum of $32.6 \times 10^{-3}\ E_H$, the reflection channel $F^-_{R_0}$ lacks flux density at lower energies with maximal $\Delta_I F^-_{R_0} = 5.45\ E_H^{-1}$ at $E = -209.2 \times 10^{-3}\ E_H$ and full width at half maximum of $18.2 \times 10^{-3}\ E_H$ but portrays a surplus at higher energy of maximal $\Delta_I F^-_{R_0} = 17.36\ E_H^{-1}$ at $E = -178.5 \times 10^{-3}\ E_H$ and FWHM of $30.3 \times 10^{-3}\ E_H$.

For the computation without electron interaction, the ratio of overall transmitted flux density by incident flux density can be used to evaluate the transmittivity `T` of

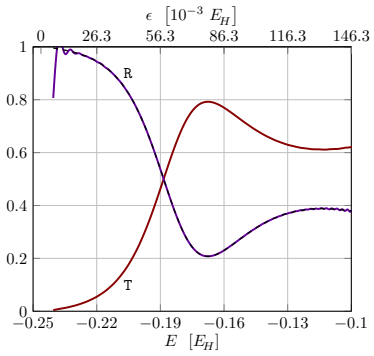

Figure 8: Transmittivity T and reflectivity R of the binding potential as function of system energy E and free electron energy ϵ. The dashed line represents $1 - \mathtt{T}$ which is analytically equal to R. Deviations are due to numerical division by small numbers at the edges of the energy distribution of the system.

the quantum-dot binding potential as function of energy. Similarly, the ratio of reflected flux density and incident flux density can be used to evaluate the reflectivity R of the binding potential in this setup. These are presented in Figure 8. Analytically, transmission and reflection must make up all available probability density current such that transmittivity and reflectivity add up to unity when electron capture is not available as is the case in the simulation where electron interaction does not take place. At the edges of the distribution where the incident flux density is close to zero, the transmittivity is numerically more stable than the reflectivity which oscillates for energies below $-0.23\ E_H$ and for energies above $-0.12\ E_H$. As this has to be a purely numerical phenomenon, the direct reflectivity R represented by a violet line is overlain by a dashed black line indicating the alternative definition as $\mathtt{R} = 1 - \mathtt{T}$.

As the system energy reduces to eigenenergy $E_{R_0} = -246.31 \times 10^{-3}\ E_H$, the reflectivity of the confinement potential approaches unity and the transmittivity vanishes. Since the reference simulation ignores electron interaction, the two electrons and their energies are independent of each other in that case. The reflectivity and transmittivity are then analogously functions of free electron energy $\epsilon = E - E_{R_0}$. At system energy $E = -240.5 \times 10^{-3}\ E_H$, the reflection coefficient of the binding potential is still dominating largely with $\mathtt{R} = 99.56$ % leaving a transmission coefficient of only $\mathtt{T} = 0.04$ %. This difference reduces with increasing energy until transmittivity and reflectivity are equally reaching 50 % at $E = -188.5 \times 10^{-3}\ E_H$. This is the energy where equivalent transmitted and reflected flux density contributions F_i^+ and F_i^- of Figure 7 (c) match in magnitude. From there on, the transmission coefficient dominates of the reflectivity and reaches a maximum of $\mathtt{T} = 79.22$ % at $E = -167.5 \times 10^{-3}\ E_H$ where the reflectivity reaches its minimum at remaining $\mathtt{R} = 20.78$ %. Their difference diminishes again slightly with increasing energy until $E = -112.0 \times 10^{-3}\ E_H$ where the transmission coefficient remains dominant as it settles at $\mathtt{T} = 61.14$ % leaving the reflection coefficient at $\mathtt{R} = 38.86$ %. The transmittivity slightly increases again with energy within the remaining window and reaches $\mathtt{T} = 62.07$ % at $E = -100.0 \times 10^{-3}\ E_H$ where the reflectivity ends on $\mathtt{R} = 37.93$ %.

Previous studies of this system have concentrated on the transmitted quantum flux density in correlation with capturing state L_0.[3,8,9] This seemed reasonable because the electron probability density of the fully interactive electron dynamics masked any reflected contributions correlating to an electron capture within the dominant broad stream of reflected incident wavepacket at occupied initial state R_0. Due to the immense mass of the quantum-dot system with respect to the moving electrons, a conservation of electron momentum is not valid, however, and the densities of electron probability and the quantum flux show already in the reference computation without electron interaction that reflected and transmitted contributions can be of comparable magnitude. Equivalent flux densities corresponding to the same occupied state were split in energy such that the transmission maximum in the reference dynamics was $16.5 \times 10^{-3}\ E_H$ higher in energy than the reflection maximum. In the ICEC dynamics computation, a local transmission maximum correlating to capture state L_0 lay only $4.2 \times 10^{-3}\ E_H$ above the reflection maximum which coincided energetically with the R_0-correlated reflection maximum in the full dynamics. That the transmitted flux density presents two local maxima was recently observed.[2] The distinctly different nature of both maxima was attributed to two distinct subprocesses of interatomic coulombic electron capture: a direct energy transfer between the electrons on impact which reflects the energetically broad spectrum of the incident wavepacket, and an intermediary capture into L_1R_0 with consecutive interatomic coulombic decay which shows a comparably narrow spectrum around a resonance energy. The previously not-investigated reflected quantum flux density $F^-_{L_0}$ exhibits a qualitatively similar behaviour but while the decay-related maximum is only 16.49 % larger than its transmitted equivalent, the reflected impact maximum exceeds the transmitted one by 89.64 %. On the one hand, the maximal reflected flux density due to the confining potential itself is already 26.46 % higher than the transmitted one. On the other hand, transmittivity and reflectivity of the binding potential are functions of the free energy ϵ of an electron. They thus shift with respect to the system energy E depending on the correlated occupied state L_0, R_0 or L_1. Nevertheless, free energies below $\epsilon = 57.8 \times 10^{-3}\ E_H$ are preferably reflected while higher energies are mainly transmitted by the confinement potential. An additional obstruction of transmission derives from the electron repulsion which also adds a further energetic dependence to transmission and reflection coefficients. Therefore it is primarily the transmitted reference contribution $F^+_{R_0}$ which, in comparison of the non-interactive dynamics with the full interaction, is converted into a surplus of reflected flux density $F^-_{R_0}$ related to a persistent initial state R_0 as well as flux density $F^+_{L_0}$ related to interatomic coulombic electron capture.

6.2.2 The Influence of the Quantum Size Effect

In connection with former studies,[3,8] the system under investigation showed three different behaviours resulting from varying the size of the capturing confinement. The distance between the confinement centres as well as the individual continuum threshold energies have been kept constant. It is known that varying the confinement size shifts the associated energy levels of eigenstates of the system. This phenomenon known as quantum size effect is a universal quantum-mechanical phenomenon independent of the underlying potential. The exact variation of each level, however, remains a function of the individual parameters to the potential. As two distinct

reaction pathways have suggested themselves in the flux spectrum above which may depend differently on the individual energy levels, their interaction and the ICEC flux density may be tuned or detuned by the size parameter of the quantum confinement. Building and elaborating on the published results of Molle et al. [2], this section presents the influence of the quantum size effect on the transmitted and reflected electron flux $F^{\pm}_{L_0}$ correlated to an occupied state L_0 within the quantum confinement region. This represents a succesful interatomic coulombic electron capture.

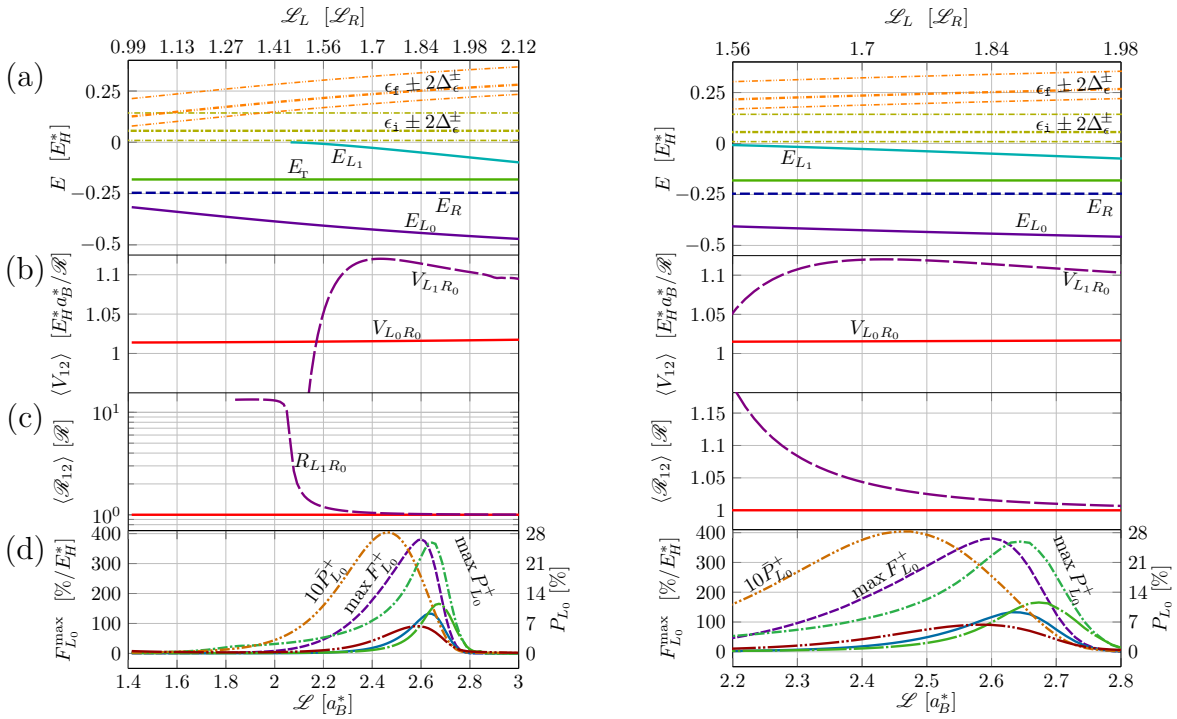

Figure 9: The impact of the quantum size effect on the interatomic coulombic electron capture in a pair of quantum confinements within a nanowire.

The quantum size effect with respect to characteristic diametric length $\mathscr{L}_L = 2\Delta_L$ in the model system has been investigated for a range between $\mathscr{L}_L = \frac{1}{2}\sqrt{2}\ a_B$ and $\mathscr{L}_L = 3.54\ a_B$ and shall be presented here in alignment with Figure 9 (a) for the refined range from $\mathscr{L}_L = \sqrt{2}\ a_B$ to $\mathscr{L}_L = 3\ a_B$ which represents a respective size of $1\mathscr{L}_R$ and $\frac{3}{2}\sqrt{2}\mathscr{L}_R$ relative to the confinement size $\mathscr{L}_R$ of the neighbouring quantum dot. Equivalently to expressing the length parameter $\mathscr{L}_L$ of the capturing confinement in the characteristic effective length scale of a_B, one may quantify it in terms of the respective parameter $\mathscr{L}_R = \sqrt{2}\ a_B$ of the neighbouring potential well. As the exact dependence of the system's energy levels and consequently the interatomic electron capture on the individual confinement sizes and their interrelation are not yet rigorously understood, both units are specified for the x axis in Figure 9. The right panel shows the same data as the left panel but for a narrower size range from $\mathscr{L}_L = 2.2\ a_B$ to $\mathscr{L}_L = 2.8\ a_B$ to aid the reader in visually distinguishing geometric configurations of higher significance to the process of interatomic coulombic electron capture.

During this investigation, the distance $\mathscr{R}$ between the quantum confinements, the potential parameters of standard deviation $\mathscr{L}_R$ and continuum threshold energy D_R of the right potential well, the continuum threshold energy D_L of the capturing potential well and the energy distribution of the incident electron at average kinetic energy ϵ_0 have been kept constant. This implies a constant eigenenergy of right-bound state R_0 which is indicated by a dashed blue line in Figure 9 (a) and a constant total energy E_T of the system indicated by a green solid line at $E = -181.2 \times 10^{-3}\ E_H$ and standard deviation in the order of $10^{-6}\ E_H$. The constant initial mean kinetic energy $\epsilon_\mathrm{i} = 56.1 \times 10^{-3}\ E_H$ is indicated by a yellow dashdotted line and the range in energy $\pm 2\Delta_\epsilon^\pm$ is indicated by slim yellow dashdotted lines above and below the mean energy. The distribution in kinetic energy is asymmetric with longer tail towards higher energies. This is due to the dispersion relation between the symmetrically distributed momentum with standard deviation $\Delta_p = \hbar/\Delta_z$ of inverse proportionality to the initial spatial extension Δ_z of the wavepacket and the kinetic energy $\epsilon = p^2/(2m)$. The characteristic energy range is thus $\Delta_\epsilon^- = 28.5 \times 10^{-3}\ E_H$ for smaller energies and $\Delta_\epsilon^+ = 38.5 \times 10^{-3}\ E_H$ for larger ones.

The change in length of the left quantum confinement induces a change in energies of left-bound eigenstates L_0 and L_1. The left-bound ground-state L_0 is presented by a violet solid line uniformly decreasing with confinement size $\mathscr{L}_L$ from $E_{L_0} = -316.5 \times 10^{-3}\ E_H$ at $\mathscr{L}_L = \sqrt{2}\ a_B$ to $E_{L_0} = -471.3 \times 10^{-3}\ E_H$ at length $\mathscr{L}_L = 3\ a_B$. The left-bound excited state L_1 is presented by a cyan solid line uniformly decreasing with increasing size $\mathscr{L}_L$ from $E_{L_1} = -0.573 \times 10^{-6}\ E_H$ at length $\mathscr{L}_L = 2.065\ a_B$ down to $E_{L_1} = -0.979 \times 10^{-3}\ E_H$ at length $\mathscr{L}_L = 3\ a_B$. At smaller confinement sizes $\mathscr{L}_L$, the excited eigenenergy E_{L_1} was numerically larger than zero and thus represented an unbound electron state of the continuum. It is thus not being shown for those cases in Figure 9. From the energy $E_{R_0} - E_{L_0}$ transferred between the electrons during a successful electron capture into L_0, the expected range of outbound kinetic energy for the released partner electron can be estimated *ab initio* by $\epsilon_\mathtt{f} = \epsilon_\mathtt{i} + E_{R_0} - E_{L_0}$ and is illustrated by an orange dash-double-dotted line where the energy range $\pm\Delta_\epsilon^\pm$ is indicated by slim lines of same style above and below. The estimated released kinetic energy $\epsilon_\mathtt{f}$ thus uniformly increases with confinement length $\mathscr{L}_L$. With an average value of $\bar{\epsilon}_\mathtt{f} = 212.1 \times 10^{-3}\ E_H$, it rises from $\epsilon_\mathtt{f} = 126.3 \times 10^{-3}\ E_H$ at length $\mathscr{L}_L = \sqrt{2}\ a_B$ to $\epsilon_\mathtt{f} = 281.1 \times 10^{-3}\ E_H$ at length $\mathscr{L}_L = 3\ a_B$.

In addition to the individual eigenenergy, varying the size of the quantum confinement also affects the extension of the wavefunctions associated to the bound states. Particularly, when both electrons temporarily occupy a bound state within the confinement region, the expectation values of their interaction potential as well as their distance $|z_2 - z_1|$ appear of relevance and are thus respectively illustrated in Figure 9 (b) and (c) as function of size $\mathscr{L}_L$ of the capturing confinement. As first-order approximation, the interaction between two electrons simultaneously occupying the two potential wells in the confinement region has been estimated as $\langle V_{L_k R_0} \rangle \approx E_H a_B/\mathscr{R}$ which is inversely proportional to the centre-to-centre distance $\mathscr{R}$ between the two wells.[3,8,64] The accuracy of this estimate, however, has been discussed in Molle et al. [2] and shall be paraphrased here for completeness and in the context of Figure 9 (b) and (c). The electronic interaction potential at simul-

taneous occupation of L_0 and R_0 increases uniformly with the confinement size of the capturing quantum dot from $V_{L_0R_0} = 101.39 \times 10^{-3}\ E_H$ at length $\mathscr{L}_L = \sqrt{2}\ a_B$ to $V_{L_0R0} = 101.75 \times 10^{-3}\ E_H$ at length $\mathscr{L}_L = 3\ a_B$. This corresponds to an underevaluation of the ground state through the $1/\mathscr{R}$-approximation by 1.37 % to 1.72 %. The simultaneous occupation of left-bound excited state L_1 and right-bound state R_0 shows a stronger variation with confinement size $\mathscr{L}_L$.

From the onset of state L_1 at length $\mathscr{L}_L = 2.065\ a_B$ to length $\mathscr{L}_L = 2.43\ a_B$, the interaction energy is rapidly increasing with confinement size $\mathscr{L}_L$ from $V_{L_1R_0} = 39.07 \times 10^{-3}\ E_H$ at onset to its climax at $V_{L_1R_0} = 112.03 \times 10^{-3}\ E_H$. For larger confinement sizes $\mathscr{L}_L$ within the investigated range, the interaction energy decreases uniformly to $V_{L_1R_0} = 109.47 \times 10^{-3}\ E_H$ at $\mathscr{L}_L = 3\ a_B$. Its average expectation value is $\bar{V}_{L_1R_0} = 107.74 \times 10^{-3}\ E_H$ with standard deviation of $9.04 \times 10^{-3}\ E_H$. Clearly, the interaction potential approximation by $\mathscr{R}^{-1}$ overestimates strongly for states with energies E_{L_1} close to zero. The interaction energy $V_{L_1R_0}$ passes the value of $E_H a_B/\mathscr{R}$ at length $\mathscr{L}_L = 2.162\ a_B$ with a comparably steep slope $\Delta V_{L_1R_0}/\Delta\mathscr{L}_L = 199.8 \times 10^{-3}\ E_H/a_B$.

The average expectation value of electron-electron distance $\bar{\mathscr{R}}_{L_0R_0}$ for a simultaneous occupation of left-bound ground state L_0 and right-bound R_0 within the presented range of confinement sizes is $0.446 \times 10^{-3}\ a_B$ smaller than the distance parameter $\mathscr{R} = 10.0\ a_B$. Over the size range, the electron-electron distance decreases slightly but uniformly with increasing length parameter $\mathscr{L}_L$ from $\mathscr{R}_{L_0R_0} = \mathscr{R}$ at length $\mathscr{L}_L = \sqrt{2}\ a_B$ to $\mathscr{R}_{L_0R_0} = 99.981\ \%\mathscr{R}$ at length $\mathscr{L}_L = 3\ a_B$. The expectation value for simultaneously occupied states L_1 and R_0 is uniformly decreasing from $\mathscr{R}_{L_1R_0} = 4.935\ \mathscr{R}$ at length $\mathscr{L}_L = 2.065\ a_B$ to $\mathscr{R}_{L_1R_0} = 100.323\%\mathscr{R}$ at length $\mathscr{L}_L = 3.0\ a_B$. For smaller lengths, the state L_0 does not represent a bound but rather a continuum state such that the expectation value of the electron-electron distance $\mathscr{R}_{L_1R_0}$ is numerically limited by the size of the grid which is illustrated by values of the order of 100 a_B in Figure 9 (c). The average expectation value is $\bar{\mathscr{R}}_{L_1R_0} = 11.685\ a_B$ which is 16.85 % larger than the centre-to-centre distance $\mathscr{R}$ of the quantum dot system.

With respect to the approximation of interaction energy $V_{L_kR_0}$ as $E_H a_B/\mathscr{R}$, the interaction energy is thus generally underestimated within the presented confinement size range for both $V_{L_0R_0}$ and $V_{L_1R_0}$. While the estimate of interaction energy in simultaneously occupied left- and right-bound ground states L_0 and R_0 appears satisfactory with an average underestimate between 1.37 % and 1.72 % only, its accuracy in estimation of $V_{L_1R_0}$ is strongly dependent on confinement size and varies between underestimating by up to 10.74 % to overestimating by 156.0 % within the numerical model. A reduction of confinement size pushes the state L_1 towards the continuum at zero. As it approaches the continuum, the eigenfunction extends over a larger domain which allows to reduce the electron-electron interaction. This implies that the expectation value of the electron-electron distance $\mathscr{R}_{L_1R_0}$ diverges as the energy E_{L_1} approaches the continuum and the approximation by $\mathscr{R}$ fails. Similarly to the interaction energy, the estimate of expected electron-electron distance $\mathscr{R}_{L_0R_0}$ for simultaneous occupation of the left- and the right-bound ground state proves satisfactory within the presented size range with a deviation below 2 ‰. The expectation

value $\mathscr{R}_{L_1R_0}$, however, is generally larger than $\mathscr{R}$ and remains strongly dependent on the size of the capturing quantum dot $\mathscr{L}_L$. An estimate of the electron-electron distance by the distance between the quantum dots $\mathscr{R}_{L_1R_0} \approx \mathscr{R}$ only underestimates less than 10 % for capturing lengths above $\mathscr{L}_L = 2.27\ a_B$. Moreover, the extension of the wavefunction increases the expectation value of interaction energy with respect to the reciprocal expectation value of electron-electron distance such that $\langle V_{12}\rangle > E_H a_B / \langle \mathscr{R}_{12}\rangle$. The ground state interaction $V_{L_0R_0}$ is thus in average 1.52 % larger than $E_H a_B/\mathscr{R}_{L_0R_0}$ with a standard deviation of 0.10 %. The excited state interaction $V_{L_1R_0}$ is in average 18.59 % above $E_H a_B/\mathscr{R}_{L_1R_0}$ and has a standard deviation of 13.29 %.

The significant quantities related to the electron flux density in correlation with an occupied state L_0 and thus representing a successful interatomic coulombic electron capture are illustrated in Figure 9 (d). Since reflected and transmitted contributions can be of comparable magnitude for appropriate conditions, the figure depicts reflected contributions by long dashes and respective transmitted contributions by short dashes. Therefore, the maximal reflected flux density ($\max_E F^-_{L_0}$) with respect to system energy E as function of capturing quantum dot size $\mathscr{L}_L$ is presented as a solid cyan line, the maximal transmitted flux density ($\max_E F^+_{L_0}$) is represented by a short-dashed blue line. The maximal capture probability ($\max_E P^-_{L_0}$) with respect to reflected Flux $F^-_{L_0}$ overall system energies E as function of length $\mathscr{L}_L$ is presented by a long-dash-dotted green line, its equivalent ($\max_E P^+_{L_0}$) with respect to transmitted flux is represented by a short-dash-dotted line. The overall capture probability into state L_0 is given by the integral ($\int_E dE\, F^\pm_{L_0}$) of respective flux density over the entire energy range as function of length parameter $\mathscr{L}_L$, such that the probability ($\int_E dE\, F^-_{L_0}$) of reflected quantum flux density in correlation to an occupied state L_0 is presented by a long-dash-dot-dotted line in red and the probability ($\int_E dE\, F^+_{L_0}$) related to the equivalent transmitted flux density is illustrated by a short-dash-dot-dotted orange line. The contributions related to transmission are labelled within Figure 9 (d), their equivalents related to reflection remain unlabelled for the sake of cleaner graphical presentation but show the same dash-dot pattern.

Within the investigated domain of confinement sizes $\mathscr{L}_L$, the maximum ($\max_E F^-_{L_0}$) with respect to energy of reflected flux density correlated to an occupation of state L_0 ranges from ($\max_E F^-_{L_0}$) = 0.52 %/E_H at $\mathscr{L}_L = 3\ a_B$ to ($\max_E F^-_{L_0}$) = 132.98 %/E_H at $\mathscr{L}_L = 2.63\ a_B$. It has an average value over the studied domain of 17.49 %/E_H and a standard deviation of $168.7\times10^{-3}\ a_B$ but behaves strongly asymmetrical with respect to confinement size $\mathscr{L}_L$. With a long onset at smaller sizes where it grows from a tenth to its peak value over a size range of $\Delta\mathscr{L}_L = 262.7\times10^{-3}\ a_B$, it dies down from the peak value to a tenth for larger sizes over a range of only $\Delta\mathscr{L}_L = 125.4\times10^{-3}\ a_B$. The maximum of transmitted ICEC flux density ($\max_E F^+_{L_0}$) with respect to energy E ranges from ($\max_E F^+_{L_0}$) = 0.41 %/E_H at $\mathscr{L}_L = 3\ a_B$ to ($\max_E F^+_{L_0}$) = 380.60%/E_H at $\mathscr{L}_L = 2.60\ a_B$. It averages to 72.56%/$E_H$ over the studied domain with standard deviation of $567.6\times10^{-3}\ a_B$ which is distributed asymmetrically in favour of smaller confinement sizes $\mathscr{L}_L$. While slowly increasing with confinement size over a range of $\Delta\mathscr{L}_L = 426.9\times10^{-3}\ a_B$ from a tenth to the peak value, the maximal transmitted ICEC flux density $\Delta\mathscr{L}_L = 426.9\times10^{-3}\ a_B$ reduces quickly to a tenth of its peak

value over a range of only $\Delta\mathscr{L}_L = 134.1 \times 10^{-3}\ a_B$ as confinement size increases further.

The maximum of reflective ICEC probability density $\max_E P^-_{L_0}$ with respect to system energy E varies for different capture sizes $\mathscr{L}_L$ from $\max_E P^-_{L_0} = 0.02$ % at $\mathscr{L}_L = 3\ a_B$ to $\max_E P^-_{L_0} = 11.59$ % at $\mathscr{L}_L = 2.67\ a_B$ with an average of 1.41 % and standard deviation of $177.9 \times 10^{-3}\ a_B$. The behaviour with respect to the length parameter $\mathscr{L}_L$ is asymmetric similar to the reflective flux density maximum. Uniformly increasing with $\mathscr{L}_L$ from a tenth to the full peak value over a range of $\Delta\mathscr{L}_L = 230.9 \times 10^{-3} a_B$, it decreases back to a tenth of its peak value over a range of $\Delta\mathscr{L}_L = 123.2 \times 10^{-3} a_B$ towards larger confinement sizes. The maximum of transmissive ICEC probability density $\max_E P^+_{L_0}$ with respect to system energy E varies over the investigated domain of capturing quantum-dot sizes $\mathscr{L}_L$ between $\max_E P^+_{L_0} = 0.02$ % at length $\mathscr{L}_L = 3\ a_B$ and $\max_E P^+_{L_0} = 25.90$ % at length $\mathscr{L}_L = 2.64\ a_B$ with an average of 5.01 % and standard deviation of $251.1 \times 10^{-3} a_B$ over the domain. It increases uniformly with length $\mathscr{L}_L$ from a tenth to its peak value over a range of $573.6 \times 10^{-3}\ a_B$ and decreases quickly over a range of $131.3 \times 10^{-3}\ a_B$ for larger $\mathscr{L}_L$ to a tenth of its peak value.

The total probability $\bar{P}^\pm_{L_0}$ of the interatomic coulombic electron capture is the energy-distribution-weighted integral of the capture probability at each energy E. It thus corresponds to the expectation value of the flux density $F^\pm_{L_0}$ or equivalently the expectation value of the probability $P^\pm_{L_0}(E)$. It is an average over the individual energy contributions and depends on the initial wavepacket. It can be interpreted as the average efficiency of the ICEC experiment. The reflective probability total $\bar{P}^-_{L_0}$ is dependent on the length $\mathscr{L}_L$ of the capturing quantum-dot within the nanowire. It ranges from a probability of $\bar{P}^-_{L_0} = 0.02$ % at length $\mathscr{L}_L = 3\ a_B$ to 0.64 % at $\mathscr{L}_L = 2.59\ a_B$. Its average probability total over the investigated domain of confinement lengths is 0.14 % with standard deviation of $283.3 \times 10^{-3}\ a_B$. The behaviour as function of length $\mathscr{L}_L$ is asymmetric with a long onset at lower lengths and a sharp decrease at lengths above the peak position. The full width at tenth maximum for the total reflective probability $\bar{P}^-_{L_0}$ is thus comprised by $413.9 \times 10^{-3}\ a_B$ for lengths below the peak position at $\mathscr{L}_L = 2.59\ a_B$ and only $187.1 \times 10^{-3}\ a_B$ for lengths above. Over the studied domain of capture lengths $\mathscr{L}_L$, the transmissive total probability $\bar{P}^+_{L_0}$ ranges from a total probability $\bar{P}^+_{L_0} = 0.01$ % at capture length $\mathscr{L}_L = 3\ a_B$ to a total transmissive probability of $\bar{P}^+_{L_0} = 2.83$ % at length $\mathscr{L}_L = 2.48\ a_B$. With length-averaged total probability of 0.74 % and standard deviation of $197.4 \times 10^{-3}\ a_B$, it behaves similarly asymmetrically as the flux density and probability maxima. The full width at tenth maximum is thereby constituted of a long onset of $489.9 \times 10^{-3}\ a_B$ from narrow quantum dots towards the peak value in transmissive total probability $\bar{P}^+_{L_0}$ and $236.7 \times 10^{-3}\ a_B$ for longer capturing confinements.

Summarising, the behaviour as function of capture length $\mathscr{L}_L$ of the maximal flux density $\max_E F^\pm_{L_0}$ with respect to energy E, the maximal probability $\max_E P^\pm_{L_0}$ with respect to energy E and the energy-averaged probability $\bar{P}^\pm_{L_0}$ for transmissive flux density $F^+_{L_0}$ passing the point $z^+ = +200\ a_B$ and reflective flux density $F^-_{L_0}$ passing the point $z^- = -200\ a_B$ in correlation to an occupied state L_0 within the

quantum-confinement region is generally favouring lengths $\mathscr{L}_L$ smaller than the respective optimum. Each quantity climaxes at a different optimal length $\mathscr{L}_L$ but the optimal capture lengths $\mathscr{L}_L$ of the reflective quantities prove to lie above each respective transmissive equivalent and the optimal parameters for maximal capture probability both lie above the optima for maximal flux density which themselves both climax at higher lengths than either of the total probabilities $\bar{P}^{\pm}_{L_0}$. The optimal length for the total reflective capture probability $\bar{P}^{-}_{L_0}$ lies $113 \times 10^{-3}\ a_B$ below the optimal length for the transmissive total probability $\bar{P}^{+}_{L_0}$ and $127 \times^{-3}\ a_B$ below the optimal length for the reflective flux density maximum $\max_E F^{-}_{L_0}$. The transmissive flux density maximum climaxes $\max_E F^{+}_{L_0}$ for a capture length $\mathscr{L}_L$ which is $28 \times 10^{-3}\ a_B$ shorter than the optimum of the maximal reflective flux density $\max_E F^{-}_{L_0}$ and $42 \times 10^{-3}\ a_B$ shorter than the optimal length for the transmissive capture probability maximum $\max_E P^{+}_{L_0}$. The optimal confinement length $\mathscr{L}_L$ for the reflective probability maximum $\max_E P^{+}_{L_0}$ is $29 \times 10^{-3}\ a_B$ longer than the transmissive equivalent $\max_E P^{+}_{L_0}$ and $43 \times 10^{-3}\ a_B$ longer than the reflective flux density maximum $\max_E F^{-}_{L_0}$.

The range in capture length $\mathscr{L}_L$ between the optimum and a tenth of the optimal value for each quantity is by a factor of 2 to a factor of 4 larger for smaller-than-optimal $\mathscr{L}_L$ in comparison with the respective range for larger-than-optimal $\mathscr{L}_L$. This implies that ICEC is more resilient to a change in quantum-dot size at smaller sizes and becomes sensitive to changes in $\mathscr{L}_L$ for sizes above the optimum. This asymmetry is enhanced for the transmissive energy-maximal flux density $\max_E F^{+}_{L_0}$ and probability $\max_E P^{-}_{L_0}$ where the domain of increase from a tenth to the optimal value with increasing length is three times and respectively four times as large as the domain of decrease from the optimal value to a tenth with increasing length. While persisting to favour smaller capture lengths, this asymmetry varies less for the reflective flux density $\max_E F^{-}_{L_0}$ and the reflective probability $\max_E P^{-}_{L_0}$ where the increasing domain of $\mathscr{L}_L$ is twice as large as the decreasing domain. The energy-averaged probability $\bar{P}^{\pm}_{L_0}$ differs less in asymmetry. Transmissive and reflective probability show both a domain roughly twice as broad for lower lengths than for larger ones.

Although it was found in the previous section for capture length $\mathscr{L}_L = 2.83\ a_B$, that the transmissive flux density corresponding to a successful electron capture was considerably smaller than the reflective one, the investigation of varying confinement sizes $\mathscr{L}_L$ as depicted in Figure 9 (d) presents the transmissive ICEC flux and probability as the dominant contributions within the significant domain between $\mathscr{L} = 2.2\ a_B$ and $\mathscr{L}_L = 2.7\ a_B$. The optimal confinement length $\mathscr{L}_L$ of the transmissive energy-averaged probability $\bar{P}^{+}_{L_0}$ coincides with the maximum in interaction energy $V_{L_1 R_0}$ for the simultaneously occupied states L_1 and R_0, the optimal length $\mathscr{L}_L$ for the transmissive ICEC flux density $F^{+}_{L_0}$ coincides with the length at which the energy difference between the states L_1 and R_0 equals the energy difference between the states L_0 and R_0. For the remaining maxima, it is less apparent whether the behaviour as function of confinement length $\mathscr{L}_L$ would coincide with a particular trend in induced by quantum size effect. Because the the initial wavepacket is kept constant with a relatively large range in energy to probe the energy domain, it is not

optimised to obtain a high total probability $\bar{P}^{\pm}_{L_0}$ which is the average over energy. Therefore the energy-maximal probability $\max_E P^{\pm}_{L_0}$ is ten times larger in order than the energy-averaged probability $\bar{P}^{\pm}_{L_0}$ for the wave-packet in this investigation. A narrower wavepacket at appropriate incident energy, however, would allow to optimise the total ICEC probability to come closer to the maximal probability with respect to energy.

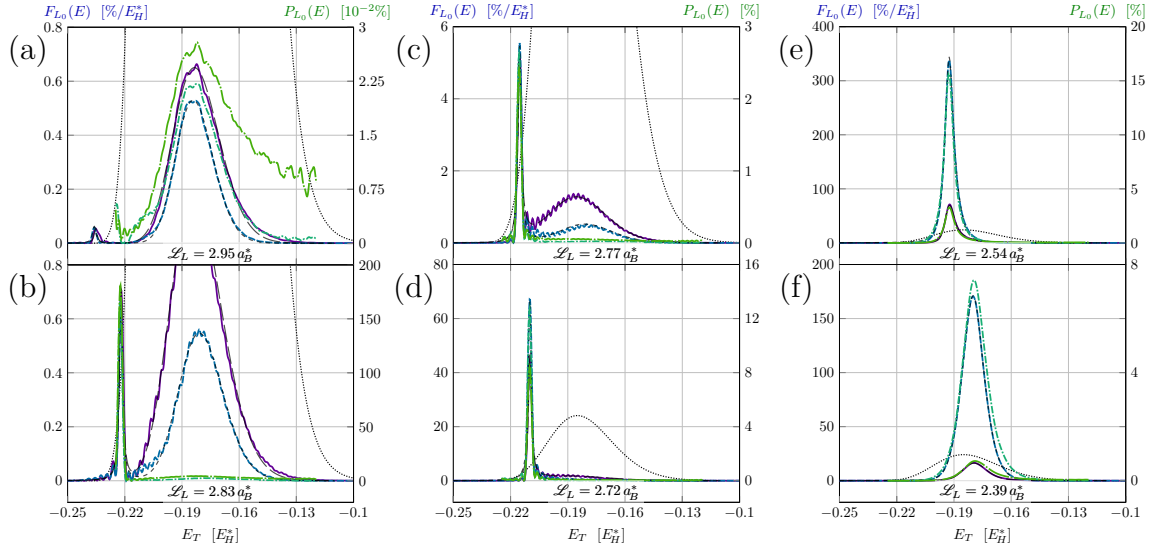

Figure 10: The ICEC induced Electron Flux as function of incident energy for various capture sizes.

While Figure 9 (d) summarises the maximal ICEC flux densities and probabilities over energy at a particular capture length $\mathscr{L}_L$, the individual flux density and probability as function of energy is presented in Figure 10 for six different confinement lengths $\mathscr{L}_L$. A part of these results have been published in Molle et al. [2]. In alignment with Figure 9 (d), the transmissive flux density $F^{+}_{L_0}$ is presented by a short-dashed blue line which is overlain with a slimmer short-dashed grey line indicating a fit to a decay spectrum in superposition with (146). The transmissive probability $P^{+}_{L_0} = F^{+}_{L_0}/F_{\mathtt{i}}$ is indicated by a short-dash-dotted turquoise line for the interval of sufficient incoming flux $F_{\mathtt{i}}$ as depicted by the dotted black line in the background. In addition to Molle et al. [2], Figure 10 also presents the reflective flux density $F^{-}_{L_0}$ by a solid violet line overlain by a long-dashed grey fit and the reflective probability $P^{-}_{L_0} = F^{-}_{L_0}/F_{\mathtt{i}}$ by a green long-dash-dotted line for the interval of sufficiently large incoming flux density. The six panels show the evolution in shape and magnitude of the spectra of ICEC flux density and probability. While the two panels on the left for $\mathscr{L}_L = 2.95\ a_B$ and $\mathscr{L}_L = 2.83\ a_B$ shed a light onto the large-confinement limit, the centre panels for $\mathscr{L}_L = 2.77\ a_B$ and $\mathscr{L}_L = 2.72\ a_B$ depict the region of steep slope towards optimal configurations for flux density and probability. The right-hand panels for lengths $\mathscr{L}_L = 2.54\ a_B$ and $\mathscr{L}_L = 2.39\ a_B$ represent two examples on the long domain of shallow slopes $\Delta F^{\pm}_{L_0}/\Delta\mathscr{L}_L$ and $\Delta P^{\pm}_{L_0}/\Delta\mathscr{L}_L$ for confinement lengths smaller than the optimum.

The incident flux density indicated by the dotted black line in the background has a peak value of $\max_E F_{\mathtt{i}} = 24.09\ E_H^{-1}$ at system energy $E = -185.0 \times 10^{-3}\ E_H$ with full width at half maximum of $39 \times 10^{-3}\ E_H$ and expectation value of $3.996\ E_H^{-1}$. It is slightly asymmetrical in favour of higher energies such that the full width at tenth maximum is composed of a energy difference of $29.7 \times 10^{-3}\ E_H$ from the low-energetic tenth of the maximum to the maximum value and of $41.3 \times 10^{-3}\ E_H$ from the maximum value to its tenth at higher energies. This remains a constant initial condition over all capture lengths $\mathscr{L}_L$. For capture length $\mathscr{L}_L = 2.95\ a_B$ presented in Figure 10 (a), the transmissive ICEC flux density $F_{L_0}^+$ climaxes at energy $E = -182.7 \times 10^{-3}\ E_H$ with $\max_E F_{L_0}^+ = 0.53\ \%/E_H$. The main contribution agrees with a flux density spectrum of a Gaussian wavepacket as is indicated by the grey dashed line and has an expectation value of $0.05\%/E_H$ with standard deviation of $12.2 \times 10^{-3}\ E_H$. Additionally, the transmissive flux density shows a small local maximum of $F_{L_0}^+ = 0.06\ \%/E_H$ at energy $E = -236.0 \times 10^{-3}\ E_H$. Qualitatively, this small and narrow shoulder can be attributed reasonably well to a Lorentzian profile with full width at half maximum of $2.6 \times 10^{-3}\ E_H$. The transmissive ICEC probability $P_{L_0}^+$ as function of energy E thus reaches the maximal value of $\max_E P_{L_0}^+ = 0.02\ \%$ for this set-up at energy $E = 182.5 \times 10^{-3}\ E_H$. It exhibits a full width at half maximum of $28.36 \times 10^{-3}\ E_H$ which is symmetrically distanced from the maximum. However, a shoulder manifests around $E = -210 \times 10^{-3}\ E_H$ which does not appear on the other branch of the curve but may be the consequence of the overall small magnitudes of flux density and resulting probability. The quotient of ICEC flux density by incident flux density $F_{L_0}^+/F_{\mathtt{i}}$ becomes numerically instable for small incident flux densities and has thus been cut off at $F_{\mathtt{i}} \leq 0.15\ E_H^{-1}$ which corresponds to 0.6 % of the maximal incident flux density. This prohibits the evaluation of ICEC probability for the small local flux density maximum at $E = -236.0 \times 10^{-3}\ E_H$.

The reflective ICEC flux density $F_{L_0}^-$ is larger than the transmissive equivalent for the capture length $\mathscr{L}_L = 2.95\ a_B$. With a maximum value of $\max_E F_{L_0}^- = 0.66\ \%/E_H$ at energy $E = -182.2 \times 10^{-3}\ E_H$, it reaches an expectation value of $\bar{F}_{L_0}^- = 0.08\ \%/E_H$ and shows a standard deviation of $14.47 \times 10^{-3}\ E_H$. Its full width at half maximum reads $27.31 \times 10^{-3}\ E_H$ and it can be fitted reasonably well to the flux density spectrum of a Gaussian wavepacket but fluctuates irregularly by approximately $\pm 0.01\%/E_H$ near the maximum as well as near the lower flux densities at the high-energy tail. These fluctuation may however be of numerical nature due to the overall small magnitude of ICEC throughput for this specific set-up. The reflective flux density shows a small local maximum at low energies similarly to its transmissive equivalent. This one is marginally shifted to higher energies with locally maximal flux density $F_{L_0}^- = 0.05\ \%/E_H$ at system energy $E = -235.5 \times 10^{-3}\ E_H$. Moreover, it shows a small shoulder on the decreasing branch towards increasing energy which produces a broadened full width at half maximum of $3.7 \times 10^{-3}\ E_H$. Resulting from the reflective and the incident flux density, the reflective ICEC probability $P_{L_0}^-$ reaches a maximum of $\max_E P_{L_0}^- \approx 0.03\ \%$ at energy $E = -182.0\ E_H$. Opposed to the transmissive equivalent, the reflective probability shows an apparent asymmetric behaviour with respect to energy and favours the branch of energies above that of the maximum where it remains above $6.5 \times 10^{-3}\%$ probability before the cut off. Its full width at half maximum measures $45.3 \times 10^{-3}\ E_H$.

For capture length $\mathscr{L}_L = 2.83\ a_B$ illustrated in Figure 10 (b), the narrow local maximum at the low-energy edge of the incident flux density distribution has significantly grown in comparison to length $\mathscr{L}_L = 2.95\ a_B$. This particular set-up has already been analysed above in Figure 7 including additional contributions to the overall flux density and has been compared there to a reference simulation without electron-electron interaction. Figure 10 (b) now emphasizes the evolution of the transmissive and reflective ICEC contributions with respect to capture length variation and its consequences for the ICEC probability.

The transmissive flux density has narrow and sharp peak at energy $E = -222.3 \times 10^{-3}\ E_H$. It has a flux density of $\max_E F^+_{L_0} = 0.61\ \%/E_H$, a full width at half maximum of only $2.5 \times 10^{-3}\ E_H$ and a full width at tenth maximum of only $4.2 \times 10^{-3}\ E_H$. It shows a second broad-banded feature at higher energies, however, which has a local maximum of $F^+_{L_0} = 0.56\ \%/E_H$ at energy $E = -181 \times 10^{-3}\ E_H$ with full width at half maximum of $26.6 \times 10^{-3}\ E_H$. The narrow peak is well fitted by a Lorentzian profile while the broad part around the smaller local maximum is well represented by the energy distribution of a Gaussian wavepacket. The final sum of square residuals of such a fit as shown by the grey thin dashed line is $3.3428 \times 10^{-6}\ E_H^{-2}$. The small oscillatory deviations from the fit line of order of magnitude of $10^{-4}\ \%/E_H$ arise from the numerical Fourier transformation of the flux density as function of discrete time steps.

The transmissive ICEC probability arising from the flux density is strongly prioritising the narrow peak at low energy over the broad feature around the incident flux density maximum near $E = -185 \times 10^{-3}\ E_H$. Just past the numerical cut-off energy, the probability reaches its global maximum at $\max_E P^+_{L_0} = 1.66\ \%$ at energy $E = -222.5 \times 10^{-3}\ E_H$ with full width at half maximum of $2.4 \times 10^{-3}\ E_H$ and full width at tent maximum of $4.2 \times 10^{-3}\ E_H$. The broader feature found in the flux density spectrum is diminished by two orders of magnitude to a local maximum of $P^+_{L_0} = 0.02\ \%$ at energy $E = -178.2 \times 10^{-3}\ E_H$ which is shifted to higher energies with respect to the broad-banded feature in the flux density. It shows a full width at half maximum of $36.8 \times 10^{-3}\ E_H$.

In contradiction to the transmissive flux density, the reflective flux density favours the broad feature at central energies of the energy distribution over the narrow peak at the lower-energetic edge. The global maximum of $\max_E F^-_{L_0} = 1.06\ \%/E_H$ is therefore found at energy $E = -185.2 \times 10^{-3}\ E_H$ with full width at half maximum of $31.1 \times 10^{-3}\ E_H$, whereas a local maximum of $F^-_{L_0} = 0.71\ \%/E_H$ manifests at energy $E = -222 \times 10^{-3}\ E_H$ with respective full width at half maximum of $2.7 \times 10^{-3}\ E_H$ and full width at tenth maximum of $4.6 \times 10^{-3}\ E_H$. The reflective flux density spectrum is well described by a supperposition of a Lorentzian profile and a energy density profile for a Gaussian wavepacket, which is indicated by a grey thin dashed line in Figure 10 (b) with final sum of square residuals of $8.7100 \times 10^{-6}\ E_H^{-2}$.

Nevertheless, the reflective probability density remains in favour of the sharp peak rather than the broader feature which is due to the strong asymmetry in the quotient of reflective ICEC flux density by incident one $F^-_{L_0}/F_{\mathtt{i}}$. So the global maximum of $\max_E P^-_{L_0} = 1.8\ \%$ is reached at energy E$=-22.3 \times 10^{-3}\ E_H$ with full width at half maximum of $2.7 \times 10^{-3}\ E_H$ and full width at tenth maximum

of 4.7×10^{-3} E_H, whereas the second local probability maximum of only $P^-_{L_0} = 0.04\%$ manifests at energy $E = -182.7 \times 10^{-3}$ E_H with full width at half maximum of 65.2×10^{-3} E_H. While the local maxima around the maximal incident flux density near -185×10^{-3} E_H remain visible for flux density and probability in both directions, that of reflection and that of transmission, they become orders of magnitude smaller in the probability spectrum for confinement length $\mathscr{L}_L = 2.83$ a_B than the narrow feature at the low-energy edge of the incident energy spectrum which remains of similar order as for the confinement length $\mathscr{L}_L = 2.95$ a_B, however, as discussed with Figure 10 (a). The reflective probability remains larger than the transmissive one for both confinement lengths which will change for smaller lengths though.

At confinement length $\mathscr{L}_L = 2.77$, the maxima in transmissive flux density and transmissive ICEC probability exceed their reflective counterparts but retain the features of a sharp peak at low energies and a broad local maximum near the incident flux density maximum. The transmissive ICEC flux density $F^+_{L_0}$ climaxes thereby at a value of $\max_E F^+_{L_0} = 5.55$ $\%/E_H$ at energy $E = -215.2 \times 10^{-3}$ E_H with full width at half maximum of 2.6×10^{-3} E_H and full width at tenth maximum of still only 4.4×10^{-3} E_H. It offers a second maximum of flux density $F^+_{L_0} = 0.51$ $\%/E_H$ at energy $E = -180.2 \times 10^{-3}$ E_H with a broader full width at half maximum of 28.3×10^{-3} E_H. This behaviour can be described by a superposition of a Lorentzian spectrum with the spectrum of a Gaussian wavepacket indicated by the grey thin dashed line in Figure 10 (c) of final sum od square residuals of 182.73×10^{-6} E_H^{-2}.

The transmissive ICEC probability peaks to $\max_E P^+_{L_0} = 2.615$ at energy $E = -215.5 \times 10^{-3}$ E_H with full width at half maximum of 2.6×10^{-3} E_H and full width at tenth maximum of still only 3.9×10^{-3} E_H. It carries on to present a second broad-banded feature of local maximum in ICEC probability $P^+_{L_0} = 0.02$ % at energy $E = -172.7 \times 10^{-3}$ E_H of a broad full width at half maximum of 41.9×10^{-3} E_H. However, the oscillatory fluctuations in probability near the edges of either branch of the narrow peak appear of similar order of magnitude to the broad feature around the maximum of incident flux density distribution.

Whereas the maximum in reflective ICEC flux density $\max_E P^-_{L_0} = 5.16$ % at energy $E = -215.2 \times 10^{-3}$ E_H amounts to less than the maximum of transmissive flux density, its second local maximum of $P^-_{L_0} = 1.36$ $\%/E_H$ provided by a broad feature at energy $E = -184.5 \times 10^{-3}$ E_H near the incident flux density maximum is twice as strong as the transmissive equivalent and of same order of magnitude as its narrow overall maximum. The full width at half maximum of 32.6×10^{-3} E_H of the broader feature measure about twelve times that of the narrow peak with full width at half maximum of 2.3×10^{-3} E_H which measures a similarly narrow full-width at tenth maximum of 4.4×10^{-3} E_H as the equivalent narrow peaks at the two larger confinement lengths. A description by superposition of a Lorentzian profile and the energy distribution of a Gaussian wavepacket thus appear successful with a final sum of square residuals of 215.13×10^{-6} E_H^{-2} as depicted by the grey thin long-dashed line in Figure 10 (c).

The maximum in reflective ICEC probability touches $\max_E P^-_{L_0} = 2.41$ % at energy $E = -215.5 \times 10^{-3}$ E_H. It spreads to a full width at half maximum over

$2.6 \times 10^{-3}\ E_H$ and to a full width at tenth maximum over $3.9 \times 10^{-3}\ E_H$. As the narrow peak in the reflective flux density has shifted to higher energies in comparison to the two larger confinement length discussed above, the estimate of reflective ICEC probability by evaluating the quotient of reflective flux density by incident one $F^-_{L_0}/F_{\mathrm{i}}$ defies a clear distinction of the two features of different bandwidth. The reflective probability thus appears as asymmetric sharp peak at the low-energetic edge of the incident flux density spectrum and presents a long tail towards higher energies. This tail extents over the entire incident spectrum but fails to reach a tenth of the maximum probability.

For the capturing confinement length of $\mathscr{L}_L = 2.72\ a_B$, the the narrow peak in the reflective and transmissive ICEC flux densities $F^{\pm}_{L_0}$ as well as ICEC probabilities $P^{\pm}_{L_0}$ grows and shifts further towards higher energies and merges with the broader feature centred near the incident flux density maximum. The transmissive flux density $F^+_{L_0}$ dominates clearly over its reflective equivalent $F^-_{L_0}$ at the narrow peak but remains inferior over the broad-banded shoulder at higher incident flux densities. Maximal with $\max_E F^+_{L_0} = 67.08\ \%/E_H$ at energy $E = 210.0 \times 10^{-3}\ E_H$, the transmissive flux density exhibits a full width at half maximum of $2.5 \times 10^{-3}\ E_H$ and a full width at tenth maximum of still only $4.2 \times 10^{-3}\ E_H$. The broad feature around the incident flux density maximum which was observed distinctly and clearly for the three examples of higher capture size $\mathscr{L}_L$, now only manifests as a shoulder below a tenth of the transmissive flux density maximum. Effectively, the transmissive flux density of this broad-banded shoulder has retained the same order of magnitude as for the previous examples discussed and shown in Figure 10 (a-c) but cannot match the increasing magnitude of the narrow flux density feature. Nevertheless, a description by superposition of a Lorentzian profile and the spectrum of a Gaussian wavepacket proves successful still with a final sum of square residuals of $23.518 \times 10^{-3}\ E_H^{-2}$.

The transmissive ICEC probability climaxes here with $\max_E P^+_{L_0} = 12.69\%$ at energy $E = -210.0 \times 10^{-3}\ E_H$ as depicted in Figure 10 (d) by the turquoise dash-dotted line. While the probability resembles at first glance a Lorentzian spectrum as was suggested previously in Pont et al. [8], the positioning along the increasing branch of the incident flux density spectrum and the superposing broad-banded shoulder of the transmissive ICEC flux density at higher energies do force an asymmetrical shape on the ICEC probability spectrum which manifests in a long tail towards the centre of the incident flux density spectrum at higher energy. This takes place below the threshold of a tenth of the maximum, however, such that the typical full width at half maximum of $2.5 \times 10^{-3}\ E_H$ and full width at tenth maximum of $4.2 \times 10^{-3}\ E_H$ are sustained.

The reflective ICEC flux density has a maximum $\max_E F^-_{L_0} = 44.76\ \%/E_H$ at energy $E = -209.7 \times 10^{-3}\ E_H$. It shows the typical full width at half maximum of $2.5 \times 10^{-3}\ E_H$ and full width at tenth maximum of $4.3 \times 10^{-3}\ E_H$ which were already observed in the previous examples. Attached to the decaying branch at higher energies, a broad shoulder manifests which outweighs its transmissive equivalent by a factor of 3. In spite of the two features appearing not as distinctly positioned as for larger capture lengths $\mathscr{L}_L$, the description by superimposing a Lorentzian profile

with the spectrum of a Gaussian wavepacket remains successful with a final sum of square residuals of $14.908 \times 10^{-3}\ E_H^{-2}$. The resulting reflective ICEC probability culminates at $\max_E P_{L_0}^- = 8.36\ \%$ at energy $E = -210.0 \times 10^{-3}\ E_H$ and similar full widths at half maximum of $2.5 \times 10^{-3}\ E_H$ and at tenth maximum of $4.3 \times 10^{-3}\ E_H$. In accord with the examples discussed above, it holds a long tail towards the centre of the incident flux density at higher energies but with probability magnitude below the tenth maximum threshold.

For the example of capture length $\mathscr{L}_L = 2.54\ a_B$ shown in Figure 10 (e), the peak in transmissive and reflective flux density shifts further to higher energies over the spectrum of the Gaussian wavepacket which induces a tilting of the profile. The decreasing branch with respect to increasing energy is passing the point of maximal incident flux density which leads to an asymmetric broadening of the width at tenth maximum in favour of higher energies. The transmissive flux density reaches $\max_E F_{L_0}^+ = 338.1\ \%/E_H$ at energy $E = -192.5 \times 10^{-3}\ E_H$. While the full width at half maximum of $5.7 \times 10^{-3}\ E_H$ is increased by a factor of 2.3 with respect to $\mathscr{L}_L = 2.72\ a_B$, the full width at tenth maximum is increased by a factor 3.6 to measure $15.1 \times 10^{-3}\ E_H$ in total. As measure of asymmetry, the energy difference on the increasing branch between the tenth maximum and the maximal transmissive flux density measures $6.6 \times 10^{-3}\ E_H$ while the branch of decreasing flux density with increasing energy measures a width of $8.5 \times 10^{-3}\ E_H$ between the maximum and its tenth. By this, the expectation value of the transmissive flux density retains $\bar{F}_{L_0}^+ = 100.1\ \%/E_H$. A description by superposition of a Lorentzian with the spectrum of a Gaussian wavepacket proved here equally successful and yielded a final sum of square residuals below $40.278 \times 10^{-3}\ E_H^{-2}$.

Consequently, the transmissive ICEC probability attains $\max_E P_{L_0}^+ = 15.69\ \%$ at energy $E = -192.8 \times 10^{-3}\ E_H$. It has a full width at half maximum of $5.7 \times 10^{-3}\ E_H$ and a full width at tenth maximum of $15.5 \times 10^{-3}\ E_H$. With partial widths at tenth maximum of $7.2 \times 10^{-3}\ E_H$ and $8.3 \times 10^{-3}\ E_H$ on the branch of respectively increasing and decreasing probability with increasing energy, the transmissive ICEC probability behaves less asymmetrical with respect to energy than the transmissive flux density. The decreasing branch at higher energies remains in slight favour though.

The maximum value of reflective flux density is significantly smaller than the transmissive one. With $\max_E F_{L_0}^- = 71.2\ \%/E_H$ at energy $E = 192.3 \times 10^{-3}\ E_H$, it remains below a quarter of the respective maximum in transmissive flux density. Moreover, it appears slightly broader and less symmetrical with a full width at half maximum of $6.0 \times 10^{-3}\ E_H$ and full width at tenth maximum of $17.5 \times 10^{-3}\ E_H$ of which the partial widths from maximum to its tenth measure $6.2 \times 10^{-3}\ E_H$ for the increasing branch and $11.3 \times 10^{-3}\ E_H$ for the branch of decreasing reflective flux density with increasing energy. A description by superposition of a Lorentzian with the spectrum of a Gaussian wavepacket proves to remain nevertheless successful with a final sum of square residuals below $4.0761 \times 10^{-3}\ E_H^{-2}$.

Similarly, the reflective probability maximum with respect to energy stays with $\max_E P_{L_0}^- = 3.28\ \%$ at energy $E = 192.5 \times 10^{-3}\ E_H$ below a quarter of the trans-

missive probability maximum. The full width at half maximum spans $6.0 \times 10^{-3}\ E_H$. Whereas the partial width from maximum to its tenth narrows to $6.7 \times 10^{-3}\ E_H$ for the increasing branch, it broadens to $11.0 \times 10^{-3}\ E_H$ on the branch of decreasing ICEC probability with increase in energy. As result, the full width at tenth maximum spans $17.7 \times 10^{-3}\ E_H$.

Opposed to the previous set-ups, the maxima of both ICEC flux densities and probabilities appear at energies above that of the maximal incident flux density for the capture length $\mathscr{L}_L = 2.39\ a_B$ depicted in Figure 10 (f) and span over more than twice the bandwidth at half maximum observed for capture length $\mathscr{L}_L = 2.54\ a_B$.

The transmissive flux density arrives at $\max_E F^+_{L_0} = 170.60\ \%/E_H$ at energy $E = -180.0 \times 10^{-3}\ E_H$. The full width at half maximum spans $13.4 \times 10^{-3}\ E_H$. Of similar magnitude, the partial width between the maximum and its tenth measures $13.5 \times 10^{-3}\ E_H$ on the branch of increasing flux density with increase in energy and $14.3 \times 10^{-3}\ E_H$ over the decreasing branch. This amounts to a full width at tenth maximum of $27.8 \times 10^{-3}\ E_H$. Describing the curve by a superimposed Lorentzian with the spectrum of a Gaussian wavepacket achieves a numerical accuracy in the final sum of square residuals of $2.0929 \times 10^{-3}\ E_H^{-2}$ as illustrated by the thin grey short-dashed line overlaying the cyan short-dashed line representing the transmissive flux density $F^+_{L_0}$ in Figure 10 (f).

The transmissive ICEC probability remains asymmetrically distributed with longer tail in favour of higher energies. Climaxing with a probability of $\max_E P^+_{L_0} = 7.42\ \%$ at energy of $E = -179.5 \times 10^{-3}\ E_H$, it dissipates to a full width at half maximum of $14.4 \times 10^{-3}\ E_H$ and a full width at tenth maximum of $31.4 \times 10^{-3}\ E_H$. This is composed of the partial width of $14.4 \times 10^{-3}\ E_H$ between maximal probability and its tenth on the branch of increasing probability with increase in energy and of $16.9 \times 10^{-3}\ E_H$ on the decreasing branch such that it appears broadened towards higher energies with respect to the transmissive flux density. This is depicted in Figure 10 (f) where the increasing branches of transmissive ICEC flux density in cyan short-dashed line and of transmissive ICEC probability in turquoise short-dash-dotted line overlay while the decreasing branch of the probability delays to higher energies in comparison to the flux density.

Less than a tenth of its transmissive equivalent, the reflective flux density reaches only a maximum of $\max_E F^-_{L_0} = 16.58\ \%/E_H$ at energy $E = -179.5 \times 10^{-3}\ E_H$. Its full width at half maximum spans over $14.3 \times 10^{-3}\ E_H$. Its partial widths between maximal flux density and its tenth maximum carry $13.8 \times 10^{-3}\ E_H$ for the increasing and $17.3 \times 10^{-3}\ E_H$ for the branch of decreasing flux density with respect to an increase in energy. The full width at tenth maximum of $31.1 \times 10^{-3}\ E_H$ thereby favours the larger energies. Although not showing distinctly, a superposition of a Lorentzian profile and a Gaussian wavepacket spectrum describes the transmissive flux density as function of energy to an accuracy given by a final sum of square residuals amounting to only $301.1 \times 10^{-6}\ E_H^{-2}$.

In consequence, the maximum in reflective ICEC probability of $\max_E P^-_{L_0} = 0.73\ \%$ at energy $E = -179.0 \times 10^{-3}\ E_H$ fails to touch a tenth of its transmissive equivalent

but dissipates to half its maximum over a full width of 15.9×10^{-3} E_H and to a tenth of its maximum over a full width of 39.9×10^{-3} E_H. The partial width of 25.3×10^{-3} E_H from maximum to its tenth on the branch of decreasing ICEC probability with respect to an increase in energy reaches nearly $\frac{7}{4}$ of the partial width on the uniformly increasing branch which spans over 14.6×10^{-3} E_H. As result, the increasing branches of reflective flux density represented by a solid violet line and that of the reflective ICEC probability represented by a green long-dash-dotted line coincide in Figure 10 (f) but the uniformly decreasing branch of the probability appears delayed to higher energies compared to the decreasing branch of the flux density.

In all six set-ups, the reflective and the transmissive flux densities are successfully represented by a superposition of a spectrum of Lorentzian shape with a spectrum of a Gaussian wavepacket. In order of their presentation, from large capture lengths $\mathscr{L}_L$ to smaller ones, the Lorentzian profile changes position from lower energies to higher energies and passes through different sections of the incident flux density distribution. The Gaussian spectrum appears to retain its order of magnitude and energetic position near the centre of the incident flux density spectrum such that it shows distinctly for Figure 10 (a-c) but merges with the Lorentzian shape to an asymmetric profile for Figure 10 (d-f). The successful description by a Gaussian spectrum in part suggests a subprocess in the interatomic coulombic electron capture where the incident electron represented by the Gaussian wavepacket transfers its kinetic energy through a direct impulse onto the encountered partner electron. In contrast, the partial description by a Lorentzian spectrum alludes to a subprocess involving an exponential decay in time. The incident electron is thus partially bound to an intermediate state simultaneously with the encountered partner electron before decaying resonantly to the final capturing state L_0 through release of the partner electron. This aspect represents the process of the so-called interatomic coulombic decay.[72] Because the initial energy distribution is kept constant throughout this study, the Gaussian contributions to the ICEC spectra appear less affected by the change of the capturing confinement size $\mathscr{L}_L$. The electron capture with consecutive decay, however, depends strongly on the resonant energy of the intermediary state. The quantum size effect therefore leads to a shifting position of the Lorentzian contribution to the ICEC spectrum as function of the capturing confinement length $\mathscr{L}_L$. In addition, the electron capture ratio is strongly affected and varying over two orders of magnitude.

The respective transmissive and reflective spectra of capture through direct impulse are positioned at different group energies. This implies that transmission and reflection coefficients differ energy-dependently which is induced by the confinement potential itself as was shown and discussed above in relation to Figure 8 and which is further modified by the Coulomb interaction potential between the electrons. Overall, it appears advantageous to let the spectra of the two subprocesses overlap significantly. Furthermore, it was observed here that the width of the ICEC spectra increased with decreasing capture size $\mathscr{L}_L$ where the Lorentzian and Gaussian contributions appeared to merge in the spectrum of the flux density and that the spectra were distributed asymmetrically in favour of higher energies. The reflective quant-

ities showed larger asymmetry than the transmissive ones in each of the discussed examples. In the set-ups investigated here, ICEC through direct impulse appeared to favour electron emission in reflection direction while the contributions through ICD favoured an emission in transmission direction. At set-ups of significant ICEC flux density, the transmissive ICEC flux density and probability outweighed their reflective equivalents.

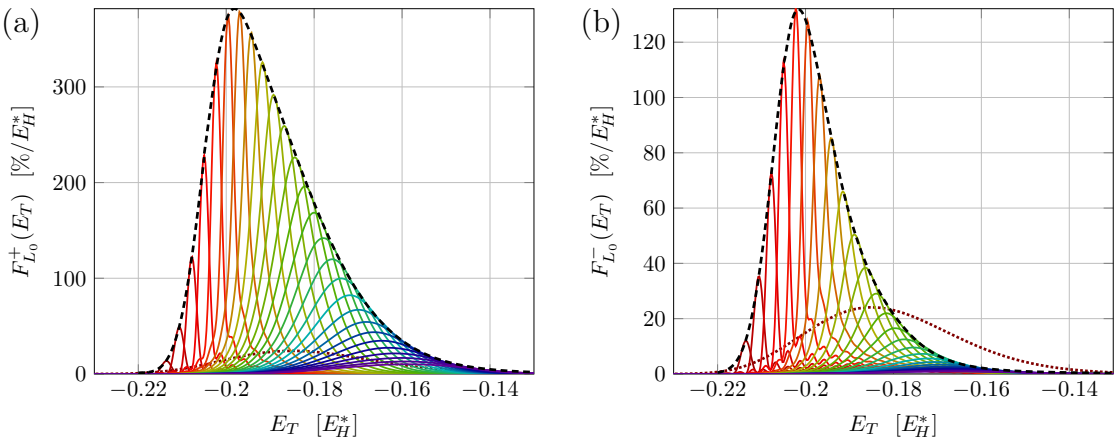

Figure 11: The development of transmitted ICEC flux spectrum $F^{\pm}_{L_0}(E)$ with changing size of the capturing quantum confinement. The coloured solid lines represent individual flux density spectra each at a different confinement size, the dotted line represents the scaled spectrum of incident flux $10^{-2}F_{\mathrm{i}}$, the dashed line represents the envelope function $\max_{\mathscr{L}_L} F^{\pm}_{L_0}$ of all ICEC flux density spectra. (a) Flux density $F^{+}_{L_0}$ as function of energy E measured in transmission direction in correlation with an occupied capture state L_0 within the confinement region. Adapted from Molle et al. [2]. (b) Energy dependence of flux density $F^{-}_{L_0}$ measured in reflection direction in correlation with an occupied state L_0.

Whereas Figure 10 shows examples of flux density and probability profiles at different capturing confinement sizes $\mathscr{L}_L$ which complement the discussion of the evolution of the peak values with Figure 9 (d), it is possible to present transmissive and reflective ICEC flux density profiles in juxtaposition to each other and to the incident flux density spectrum. Figure 11 thus illustrates the 52 most prominent ICEC flux density spectra in transmission and reflection direction to indicate their difference to each other and the incident flux density and their evolution with respect to a variation of confinement size $\mathscr{L}_L$. In their collective representation, these curves appear to allude to an envelope function limiting the respective shape and size of ICEC flux density in either direction. Showing a steep rise in magnitude on the side of low energies, both ICEC flux densities broaden in their spectra while they drop more slowly in magnitude towards higher energies above the optimum. Noticeably, the optimal transmissive flux density is reached at higher energies than the optimal reflective flux density. At the same time, the reflective flux densities cover less bandwidth than the transmissive ones and reach only a third of the optimal

transmissive flux density. During this study, both flux densities find their optimum at energies smaller than that of the maximal incident flux density.

At first glance, the envelope of the flux density spectra appears to be of shape of a Maxwell-Boltzmann energy distribution. On closer inspection, however, its energetic width proves to be more closely matched by a superposition of a Lorentzian with the spectrum of a Gaussian wavepacket, a one-dimensional Maxwell-Boltzmann energy distribution. This is consistent with the discussion of the individual flux densities. The analytical spectrum of the single-dimensional wavepacket involves square roots of energy and their reciprocal value though which complicates numerical fitting by involving limited domains and division by zero. A construction of the envelope function for the transmissive and reflective case was thus most successful by fitting the two respective branches from the maximum individually. While this may suggest the necessity of a more involved consideration of the expected overall spectrum and ways to improve numerical stability of the superposition of the two complex solutions that lead to Lorentzian and Gaussian energy spectra, it proves nevertheless that both, the transmissive and reflective envelope function are of the same family of functions. These envelopes are drawn in Figure 11 by a black dashed line. On the other hand, the difference in composition of the increasing and decreasing branch for the envelope functions may also be rooted in the fact that transmission and reflection coefficients from confinement potential and interaction potential are energy-dependent and thus modify the shape. This exceeds the scope of this work, however, and shall not be of further concern here. It suffices at this point to find the envelope function can be successfully constructed to some extent by careful superposition of a Lorentzian and Gaussian energy spectrum.

The envelope $\max_{\mathscr{L}_L} F^+_{L_0}(E)$ of the transmissive flux densities at varying capture lengths $\mathscr{L}_L$ as function of system energy E thus ranges from $\max_{\mathscr{L}_L} F^+_{L_0} = 1.18\ \%/E_H$ at energy $E = -220.0 \times 10^{-3}\ E_H$ to its maximum over energy $\max_{\mathscr{L}_L,E} F^+_{L_0} = 381.7\ \%/E_H$ at energy $E = -198.1 \times 10^{-3}\ E_H$. It shows an expectation value in flux density of $92.9\ \%/E_H$ with standard deviation of $14.0 \times 10^{-3}\ E_H$. The full width at half maximum spans $24.9 \times 10^{-3}\ E_H$ which is composed by more than two thirds by the partial width from maximum to its half on the branch of decreasing flux density with increasing energy. At the tenth maximum, the decreasing branch makes up nearly three quarters of the total full width of at tenth maximum which spans over a total of $50.4 \times 10^{-3}\ E_H$. It thus provides an increasingly long tail on the branch of higher energies whereas it dies down more quickly on the side of low energies.

For the illustrated energy domain, the envelope $\max_{\mathscr{L}_L} F^-_{L_0}(E)$ of reflective flux densities at varying capture lengths $\mathscr{L}_L$ as function of the system energy E ranges from $\max_{\mathscr{L}_L} F^-_{L_0} = 0.33\ \%/E_H$ on the edge at energy $E = -130 \times 10^{-3}\ E_H$ to its maximum of $\max_{\mathscr{L}_L,E} F^-_{L_0} = 131.90\ \%/E_H$ at energy $E = 201.6 \times 10^{-3}\ E_H$. It averages to an expectation value of only $30.79\ \%/E_H$ with standard deviation of $10.1 \times 10^{-3}\ E_H$. The full width at half maximum spans over $16.9 \times 10^{-3}\ E_H$ of which only three fifth are made up by the partial width on the decreasing branch with increasing energy. At tenth maximum, the partial width on the decreasing

branch provides slightly more than two thirds of the full width which measures $37.9 \times 10^{-3}\ E_H$ in total.

The envelope function of the reflective flux density diminishes faster with higher energies than the envelope for the transmissive ICEC flux density whereas the increase towards the respective maximum with increasing energy for lower energies is comparable. The maximum of the reflective envelope already remains below a third of its transmissive equivalent and it has already died down below a fifth of its maximum value at energy $E = -181.1 \times 10^{-3}\ E_H$ where the envelope of transmissive ICEC flux density reaches the respective half maximum value. At energy $E = -175.5 \times 10^{-3}\ E_H$, the reflective envelope reaches the tenth maximum while the transmissive envelope function is still above a third of its respective maximum value. In contrast, the energetic difference between the respective tenth maximum measures only $2.1 \times 10^{-3}\ E_H$ on the side of lower energies and both curves' half maxima lie within $2.3 \times 10^{-3}\ E_H$ from each other. The respective maxima then differ in energy by $3.5 \times 10^{-3}\ E_H$.

In summary, Figure 11 provides insight into the optimal limits of the transmissive and reflective ICEC flux density as function of energy which complements the information provided on the limits of the two flux density contributions as function of confinement size illustrated in Figure 9 (d). The transmissive flux continues to become more relevant than the reflective flux. At energies of maximal flux density below approximately $200 \times 10^{-3}\ E_H$ corresponding to a capture size below $\mathscr{L}_L = 2.62\ a_B$, the transmissive and reflective flux density spectra both appear narrow. The envelope functions grow with energy over a similar energy difference towards there maximum value but the transmissive flux exceeds the reflective by a factor of three. For energies above approximately $200 \times 10^{-3}\ E_H$ corresponding to capture sizes above $\mathscr{L}_L = 2.62\ a_B$, the flux density spectra broaden with increasing energy and get smaller in value. The transmissive flux is more resilient to a deviation from the optimal capture size $\mathscr{L}_L$ such that the envelope function of transmissive flux density retains more significant values over a longer bandwidth at energies above the optimal energy than its reflective counterpart. The transmissive flux density is therefore expected to dominate for larger confinement sizes and at higher energies. The individual flux density spectra were successfully described by a superposition of a Lorentzian profile with the spectrum of a Gaussian wavepacket. This implies that there are two distinct subprocesses involved in an interatomic coulombic electron capture into the state L_0 within this investigation: A decay process of an intermediary capture state giving rise to an energy selection of some bandwidth around the resonant energy of the intermediary state, and an energy transfer through direct impulse from the incident electronic Gaussian wavepacket on the partner electron which gives rise to a modified spectrum of another Gaussian wavepacket in the measured ICEC flux density where the confinement potential itself and the Coulomb interaction between the electrons act as modifiers. While it was found here that an envelope function exists for either transmissive or reflective ICEC flux density, that describes the optimal flux density to be measured at an energy E, the respective envelope function appears to be modified by the energy-dependence of the reflection and transmission coefficients arising from the confinement potential.

6.2.3 Capture Efficiency

Since it was found in the previous subsections that the confinement potential itself modifies the measured flux density related to the interatomic coulombic electron capture, the following will attempt to generalise the found dependence of ICEC flux on the confinement parameters by a variation of capturing confinement size $\mathscr{L}_L$, continuum threshold energy D_L of the capturing quantum dot, and the distance $\mathscr{R}$ between the centres of the two involved quantum confinements. In a potential electronic device exploiting ICEC induced electron flux in a nanowire, the transmissive flux will play the predominant role in the application as it has been shown above, the electronic charge within the confinement region hinders general transmission apart from ICEC while reflected flux contributions will interfere with the incident flux and with each other. Due to this and the shown advantageous dominance of the transmissive flux density, the following study will concentrate on the transmissive ICEC probability only. The data on ICEC probability presented and analysed hereafter has also been subject of the recent publication of a scientific article by Pont et al. [64] discussing limiting conditions for a successful interatomic coulombic electron capture and the estimation of such relations from single-electronic quantities.

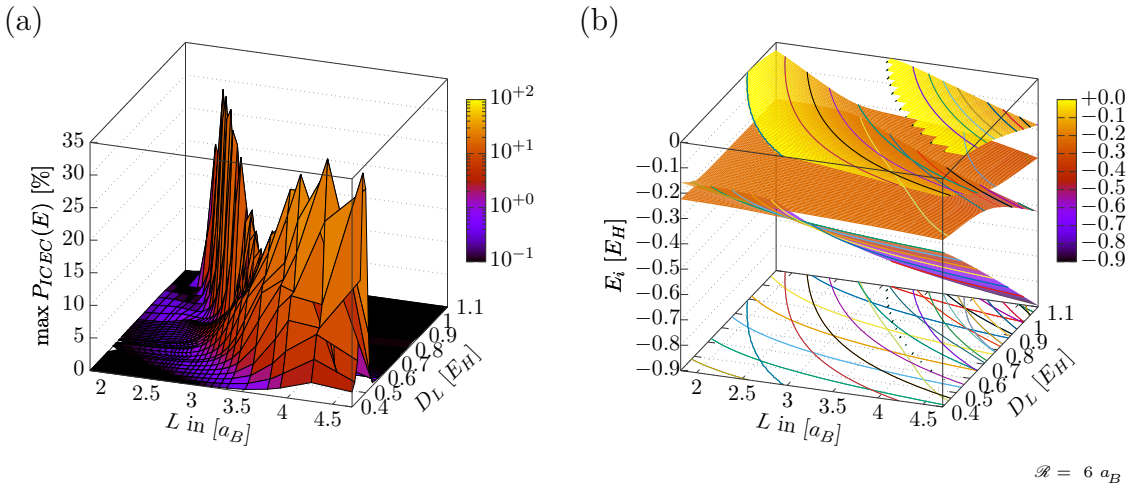

Figure 12: The maximal efficiency of interatomic coulombic electron capture in a pair of quantum confinements embedded in a nanowire as function of acceptor length $\mathscr{L}_L$ and its confinement strength D_L at centre-to-centre distance $\mathscr{R} = 6\ a_B$. (a) ICEC efficiency as landscape in parameter space $(\mathscr{L}_L, D_L)$. (b) Single-electron eigenenergy surfaces and contour lines of constant energy in parameter space.

In line with the evaluation of the transmissive ICEC probability $P^+_{L_0}$ for Figure 10 as quotient of flux density measured in transmission direction in correlation with an occupied capture state L_0 by the incident flux density, such a spectrum can be determined for every pair of parameters $(\mathscr{L}_L, D_L)$. Extracting the maximal probability $\max_E P^+_{L_0}$ in each of those spectra allows to visualise it as a landscape of coordinates $(\mathscr{L}_L, D_L)$ which is illustrated in Figure 12 (a) for a distance of $\mathscr{R} = 6\ a_B$ between the two confinement centres. The ICEC probability varies between 0.0 % and a

maximum of 34.57 % at a confinement length of $\mathscr{L}_L = 4.26\ a_B$ and a continuum threshold of $D_L = 0.52\ E_H$.

The ICEC probability function $\max_E P^+_{L_0}(\mathscr{L}_L, D_L)$ in the sampled parameter space manifests in a rather narrow comb from $P = 31.6$ % at length $\mathscr{L}_L = 2.39\ a_B$ and continuum threshold energy $D_L = 1.00\ E_H$ in the background on the left hand side of Figure 12 (a) decreasing slowly via $P = 26.03$ % at length $\mathscr{L}_L = 2.89\ a_B$ and threshold energy $D_L = 0.80\ E_H$ down to a probability of $P = 12.44$ % at length $\mathscr{L}_L = 3.33\ a_B$ and threshold $D_L = 0.68\ E_H$ and increasing again via $P = 27.85$ % at length $\mathscr{L}_L = 3.78\ a_B$ and threshold $D_L = 0.57\ E_H$ up to a probability of $P = 34.57$ % at length $\mathscr{L}_L = 4.26\ a_B$ and threshold energy $D_L = 0.52\ E_H$ shown in Figure 12 (a) in the foreground at the edge on the right hand side. This line of highest probabilities on the map of parameter coordinates $(\mathscr{L}_L, D_L)$ is positioned in a slope of $\Delta D_L/\Delta\mathscr{L}_L = (-266 \pm 17) \times 10^{-3} E_H/a_B$ with interpolated intercept with the D_L-axis at $(+159 \pm 53) \times 10^{-3} E_H$ and a linear correlation coefficient of -97.95 % between the two parameters. Owing to the narrow-combed distribution of the probability, the average probability in the sampled parameter space reaches only 2.93 % with weighted average coordinates of length $\mathscr{L}_L = 3.21\ a_B$ and threshold $D_L = 0.67\ E_H$. Interestingly, the onset of probability which is highlighted by a purple colour in Figure 12 (a) appears to partially separate from the main strand of high probability into another yet weaker branch for confinement lengths below $\mathscr{L}_L = 3\ a_B$ and thresholds around $D_L = 0.6\ E_H$ to $D_L = 0.9\ E_H$. While they are clearly seperated for lengths below $\mathscr{L}_L = 2.5\ a_B$, their recombination coincides on the one hand with the observed local reduction of ICEC probability on the major branch as described above and coincides on the other hand with the position of the sample average whose probability-weighted standard deviation measures $0.60\ a_B$ in confinement length and $0.15\ E_H$ in continuum threshold energy.

The simultaneous variation of confinement length $\mathscr{L}_L$ and continuum threshold energy D_L in the capturing quantum dot of the underlying potential presents a generalisation of the discussion on the quantum size effect of ICEC for a fixed continuum threshold parameter D_L. The variation of eigenenergies E_i of the confinement potential with respect to the parameter pair $(\mathscr{L}_L, D_L)$ is therefore illustrated in Figure 12 (b) for the case of a distance of $\mathscr{R} = 6\ a_B$ between the centres of the two quantum confinements. Within the investigated domain, an electron will be able to find between two and four eigenstates in the confinement potential illustrated by the four surfaces between energy values of 0 and $-0.9\ E_H$. Shown as diabatic energy surfaces, the ground state of the potential is primarily constituted by the state L_0 bound to the left quantum dot but approaches the eigenenergy of the right bound state R_0 in the lower third of the third quadrant in $(\mathscr{L}_L, D_L)$. At this point, any higher eigenstate has already been expelled from the confinement potential by an unfavourably narrow and energetically shallow left quantum dot. The energy crossing between L_0 and R_0 is approximately situated on the line spanned between the points of $(\mathscr{L}_L, D_L) = (2.6 a_B, 0.40 E_H)$ and $(\mathscr{L}_L, D_L) = (1.8 a_B, 0.48 E_H)$ indicated as solid ochre-coloured contour line of constant eigenenergy on the surface and on the bottom grid of Figure 12 (b).

As the right parameters of the right quantum dot remain unchanged during this study, the eigenenergy of the right-bound eigenstate R_0 will remain constant over large parts of the scanned domain as long as the left bound eigenstates are sufficiently separated in energy and localised distinctly thanks to narrow enough quantum confinements. Due to that constant nature over most of the domain, the state R_0 appears as orange plane making up most of the first excited state in Figure 12 (b) which shows only few contour lines marking the edges of energy crossings with L_0 and L_1. Due to the diabatic representation in Figure 12 (b), the energy ordered surfaces depicted avoid the crossing while the degerate states mix to form the eigenstate at these points. In the upper third, the energy crossing of R_0 with L_1 coincides incidentally with the beginning of noticeable effects of the parameter variation on the right-bound state itself. Marked by the unusually straight yellow contour line marking a constant eigenenergy of $E_i = -250 \times 10^{-3}\ E_H$ from coordinates $(\mathscr{L}_L, D_L) = (2.8a_B, 1.10E_H)$ to $(\mathscr{L}_L, D_L) = (4.7a_B, 0.44E_H)$. Ranging between a degeneracy with L_0 around $-211 \times 10^{-3}\ E_H$ and a minimum of $\min_{\mathscr{L}_L, D_L} E_{R_0} = -312 \times 10^{-3}\ E_H$ at parameters $(\mathscr{L}_L, D_L) = (4.7a_B, 1.10E_H)$, the state R_0 has an average energy of $\bar{E}_{R_0} = -226.2 \times 10^{-3}\ E_H$ over the investigated domain.

The left-bound eigenstate L_0 ranges from $\max_{\mathscr{L}_L, D_L} E_{L_0} = -157 \times 10^{-3}\ E_H$ at parameters $(\mathscr{L}_L, D_L) = (1.8a_B, 0.40E_H)$ where it exceeds the eigenenergy of R_0 down to $\min_{\mathscr{L}_L, D_L} E_{L_0} = -895 \times 10^{-3}\ E_H$ at $(\mathscr{L}_L, D_L) = (4.1a_B, 1.10E_H)$, the opposite corner of the domain over which it thus uniformly decreases with increasing length $\mathscr{L}_L$ and with increasing continuum threshold D_L. The average eigenenergy arrives therefore at $\bar{E}_{L_0} = -466 \times 10^{-3}\ E_H$.

The excited state L_1 only provides a valid localised eigenstate for part of the investigated domain. The lines of constant energy show a distinctly steeper slope $\Delta D_L / \Delta \mathscr{L}_L$ than the contour lines for L_0. Both of them are negative. The limiting solution of $E_{L_1} \approx 0$ is indicated in Figure 12 (b) by the blue contour line passing from coordinates $(\mathscr{L}_L, D_L) = (1.83a_B, 0.89E_H)$ in the background to $(\mathscr{L}_L, D_L) = (2.96a_B, 0.40E_H)$ in the foreground. There the energy surface is setting on with yellow colouring on top of the second lowest representing the R_0 state at that point. The energy of state L_1 then decreases uniformly with increasing confinement length $\mathscr{L}_L$ and continuum threshold D_L, crosses the energy of R_0 and reaches its minimal energy of $\min_{\mathscr{L}_L, D_L} E_{R_0} = -524 \times 10^{-3}\ E_H$ at the corner $(\mathscr{L}_L, D_L) = (4.7a_B, 1.10E_H)$ of the investigated domain. The sample average thus measures $\bar{E}_{L_1} = -105 \times 10^{-3} E_H$.

A third excited state L_2 is present for some part of the parameter domain towards large confinement lengths $\mathscr{L}_L$ and continuum threshold energies D_L but falls mainly into the same region as the energy crossing of L_1 with R_0. Indicated by dashed black line from parameters $(\mathscr{L}_L, D_L) = (3.09a_B, 1.09E_H)$ to $(\mathscr{L}_L, D_L) = (4.47a_B, 0.58E_H)$, the eigenenergies decrease uniformly with increasing $\mathscr{L}_L$ and D_L to a minimum of $\min_{\mathscr{L}_L, D_L} E_{L_2} = -182 \times 10^{-3} E_H$ at the far corner of the domain at $(\mathscr{L}_L, D_L) = (4.7a_B, 1.10E_H)$. It thus covers about 11 % of the domain and reaches an average energy of $\bar{E}_{L_2} = -43 \times 10^{-3} E_H$. Moreover, the far corner of the domain also sees the onset of a fourth excited level L_3 which, however, does not provide an energy surface within the domain of parameters.

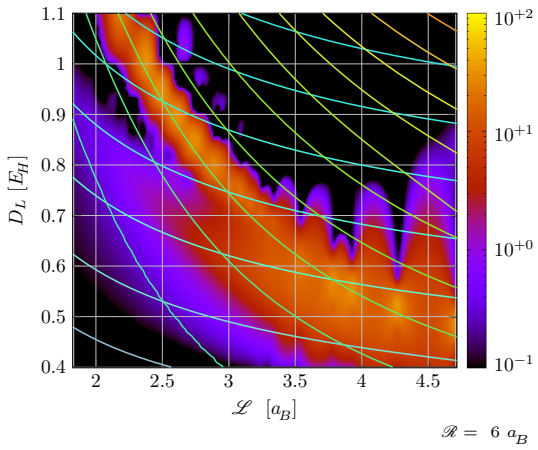

Figure 13: The maximal efficiency of interatomic coulombic electron capture in a pair of quantum confinements embedded in a nanowire as function of acceptor length $\mathscr{L}_L$ and its confinement strength D_L at centre-to-centre distance $\mathscr{R} = 6\ a_B$. Top view onto the landscape of the ICEC efficiency depicted in Figure 12 (a) which follows in trend the overlying contour lines of constant acceptor eigenenergy L_0 in shades of blue crossed by contour liness of eigenenergy L_1 in green to yellow which were presented and discussed with respect to Figure 12 (b).

In order to investigate a possible correlation between the trends in the maximum over energy of the ICEC probability $\max_E P^+_{L_0}$ shown in Figure 12 (a) and trends in single-electronic eigenenergies E_i discussed with respect to Figure 12 (b) which each are functions of the varied potential parameters $(\mathscr{L}_L, D_L)$, the top view onto the map of ICEC probability is presented with overlaying lines of constant eigenenergies E_{L_0} and E_{L_1} in Figure 13 for the distance of $\mathscr{R} = 6\ a_B$ between both quantum-dot centres. The ICEC probability is presented in logarithmic colouring and has been interpolated between the quantum-mechanically computed points of confinement length $\mathscr{L}_L$ and continuum threshold energy D_L. A bright yellow colour represents the maximal ICEC probability of 100 %. It iridesces in shade to arrive at an orange colour for a probability of 10 %. Then it transforms to red below 5 % and ranges through a fuchsia colour for a probability of 2% down to 1 % before fading to black for ICEC probabilities below 0.1%.

As a general trend, regions of comparable ICEC probability present a negative slope $\Delta D_L / \Delta \mathscr{L}_L$ on the map with respect to confinement parameters of capture length $\mathscr{L}_L$ and continuum threshold energy D_L. For confinement lengths below $\mathscr{L}_L = 2\ a_B$, the ICEC probability map presents a single broad strand which is emerging from the lower edge of the domain with length $\mathscr{L}_L = 1.83\ a_B$ at continuum thresholds of the confinement potential between $D_L \approx 1.0\ E_H$ and $D_L \approx 0.6\ E_H$ showing a small but non-vanishing ICEC probability between 0.09 % and 0.26 %. From a confinement length of $\mathscr{L}_L = 2\ a_B$ to $\mathscr{L}_L = 2.5\ a_B$ there appear two separate branches in the probability map which merge above $\mathscr{L}_L = 2.5\ a_B$. The previous

branch which arose from lower lengths $\mathscr{L}_L$ increases in probability with increasing confinement length and arrives at $P^+_{L_0} = 1.64$ % for a continuum threshold of $D_L = 0.72\ E_H$. Its negative slope $\Delta D_L/\Delta\mathscr{L}_L$ has brought it down to lower threshold energies between $D_L \approx 0.48\ E_H$ and $D_L \approx 0.81\ E_H$. An upper branch with respect to parameter D_L emerges from the upper edge on the map at $D_L = 1.10\ E_H$ which offers a larger ICEC probability above 30 % at length $\mathscr{L}_L = 2.5\ a_B$ but is narrower in D_L too such that it its distribution in D_L decreases to 1.5 % probability between $D_L = 0.85\ E_H$ and $D_L = 1.00\ E_H$. This branch provides the prominent ridge of high probability discussed with respect to Figure 12 (a) and evolves across the $(\mathscr{L}_L, D_L)$ parameter map with a steeper negative slope from its onset with 20.06 % probability at $(\mathscr{L}_L, D_L) = (2.16a_B, 1.10E_H)$ to $(\mathscr{L}_L, D_L) = (2.5a_B, 0.95E_H)$ with an ICEC probability of 31.28 %. In terms of confinement length, the upper branch spans between 0.38 a_B at $D_L = 1.00\ E_H$ and $0.45a_B$ at $D_L = 0.90\ E_H$.

Over the interval of confinement lengths $\mathscr{L}_L \in (2.5a_B, 3.0a_B)$, the two branches both broaden with respect to their width in D_L and gradually merge. The lower branch increases in probability to 6.61 % at $(\mathscr{L}_L, D_L) = (3.0a_B, 0.61E_H)$. Simultaneously, the upper branch decreases in probability to 17.48 % at $(\mathscr{L}_L, D_L) = (3.0a_B, 0.75E_H)$ but remains dominant. The probability distribution edge toward higher D_L moves further down with increasing lengths $\mathscr{L}_L$ such that at $\mathscr{L}_L = 3.54\ a_B$, the edge of 0.5 % probability is found at $D_L = 0.69\ E_H$. The overall probability-averaged position in parameter space is situated here at $(\mathscr{L}_L, D_L) = (3.21a_B, 0.67E_H)$.

For confinement lengths between $\mathscr{L}_L = 3.5\ a_B$ and $\mathscr{L}_L = 4.0\ a_B$, the probability regains strength measuring 30.88 % at $(\mathscr{L}_L, D_L) = (3.92a_B, 0.55E_H)$ while the distribution's 0.5%-edge moves further down to $D_L = 0.62\ E_H$ at length $\mathscr{L}_L = 3.92\ a_B$. Simultaneously, this edge shows more pronounced oscillations in D_L with increasing $\mathscr{L}_L$ which are partially introduced by the interpolation between available numerical grid points on the map but also reflects the fact that the left-localised eigenstates decrease in eigenenergy to larger negative values and increase in number towards higher $\mathscr{L}_L$ and D_L. Above a confinement length of $\mathscr{L}_L$, the oscillations of the probability edge toward higher D_L oscillates increasingly and gains in width to reach above $D_L = 0.95\ E_H$ while irregularities appear to manifest in the spacing between the overlaying contour lines indicating the energy crossing of L_1 with R_0 which moves down in D_L with increasing $\mathscr{L}_L$.

Overlaying the colour-graded ICEC probability map in Figure 13, the contour lines of constant eigenenergy E_{L_0} are presented in steps of $-0.10\ E_H$ with increasing continuum threshold D_L whereas the contour lines of constant E_{L_1} intercept those and represent eigenenergies in steps of $-0.05\ E_H$ with increasing D_L. Moving along an energy surface while keeping the energy value constant results in a family of curves with parameter D_L becoming a function of the independent parameter $\mathscr{L}_L$. Along the D_L axis at confinement length $\mathscr{L}_L = 1.8\ a_B$, the lowest contour line of constant eigenenergy $E_{L_0} = -0.20\ E_H$ starts at $D_L = 0.48\ E_H$ as solid grey-cyan line uniformly decreasing in D_L with increasing length $\mathscr{L}_L$. The next contour line represents an eigenenergy of $E_{L_0} = -0.30\ E_H$ and is beginning to appear along the

D_L-axis at $D_L = 0.62\ E_H$. Providing a constant eigenenergy for the state L_0 by decreasing uniformly in D_L with increasing $\mathscr{L}_L$, this contour line spreads over the entire domain of confinement lengths and hits the edge of $\mathscr{L} = 4.7\ a_B$ at continuum threshold $D_L = 0.41\ E_H$. Between these two contour lines, L_0 has passed the eigenenergy of R_0 which started out with $E_{R_0} = -224.0 \times 10^{-3} E_H$ in the corner of $(\mathscr{L}_L, D_L) = (1.8a_B, 0.40E_H)$ where the left-bound state had its maximum over the parameter domain of $E_{L_0} = -156.9 \times 10^{-3}\ E_H$. In line with this observation, it was recently shown that a part of this edge in the probability distribution at low $\mathscr{L}_L$ and low D_L is in fact following the curve of degeneracy where $E_{L_0} = E_{R_0}$.[64] The next contour lines of constant eigenenergy $E_{L_0} = -0.40\ E_H$, $E_{L_0} = -0.50\ E_H$ and $E_{L_0} = -0.60\ E_H$ appear parallel to the previous line along the abscissa at increasing D_L which are $D_L = 0.78\ E_H$, $D_L = 0.92\ E_H$ and $D_L = 1.06\ E_H$, respectively. Moreover, two additional contour lines of constant energy $E_{L_0} = -0.70\ E_H$ and $E_{L_0} = -0.80\ E_H$ appear from the upper border of the domain at $D_L = 1.10\ E_H$ at confinement lengths of respectively $\mathscr{L}_L = 2.22\ a_B$ and $\mathscr{L}_L = 3.09\ a_B$. For reasons of visibility, the contour lines of E_{L_0} are illustrated with a slight colour gradient with decreasing energy from bluish grey at $E_{L_0} = -0.20\ E_H$ towards cyan colour with decreasing energy down to $E_{L_0} = -0.80\ E_H$. Along the axis of D_L at confinement length $\mathscr{L}_L = 1.8\ a_B$, a line manifests at $D_L = 0.89\ E_H$ which distinctly crosses the otherwise parallel lines of constant E_{L_0} on its passage through increasing $\mathscr{L}_L$ and decreasing D_L until it reaches the lower border at $(\mathscr{L}_L, D_L) = (2.96a_B, 0.40E_H)$.

The lower branch of high ICEC probability is primarily situated between then L_0-contour lines of $E_{L_0} = -0.30\ E_H$ and $E_{L_0} = -0.50\ E_H$ which also describes the merged distribution to some extent. It shows a sharper onset of probability along $E_{L_0} = -0.50\ E_H$ visual by a more contrasted appearance of colouring against the black background as opposed to the smoother fading of colouring on the side of $E_{L_0} = -0.30\ E_H$. Simultaneously, fluctuations and oscillations at the edge of the probability distribution appear more pronounced around $E_{L_0} \approx -0.55\ E_H$ but less ragged around $E_{L_0} \approx -0.25\ E_H$. The highest probability along the D_L axis at $\mathscr{L}_L = 1.8\ a_B$ occurs at $D_L = 0.90\ E_H$ just between the L_0-contour of $-0.50\ E_H$ and the L_1-contour of $0.0\ E_H$. The maximal probability of the lower branch up to $\mathscr{L}_L$ appears to evolve on the line formed by this intersection to the intersection of the next lower lying contours of L_0 and L_1 where $E_{L_0} = -0.40\ E_H$ and $E_{L_1} = -0.05\ E_H$.

While the contours of L_0 appear to coincide with the general trend of the lower branch, the maximum of ICEC probability for a specific $\mathscr{L}_L$ seems to be additionally modified by contours of L_1 which also coincides with the upper branch and main ridge of high probability for $E_{L_1} = -0.10\ E_H$. Most contours of L_0 pass the entire range of $\mathscr{L}_L$ presented in Figure 13 which is thanks to the small slope $\Delta D_L / \Delta \mathscr{L}_L$ whereas all but one of the presented contours of L_1 pass from a domain edge of $\mathscr{L}_L$ to a perpendicular domain edge of D_L or vice versa due to their uniformly steeply decreasing in D_L with increasing $\mathscr{L}_L$. Descending from the upper border of $D_L = 1.10E_H$, the contour lines of constant energy of L_1 appear as $E_{L_1} = -0.05\ E_H$ at $\mathscr{L}_L = 1.93\ a_B$, as $E_{L_1} = -0.10\ E_H$ at $\mathscr{L}_L = 2.17\ a_B$, as $E_{L_1} = -0.15\ E_H$ at length $\mathscr{L}_L = 2.41\ a_B$ and so forth in steps of $-0.05\ E_H$ in energy. The next three contour lines start out as regular as the previous ones but their spacing deviates for lengths

above $\mathscr{L}_L = 3.9\ a_B$. This is induced by the energy crossing with R_0 which itself begins to decrease with increasing $\mathscr{L}_L$ and D_L.

The upper strand of significant ICEC probability is bound by the contour lines of L_1 of $E_{L_1} = -0.05\ E_H$ and $E_{L_1} = -0.15 E_H$ which also determine the trend of the probability above confinement length $\mathscr{L}_L = 3\ a_B$ where the upper branch merges with the lower one which follows the contour lines of L_0. The major trend of points of high ICEC probability discussed with respect to Figure 12 (a) visible on the top view onto the probability map by shades of bright orange to yellow thus follow the central contour of $E_{L_1} = -0.10\ E_H$ closely over the entire map. While the confidence interval of the upper branch in terms of eigenenergy of L_1 spans below $0.10\ E_H$. It broadens where the three L_1 contours overlap with the L_0 contour lines determining the lower branch confidence interval in terms of eigenenergy of L_0 to about $0.25 E_H$. As the two branches join, their respective trends merge too and broaden the probability distribution. Therefore, the boundary of 2 % probability within the lower branch follows closely to the adjoining L_1 level. As the L_1 contour lines descend with increasing $\mathscr{L}_L$, their spacing increases on the map. The broadening in the probability distribution appears to occur in line with the broadening of the L_1 contour line spacing. While the fluctuations in shape of the edge of the probability distribution to higher D_L increase with $\mathscr{L}_L$ and increasingly spread beyond the L_1 contour of $E_{L_1} = -0.15\ E_H$, they reconvene within this boundary at confinement lengths where local maxima appear in the probability. At the same time, the edge of the probability distribution fluctuates and broadens particularly near the region of energy crossing between L_1 with R_0 at confinement lengths above $\mathscr{L}_L = 3.9\ a_B$ and continuum threshold energies above $0.7\ E_H$.

While the description of ICEC probability as well as eigenenergies of the capturing potential in terms of the parameters of the used confinement potential appear complicated and strongly dependent on the definition of the modelling potential itself, a general correspondence between trends in the eigenenergies and trends in the ICEC probability would offer a way to estimates beyond the particular model used. It was thus possible in the related recent publication of Pont et al. [64] to propose several limiting conditions estimated from single-electronic quantities which mark boundaries of the ICEC probability. If the ICEC probability can be mapped successfully in terms of the eigenenergies, as it appears suggestively from Figure 13, this may simplify analysis and discussion of the efficiency of ICEC in a particular system independently from the real or modelled underlying confinement potential and its various available parameters. To this goal, the preliminary hypothesis shall be tested qualitatively against selected larger quantum-dot distances $\mathscr{R}$ although a quantitative representation resolved in terms of (E_{L_0}, E_{L_1}) is complicated by the curvilinear nature of the contour lines on the numerically computed rectilinear grid of parameters $(\mathscr{L}_L, D_L)$. For six different quantum-dot-distances $\mathscr{R}$ increasing in increments of $1\ a_B$, Figure 14 shows therefore the maximum with respect to energy of the ICEC probability in transmission direction $\max_E P^+_{L_0}$ as function of confinement parameters of capture length $\mathscr{L}_L$ and continuum threshold energy D_L in comparison to curves of constant eigenenergy E_{L_0} and E_{L_1} as functions of the same confinement parameters.

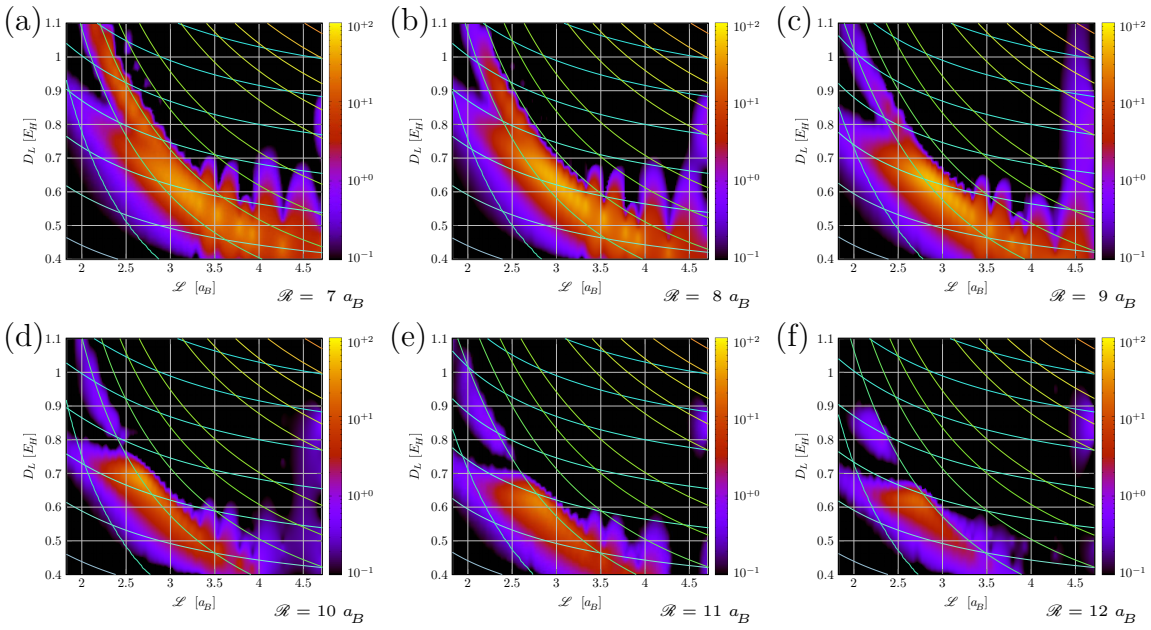

Figure 14: The maximal efficiency of interatomic coulombic electron capture in a pair of quantum confinements as function of acceptor size and potential strength in depends on distance but follows the contours of acceptor eigenenergy L_0 crossed by eigenenergy L_1.

A distance of $\mathscr{R} = 7.0\ a_B$ between the centres of the two quantum confinements is shown in Figure 14 (a). As the distance increases with respect to Figure 12, the perturbative influence arising from the vicinity of the two quantum dots on eigenstates of higher energy reduces slightly. This has an effect primarily on R_0 and L_1 and affects the energy surfaces particularly in regions of higher parameters $\mathscr{L}_L$ and D_L where the right-bound level R_0 was increasingly perturbed and decreased in energy E_{R_0} for the distance $\mathscr{R} = 6.0\ a_B$. At $\mathscr{R} = 7\ a_B$, the right-bound state R_0 varies therefore less in energy. Over the dominant diagonal of the parameter domain, it thus varies from an eigenenergy of $E_{R_0} = -237.5 \times 10^{-3}\ E_H$ at $(\mathscr{L}_L, D_L) = (1.8a_B, 0.40E_H)$ to an energy of $E_{R_0} = -277.3 \times 10^{-3}\ E_H$ at $(\mathscr{L}_L, D_L) = (4.7a_B, 1.10E_H)$ at the opposite corner of the domain. In average, the state R_0 has an energy of $E_{R_0} = -239.2 \times 10^{-3}\ E_H$. The left-bound state L_1 remains mainly unchanged in maxima and average but the higher states L_2 and L_3 which appear towards large $\mathscr{L}_L$ and D_L move close to R_0 by up to $25 \times 10^{-3}\ E_H$. This changes the progression of contour lines with respect to parameters $(\mathscr{L}_L, D_L)$ slightly. In particular, the energy crossing of L_1 with R_0 now appears as consistent additional spacing between the contour lines of L_1 whereas it had appeared to repel the contour lines for $\mathscr{R} = 6a_B$ between $E_{L_1} = -0.2\ E_H$ and $E_{L_1} = -0.3\ E_H$ only for confinement lengths above $\mathscr{L}_L = 0.39\ a_B$.

The probability map appears despite these changes qualitatively similar to Figure 13 but the regions of significant ICEC probability have narrowed to cover less area in parameter space while becoming on average more efficient within those re-

gions. In fact, the maximal probability on this map reaches 36.74 % at parameters $(\mathscr{L}_L, D_L) = (3.33a_B, 0.57E_H)$ which is roughly 2 % more effective here than the maximum for $\mathscr{R} = 6\ a_B$. Simultaneously, the average ICEC probability over the map has increased to 3.92 % with a probability-weighted average position of $(\mathscr{L}_L, D_L) = (3.03a_B, 0.64E_H)$. The sample standard deviation in ICEC probability has grown to 7.36 % indicating an improved efficiency over the regions of significantly large probability. Simultaneously, the probability-weighted standard deviation in the parameter space has shrunk to 0.42 a_B in confinement length and $99 \times 10^{-3}\ E_H$ in continuum threshold energy which speaks for an overall smaller area on the map in parameter space $(\mathscr{L}_L, D_L)$ covered by the probability distribution.

The probability map consists of one major area which is fenced in towards larger $\mathscr{L}_L$ and larger D_L by the overlapping contours of $E_{L_1} \leq -125 \times 10^{-3}\ E_H$ and $E_{L_0} \leq -0.52\ E_H$, towards lower $\mathscr{L}_L$ and higher D_L by the overlapping contours of $E_{L_1} > -0.05\ E_H$ and $E_{L_0} \leq -0.52\ E_H$, and is fading towards lower L_L and lower D_L where $E_{L_0} \approx E_{R_0}$ and beyond $E_{L_1} = 0$. Marginal increases in probability appear outside this general area at intervals along the contour line of $E_{L_1} = -0.15\ E_H$ and at the edge of $\mathscr{L}_L = 4.7\ a_B$ between $D_L = 0.7\ E_H$ and $D_L = 0.9\ E_H$ but these remain below 1 % probability. The two branches of ICEC probability remain therefore visible for lower $\mathscr{L}_L$ consistent with the previous distance $\mathscr{R} = 6$. Similar to the previous, the probability forms a major ridge of high probability along the upper branch and down along the contour lines of L_1 which decreases briefly in strength when merging with the lower branch which then fluctuates strongly in its edge when passing beyond the L_1 branch to higher $\mathscr{L}_L$. However, intervals in energies of L_0 and L_1 have reduced in their respective sizes. The confidence interval in E_{L_1} is now only about 0.07 E_H and the confidence interval in E_{L_0} spans about 0.2 E_H. Local maxima in probability at constant confinement lengths $\mathscr{L}_L$ occur along the long diagonals drawn by the curvilinear intersections of the contours of L_0 with L_1 from the intersection of $E_{L_0} = -0.5\ E_H$ with $E_{L_1} = 0$ through the cross of $E_{L_0} = -0.4\ E_H$ with $E_{L_1} = -0.05\ E_H$ towards the intersection of $E_{L_0} = -0.30\ E_H$ with $E_{L_1} = -0.10\ E_H$. This agrees with the observations for Figure 13.

At distance $\mathscr{R} = 8\ a_B$, the parameter space covered by the ICEC probability reduces further while the average efficiency increases with respect to $\mathscr{R} = 7\ a_B$. The maximum probability encountered here is 47.65 % at confinement length $\mathscr{L}_L = 3.02a_B$ and continuum threshold $D_L = 0.63\ E_H$. Averaged over the sampled domain, the mean probability reaches 4.75 % with an increased sample standard deviation of 9.65 %. At the same time, the probability-weighted standard deviation in parameter space decreases to 0.38 a_B in confinement length $\mathscr{L}_L$ and to $84 \times 10^{-3} E_H$ in threshold D_L The probability map remains bound toward smaller $\mathscr{L}_L$ and D_L by the condition of $E_{L_0} \approx E_{R_0}$ and fades past $E_{L_1} = 0$. The boundaries from above have moved closer though such that the probability is slowly being pushed out. Toward larger $\mathscr{L}_L$ and larger D_L, the simultaneous fulfilment of the conditions of $E_{L_1} > -0.10\ E_H$ and $E_{L_0} > -0.48\ E_H$ appears to limit any probability contributions above 0.8 %. However, larger confinement lengths $\mathscr{L}_L > 4.2\ a_B$ allow a spreading of low probability around 0.5 % down to $E_{L_0} = -0.70\ E_H$. At high threshold D_L and low confinement $\mathscr{L}_L$, the probability appears in the known two branches confined

by $E_{L_0} > -0.52\ E_H$ and $E_{L_1} < 0.04\ E_H$. As the area covered by the upper branch shrinks, the local probability appears to retract slightly towards the area where both branches merge.

The probability density has been pushed further to areas of higher energies in L_0 and L_1 in Figure 14 (c) representing a distance of $\mathscr{R} = 9\ a_B$ and retracts further away from a band of maxima toward a single larger maximum but retains the qualitative shape of two joining branches. Its maximum ICEC probability of 55.18 % represents thereby the largest maximum over the shown distances from $\mathscr{R} = 6\ a_B$ to $\mathscr{R} = 12\ a_B$. The position of the maximum at $(\mathscr{L}_L, D_L) = (2.89a_B, 0.63E_H)$ has moved to yet smaller confinement length where the left-bound state measure an eigenenergy of $E_{L_0} = -400.1 \times 10^{-3}\ E_H$ and $E_{L_1} = -56.9 \times 10^{-3}\ E_H$. The average probability of 4.43 % has decreased in comparison to the result for $\mathscr{R} = 8\ E_H$ while the sample standard deviation has increased to 9.71 % statistically distributed over a smaller area in parameter space which reduces the probability-weighted standard deviation to 0.34 a_B in confinement length and $72 \times 10^{-3}\ E_H$ in continuum threshold D_L. This alludes at a larger range of probability covered by a smaller domain in $(\mathscr{L}_L, D_L)$. The standard deviation in probability is the highest for the investigated distances $\mathscr{R}$ whereas the probability-weighted standard deviation in $\mathscr{L}_L$ and D_L proves to be smallest at the same time.

Taking into account that the R_0 level has slightly shifted towards an average of $\bar{E}_{R_0} = -222 \times 10^{-3}\ E_H$, the probability map remains bound towards small $\mathscr{L}_L$ and D_L by the energy crossing of L_0 with L_1. Towards larger D_L and larger $\mathscr{L}_L$, the bounding conditions have moved to $E_{L_1} > -0.08\ E_H$ and $E_{L_0} > -0.45\ E_H$ but are overcome for confinement lengths above $\mathscr{L}_L = 4.25\ a_B$ where it becomes possible to cover the entire domain in D_L with probability up to 0.97 %. The boundary between the two branches toward small $\mathscr{L}_L$ and higher D_L has are given by $E_{L_0} < -0.47\ E_H$ and $E_{L_1} > -0.04\ E_H$ which is shifted slightly and condenses the probability distribution to less area. As a result, the upper branch of the probability map has lost its dominance seen in the case of $\mathscr{R} = 6\ a_B$ and barely exceeds 2 % probability which concentrates towards the edge of the lower branch.

The quantum-dot distance of $\mathscr{R} = 10\ a_B$ becomes generally less favourable where regions of higher probability concentrate more locally. As the boundary from larger $\mathscr{L}_L$ and D_L pushes further towards the opposing bounds, the probability reduces on the remaining available area. The maximum of only 36.36 % therefore localises within then merging two branches at $(\mathscr{L}_L, D_L) = (2.67a_B, 0.68E_H)$. The average probability reaches at 2.33 % only half of the value for $\mathscr{R} = 9\ a_B$. Simultaneously, the standard deviation reduces to 5.48 % and concentrates to a probability-weighted standard deviation of 0.29 a_B in confinement length $\mathscr{L}_L$ and $67 \times 10^{-3}\ E_H$ in continuum threshold energy D_L.

Bounding the probability distribution towards larger $\mathscr{L}_L$ and larger D_L are the conditions of $E_{L_1} > -0.07\ E_H$ and $E_{L_0} > -0.42\ E_H$. For larger confinement lengths above $\mathscr{L}_L = 4.2\ a_B$, the probability persists to reach further into the domain of D_L up to $E_{L_0} = -0.70\ E_H$ but barely reaches 0.67 %. The upper branch in the distribution

seen at smaller distances is still present, but faded in probability to a local maximum of 0.76 % at parameters $(\mathscr{L}_L, D_L) = (2.32a_B, 0.85E_H)$. The previously observed reduction in probability at the point of merging with the lower branch begins to manifest as gap between the two as they are both weakened. The long tail at low thresholds D_L to increasing lengths $\mathscr{L}_L$ which had pertained a ridge of higher probability throughout the variations of $\mathscr{R}$ has decreased below 1 % and is fading. Towards lower $\mathscr{L}_L$ and higher D_L, the probability map is bound by the condition of $E_{L_1} < -25 \times 10^{-3}\ E_H$ defining the upper branch but persists to hold its probability at the intersection of both branches such that the lower branch is bound by $E_{L_0} > -0.48\ E_H$ but fades quickly before that outside the intersection of both branches. At low lengths $\mathscr{L}_L$ and threshold energies D_L, the probability map remains bound by the energy crossing of L_0 with R_0 and is fading beyond the spawning line of L_1 where $E_{L_1} = 0$.

Gradually expelled, the ICEC probability reaches only a maximum of 26.36 % as the boundaries approach each other and diminish the coverable domain in parameter space for a quantum-dot distance of $\mathscr{R} = 11\ a_B$ as depicted in Figure 14 (e). Ten percent lower in its maximal probability than for distance $\mathscr{R} = 10\ a_B$, the average probability over the domain has reduced to 1.64 % and its probability-weighted position is moving to lower D_L arriving at an average position of $(\mathscr{L}_L, D_L) = (2.78a_B, 0.59E_H)$ in parameter space. The standard deviation in probability has diminished to 3.91 % but retained the probability-weighted standard deviation of 0.32 a_B in length $\mathscr{L}_L$ and of $66 \times 10^{-3}\ E_H$ in continuum threshold D_L.

At this setup, the probability distribution barely reaches beyond the first contour line of L_1 but finds slightly more support by the intersection with the lower branch such that the distribution as a whole is limited by $E_{L_1} > -0.07\ E_H$. Apart from the intersection, the lower branch only touches up to $E_{L_0} = -0.40\ E_H$ but reaches up to $-0.42\ E_H$ along the direction of the upper branch. Bound by the energy crossing of L_0 with R_0 at small $\mathscr{L}_L$ and D_L, the distribution thus barely covers a third of the parameter domain with probabilities above 0.1 %. The tail of the probability distribution toward higher confinement lengths dies down at $\mathscr{L}_L = 4.25\ a_B$ but shows a marginal revival of probability up to 0.47 % at $\mathscr{L}_L = 4.71\ a_B$. Similarly, a region of up to 0.92 % probability has remained within $E_{L_0} = -0.60\ E_H$ and $-0.70\ E_H$. At this distance $\mathscr{R}$, this small region of probability is possibly arising from favourable energetic conditions from higher lying states L_2 and L_3 which both present themselves at this border of the domain.

Eventually, the probability distribution diminishes quickly toward $\mathscr{R} = 12\ a_B$ such that the maximum is ten percent less in probability than for $\mathscr{R} = 11\ a_B$ and covers only a fifth of the investigated domain by three small main regions of which only one exceeds 1 % probability. The maximum of 15.65 % has moved yet again to lower confinement length and is positioned on the map at $(\mathscr{L}_L, D_L) = (2.67a_B, 0.62E_H)$. The average probability has shrunk below one percent to only 0.76 % with a standard deviation of 2.02 % yet more localised in its position to probability-weighted standard deviations of 0.31 a_B in confinement length $\mathscr{L}_L$ and of $60 \times 10^{-3}\ E_H$ in continuum threshold energy D_L.

The upper branch has reduced to a small region of maximum 0.84 % at $(\mathscr{L}_L, D_L) = (2.32a_B, 0.80E_H)$ which appears to experience a hard boundary at $E_{L_1} = -0.05\ E_H$. At the same time, the small region at large confinement lengths $\mathscr{L}_L > 4.5\ a_B$ has persisted and reaches a maximum of 1.28 % probability at $(\mathscr{L}_L, D_L) = (4.71a_B, 0.85E_H)$. The lower branch has retracted and is bound by $E_{L_0} > -0.41\ E_H$ which shows slightly more support where the conditions of both branches merge. The region of higher probability, however, follows the bounding limit of the upper branch closely such that the tail towards higher confinement lengths vanishes fades quickly. The probability distribution is thus mainly confined between the two contour lines of L_1 of energies between $E_{L_1} = 0$ and $E_{L_1} = -0.05\ E_H$ and between the two contour lines of L_0 of energies between $E_{L_0} = -0.4\ E_H$ and $E_{L_0} = -0.30\ E_H$ but reaches along the contour lines of L_1 down to the energy crossing of L_0 with R_0.

In summary over the investigated distances from $\mathscr{R} = 6\ a_B$ depicted in Figure 13 to $\mathscr{R} = 12\ a_B$ depicted in Figure 14 (f), the ICEC probability mapped logarithmically as function of the parameters $(\mathscr{L}_L, D_L)$ shows two major branches for small confinement lengths $\mathscr{L}_L$ which merge towards larger $\mathscr{L}_L$ and smaller D_L. It has been shown that the upper branch of the main body of the probability map has followed the contours of lines of constant eigenenergy of the state L_1 but its edge toward higher $\mathscr{L}_L$ shifted two contour lines of L_1 from $E_{L_1} = -0.15\ E_H$ to $E_{L_1} = -0.05\ E_H$. At the same time, the shape of the lower branch at low $\mathscr{L}_L$ appeared to follow the contours of constant eigenenergy of state L_0, as did the shape of the probability map for higher $\mathscr{L}_L$ beyond the merging of the two branches despite showing increasing oscillations in shape with increasing $\mathscr{L}_L$. This edge toward higher D_L has retracted by approximately one contour line from $E_{L_0} = -0.52\ E_H$ at $\mathscr{R} = 6\ a_B$ to $E_{L_0} = -0.4\ E_H$ at distance $\mathscr{R} = 12\ a_B$. At the same time, the boundary of the probability distribution from below at small $\mathscr{L}_L$ and D_L remains intact and varies little. In line with the arguments presented in Pont et al. [64], part of the bounding shape coincides here with the energy crossing of the capturing state L_0 with the initial state R_0. The probability density appeared to fade here beyond the line of vanishing energy level L_1.

At large $\mathscr{L}_L$ above 4.25 a_B, the initial state R_0 varies significantly from its average value over the remaining domain. Simultaneously, two energy levels are present below R_0 in this region while two excited levels present themselves above R_0. This allows the ICEC probability in this region of $\mathscr{L}_L > 4.25\ a_B$ to spread from the main body of its distribution to higher D_L where it collates at distances $\mathscr{R} = 11\ a_B$ and 12 a_B while detaching itself from the main region at lower D_L. In logarithmic scaling from 0.2 % to 100 %, the ICEC probability covered approximately 60 % of the investigated domain in parameters $\mathscr{L}_L$ and D_L for the distance of $\mathscr{R} = 6\ a_B$ in a fairly uniform distribution of ICEC probability along the contour line of L_1 at energy $E_{L_1} = -0.1\ E_H$ and large regions above around and above 30 % ICEC probability. As the boundaries move with increasing quantum dot distance, the probability map has evolved into an uneven distribution covering 50 % of the domain for the distance $\mathscr{R} = 9\ a_B$ and appears to follow the contour line of $E_{L_1} = -0.05\ E_H$ but has concentrated into a single maximum exceeding 55 % ICEC probability which is the highest found for the investigated parameter domain. With increasing distance, the boundaries of the logarithmic ICEC probability contract further such that for

$\mathscr{R} = 12\ a_B$ only 20 % of the domain are covered by the probability map which has by now localised into three small regions with a mean below 1 % ICEC probability and which appears to find a boundary of favourable conditions along the contour line of $E_{L_1} = -0.05\ E_H$. While it is clear that the distance between the two quantum-dots $\mathscr{R}$ gives rise to the changes in the probability distribution which appears to follow the trends of the contours of constant eigenenergy in L_0 and L_1, the relation between variation of $\mathscr{R}$ and shift in eigenenergies is not yet apparent.

6.3 Conclusion

Throughout this chapter, the electron dynamics of interatomic coulombic electron capture have been investigated numerically for the quasi-one-dimensional system of two quantum confinements embedded longitudinally within a nanowire. While the numerical model has been established and used with the MCTDH approach since (2011) for numerical investigations of the dynamics of interatomic coulombic decay and has been adapted successfully in (2013) to model electronic scattering and interatomic coulombic electron capture,[3,72] it was possible to draw several conclusions in the current investigation which can inspire further comprehension of the dynamics governing ICEC and which proposes several hypotheses beyond the employed numerical model that may be employed in theory and experiment to guide future investigations.

Section 6.2.1 discussed the resolution of quantum flux into contributions measured in the direction of reflection and that of transmission in correlation with an occupation of various electronic bound states within the confinement region. In comparison with an additional computation of the dynamics of two independent electrons at same initial conditions, it was found that the transmission of electronic flux associated with interatomic coulombic electron capture is modified by the energy dependence of the transmission coefficient of the confinement potential itself. In addition to existing literature,[2,3,8,9] the quantum flux in reflection direction was analysed and discussed which showed that its spectrum differs from that of the transmitted flux. The spectrum of the ICEC-correlated flux density showed clear indications in either direction that two distinct subprocesses are active and can show differing spectral features at independent resonant energies.

As discussed recently,[2] interatomic coulombic electron capture may occur successfully on the one hand through a direct energy transfer on impact which will carry a modulated echo of the original spectrum of the incident electron, and can take place on the other hand through an energy conversion into potential Coulomb energy between the two electrons which allows capture into an intermediary state of simultaneous localisation of both electrons. A consecutive decay will offer a distinct spectral contribution to the ICEC-related flux density which carries the information of the particular resonant energy and decay width of the decaying state. It was found here, that the subprocesses can have different reflection and transmission coefficients thus appearing to contribute in different amounts to the overall ICEC flux depending on which emission direction is measured.

Section 6.2.2 advanced these findings over a range of varying capture sizes and showed that in either emission direction, the maximal flux density associated to ICEC is limited by a function of system energy. However, the individual flux density maximum moves along the system energy with increasing capture length as a result of the quantum size effect. The flux density in transmission direction proved to be dominant which supported the concentration on the emission in transmission direction found in the literature.[2,3,8,9,64] The envelope functions corresponding to the maximal ICEC flux density at a particular system energy showed a comparable rise toward their maximum value for both emission directions but differed in their decrease for larger energies. The spectrum of the transmissive flux density presented here a much broader range.

Eventually, Section 6.2.3 investigated the logarithmic ICEC probability and found that the narrow ridge of high probability formed a curved line when mapped against the domain of capturing length and continuum threshold which appeared to coincide with the contours of constant eigenenergy of the excited capture state L_1 and presented a second branch coinciding with trends of the contour lines for capturing ground state L_0. This conclusion was validated at different distances between the quantum confinement centres and it was found that the curvilinear behaviour with respect to the parameters of capture size and continuum threshold were retained. In a description by the respective eigenenergies of L_0 and L_1, the logarithmic ICEC probability could be expressed by an interval of eigenenergies and was strongest in the region where both intervals met. With increasing distance, the interval boundaries toward larger confinement lengths and those toward larger continuum thresholds shifted gradually toward lower parameters which corresponds with a shift toward higher eigenenergies. At the same time, the interval boundaries toward lower confinement lengths and lower continuum threshold parameters appeared persistent in their energetic value in L_0 and L_1 which roughly coincided with the degeneracy between capturing ground state L_0 and initially bound state R_0 for one and faded slowly beyond vanishing L_1. This results in a focus of both branches on less parameter space with increasing confinement distance. By this, the curvilinear ridge of high probability around 20 % to maximal 34.57 % at $\mathscr{R} = 6\ a_B$ focusses in one point and rises up to 55.18 % at distance $\mathscr{R} = 9\ a_B$ before decreasing in maximum and covered area in parameter space with further increasing distances. At the intersection between the two branches a reduced probability is visible for all distances which leads to a separation of both regions of probability distribution as it decreases generally with the reduced area. Large confinement lengths show some resilience to the general decrease in ICEC probability which has been attributed to be potentially due to the presence of an additional energy level L_3 energetically above initial state R_0 while also presenting an additional level L_1 below R_0. At the same time, this region shows a stronger change in eigenenergy of the initial state R_0 itself. Furthermore, the parallel has been drawn that two subprocesses were observed over the range confinement lengths which exerted a narrow-banded and a broad-banded spectrum in ICEC flux density whereas similarly, the two branches presented one with abroad energy range with respect to L_0 and one with a narrow energy range with respect to L_1.

In conclusion, the presented computational results proposed the hypotheses that a presentation of the logarithmic ICEC probability resolved in terms of eigenenergies of capturing states L_0 and L_1 will show a simpler and possibly model-independent description. These dependences strongly suggest to relate to the respective subprocesses of ICEC through direct inter-electronic impulse and of ICEC via interatomic coulombic decay. At the current stage, the particular relation between the bounding eigenenergies and the quantum dot distance remains unclear. Nevertheless, the interatomic coulombic electron capture appears predominantly optimised by a tuning of the single-electron energy levels independent on the employed confinement model or real potential.

7 Electron Capture in Ultracold Atoms

Proven to be a powerful and adaptable method to attack the question of electron dynamics of interatomic coulombic electron capture within the theoretically and experimentally flexible system of artificial atom-like confining potentials within a solid-state medium,[2,3,8,9,64] the model was transferred naturally in Section 5 of this work to encompass real ions in clouds assisting atoms. Trapped ultracold ions and atoms are a particularly intriguing research field for a prospective application of a generalized model to investigate ICEC dynamics. Offering a high experimental precision and quantum-mechanical yet macroscopic control over the reaction partners on the one hand, and nearly two centuries of experience in manipulation of electron rays through vacuum on the other hand, not at least from consumer electronics. The first time-resolved ICEC experiment appears at our tips in this field of research whereas the design of potential experimental set-ups seems evasive in other fields. Moreover, the same working principles that allow entrapment and manipulation of cold atoms and ions are being explores to produce beams of cold electrons at energies on the order of 1 meV, just above ionisation threshold.[119] Thus motivated to seize this opportunity to diversify the field of investigation of the electron dynamics of the interatomic coulombic electron capture, this chapter will present the first numerical implementation towards this goal.

In search for a valid starting point, several approximations have been made. Relying on the methodological approach which proved fruitful in constructively analysing the established solid-state systems involved in Section 6.2, insight shall be gathered on the portability of the model and on weaknesses of and benefits from the employed approximations. One of the challenges is the difference in orders of magnitude between the characteristic range of a Coulomb interaction and typical distances between trapped central ions and their surrounding atoms distributed in a macroscopic cloud. On the other hand, the number of available identical interaction partners is large and would be similarly reach the limit of computational feasibility. It has thus been proposed in Section 5.1 that these extremes may allow to numerically counteract each other in an averaged treatment in the spirit of an effective particle approach not dissimilar to the successful interpretations in the application to quantum dots. Freeing the assisting ultracold atom from a fixed distance $\mathscr{R}$ away from the electron-capturing ion to be distributed but bound by a macroscopic harmonic potential introduces in fact an effective nuclear degree of freedom into the

two-electron model to make it computationally more robust.

7.1 Computational Details

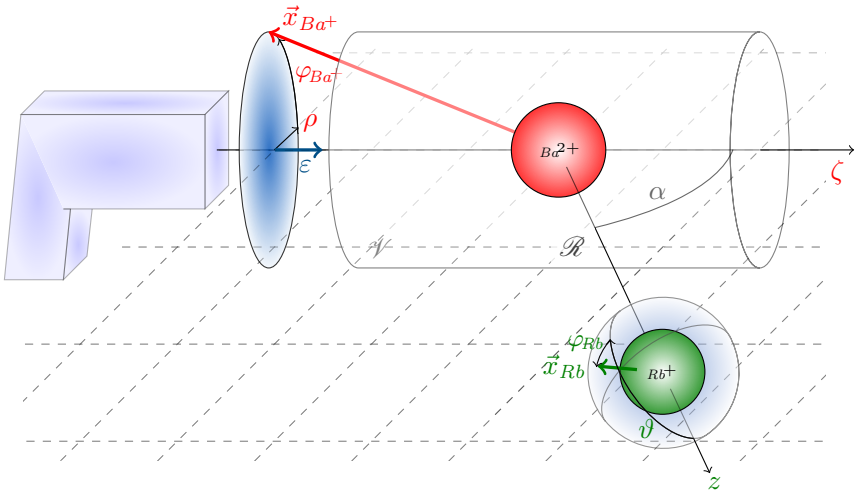

Figure 15: Schematic geometry and symmetries of an ICEC experiment with barium (II) under assistance of rubidium. An electron gun provides an electron density distribution with kinetic energy ε approaching a barium (II) cation. The incident electron has a position vector $\vec{x}_{Ba^+}$ with respect to the barium (II) cation and the distribution has a cylindrical symmetry with coordinates $(\zeta, \rho, \varphi_{Ba^+})$. A rubidium atom is situated at distance $\mathscr{R}$ from the barium ion and forms an angle α between the atom-atom axis and the axis cylinder axis of incident electron on barium. Rubidium's electron symmetry is best described by a spherical coordinate system with coordinates $(r, \vartheta, \varphi_{Rb})$ which is aligned with the atom-atom axis.

The electron coordinates of the free incident electron shall be given in cylindrical coordinates ζ along the cylinder axis, ρ along the transverse and φ_{Ba^+} along the angular direction. The kinetic energy operator of the incident electron on barium (II) can then be given by

$$\hat{T}_{Ba^+} = -\frac{\hbar^2}{2m}\left(\partial_\zeta{}^2 + \partial_\rho{}^2 + \rho^{-2}(\partial_{\varphi_{Ba^+}}{}^2 + \tfrac{1}{4})\right) . \tag{198}$$

The rubidium atom is situated at a distance $\mathscr{R}$ from the barium (II) cation in an angle α from the electron beam axis on barium. In spherical coordinates of radius r, polar angle ϑ with z axis along the atom-atom axis and azimuthal angle φ_{Rb}, the kinetic energy operator of the outermost valence electron bound to rubidium shall be

$$\hat{T}_{Rb} = -\frac{\hbar^2}{2m}\left(\partial_r{}^2 + r^{-2}\hat{\ell}^2_{(\vartheta,\varphi_{Rb})}\right) , \tag{197}$$

where $\hat{\ell}$ indicates the electronic angular momentum operator.

In this model, bound electrons below the 6s shell on barium and the 5s shell on rubidium shall be frozen and the effective binding potential for the remaining

outer-most rubidium electron and the incident electron on barium be given by[111,120]

$$V_k(r_k) = -\frac{Z_k}{r_k} + \frac{\alpha_k}{r_k^4}\left(1 - \exp\left[-\left(\frac{r_k}{\delta_k}\right)^2\right]\right)^2 + B_k \exp\left[-\left(\frac{r_k}{b_k}\right)^2\right] \tag{212}$$

with respective parameters of distance from the ion core r_k, effective core charge Z_k, dipole polarisability α_k, approximate core radius δ_k, and relativistic corrective parameters (B_k, b_k) which are in general dependent on the electronic angular momentum,[111] where k shall represent barium or rubidium. For simplicity, the dependence on the angular momentum is ignored in this study which is therefore considered to present a proof of principle. The respective parameters are chosen to describe the s shell and are summarized in Table 2 since these represent the ground state configurations for both species.

Considering the incident electron and frozen barium (II) cation as a subsystem with electrodynamic dipole $\vec{x}_{Ba^+} = (\zeta, \rho, \varphi_{Ba^+})$ and the outermost rubidium electron with frozen rubidium (I) cation as a second subsystem of electrodynamic dipole $\vec{x}_{Rb} = (r, \vartheta, \varphi_{Rb})$, the interaction potential between both subsystems shall be modelled by the dipole-dipole interaction potential V_{12} as

$$\frac{4\pi\epsilon}{e^2} R^3\, V_{12}(\vec{x}_{Ba^+}, \vec{x}_{Rb}) = \vec{x}_{Ba^+} \cdot \vec{x}_{Rb} - 3\left(\vec{x}_{Ba^+} \cdot \frac{\vec{R}}{R}\right)\left(\frac{\vec{R}}{R} \cdot \vec{x}_{Rb}\right) \ . \tag{213}$$

To accommodate the macroscopic atom distribution of the rubidium Bose-Einstein condensate, the effective distance $\mathscr{R}$ between the barium (II) cation and a rubidium atom has been introduced as additional degree of freedom with an independent Hamiltonian part

$$\hat{h}_{\mathscr{R}} = -\frac{\hbar}{2M_{Rb}}\partial_{\mathscr{R}}^2 + \frac{\hbar}{4M_{Rb}\Delta_{Rb}^2}\mathscr{R}^2 - \frac{\hbar^2}{4M_{Rb}\Delta_{Rb}^2} \tag{214}$$

where M_{Rb} is the mass of a rubidium atom and Δ_{Rb} is the standard deviation of the spatial distribution of rubidium atoms which gives rise to a Gaussian distribution as ground state function. The last term provides a zero-point energy correction to the ground state which would otherwise be non-vanishing. This leads to the effective interaction potential proposed as

$$\frac{4\pi\epsilon}{e^2}\frac{\mathscr{R}^3}{N_{Rb}} V_{\text{eff}} = \rho\cos\varphi_{Ba^+}\, r\sin\vartheta\cos\varphi_{Rb} - 4\rho\sin\varphi_{Ba^+}\, r\cos\vartheta - 2\zeta\, r\sin\vartheta\sin\varphi_{Rb} \tag{204}$$

where the potential was integrated over the angle α between incident electron axis and atom-atom axis given by the vector $\vec{\mathscr{R}}$. Moreover, the total atom number N_{Rb} is counteracting the quick decay of the interaction with $\mathscr{R}^3$ which stabilises the model toward larger interatomic distances. The Hamiltonian operator of the system is then

$$\hat{H} = \hat{h}_{\mathscr{R}} + \hat{h}_{Ba^+} + \hat{h}_{Rb} + V_{\text{eff}}(\vec{x}_{Ba^+}, \vec{x}_{Rb}, \mathscr{R}) - (i\hat{W}) \ , \tag{215}$$

where $\hat{h}_k := \hat{T}_k + V_k(\vec{x}_k)$ denotes the respective Hamiltonian operator of the individual electron-ion subsystem $k \in \{Ba^+, Rb\}$ and $i\hat{W}$ indicates a complex absorbing potential as computational tool to prevent non-physical backscattering from the

edges of a finite numerical grid of points in space. The overall wavefunction of the system is then to be represented in the multi-configuration time-dependent Hartree (MCTDH) framework[90,91]

$$\Psi(t,\vec{x}_{Ba},\vec{x}_{Rb},\mathscr{R}) = \sum_{\mathrm{J}:=(j_\zeta,\ldots,j_r,\ldots,j_{\mathscr{R}})} A^{J}_{(t)}\Big(\mathscr{Z}^{j_\zeta}_{(t,\zeta)}\mathscr{Q}^{j_\rho}_{(t,\rho)}\mathfrak{f}^{j_\varphi}_{(t,\varphi_{Ba^+})}\Big)\Big(\mathfrak{u}^{j_r}_{(t,r)}Y^{j_Y}_{(t,\vartheta,\varphi_{Rb})}\Big)\mathfrak{R}^{j_{\mathscr{R}}}_{(t,\mathscr{R})} \tag{216}$$

as partially entangled configurations from Hartree products of low-dimensional wavefunctions indexed by the 6-tuple $J := (j_\zeta, j_\rho, j_{\vartheta_{Ba^+}}, j_r, j_Y, j_{\mathscr{R}})$ where $Y^{j_Y}_{(t,\vartheta,\varphi_{Rb})}$ represents a combination of the two primitive degrees of freedom ϑ and φ_{Rb} into one single-particle function. The electron dynamics are being computed with the Heidelberg MCTDH software suite.[93,121]

As initial wavefunction, the free electron shall be given by a spherical Gaussian distribution of initial transverse uncertainty $\Delta_\rho = 14.0\ a_B$ and longitudinal uncertainty $\Delta_\zeta = 7.0\ a_B$. It shall be centred at position $\zeta_0 = -85.0 a_B$ on the cylindrical axis with group momentum $p_0 = 0.39\ \hbar/a_B$ in positive ζ direction along the cylinder axis. Its single particle functions are then initially composed of the Hartree product from a longitudinal single-particle function (SPF)

$$\mathscr{Z}^{(0)}_{(0,\zeta)} := (2\pi\Delta_\zeta)^{-\frac{1}{4}}\ \exp\Big[-\Big(\tfrac{\zeta}{2\Delta_\zeta}\Big)^2 + \tfrac{i}{\hbar}p_0\,(\zeta-\zeta_0)\Big] \tag{217}$$

which is analogous to the initial condition for the quantum dot model and has been discussed in Section 4.1, from a lateral single-particle function

$$\mathscr{Q}^{(0)}_{(0,\rho)} := \frac{\sqrt{\rho}}{(2\pi\Delta_\rho^2)^{\frac{1}{2}}}\ \exp\Big[-\Big(\tfrac{\rho}{2\Delta_\rho}\Big)^2\Big] \tag{218}$$

where the factor $\sqrt{\rho}$ accounts for the normalisation with respect to the cylindrical volume element, and from an angular SPF

$$\mathfrak{f}^{(0)}_{(0,\varphi_{Ba^+})} := (2\pi)^{-\frac{1}{2}} \tag{219}$$

which is constant owing to the initially angle-independent cylindrical distribution of the incident electron wavepacket.

The rubidium electron is initially in its 5s ground state provided numerically by solving the stationary Schrödinger equation of the rubidium subsystem which is separable into a radial and an angular stationary Schrödinger equation and defines the initial single particles on rubidium by

$$\hat{h}_{Rb}\Big|_{\ell_{Rb}=0}\mathfrak{u}^{(0)}_{(0,r)} = E^{(0)}_{Rb}\mathfrak{u}^{(0)}_{(0,r)} \tag{220}$$

for the radial single-particle function such that the eigenenergy $E^{(0)}_{Rb}$ is minimal for vanishing angular momentum quantum number ℓ_{Rb} and represents the ground state, while the angular part of the rubidium subsystem shall be initially described by a single-particle function

$$Y^{(0)}_{(0,\vartheta,\varphi_{Rb})} := (4\pi)^{-\frac{1}{2}} \tag{221}$$

Table 2: Collection of computational parameters used to model an interatomic coulombic electron capture by a barium (II) cation assisted by a surrounding cloud of ultracold neutral rubidium atoms.

Incident electron parameters, see Eqs. (217) and (218)				
$p_0 = 0.39\ \hbar/a_B$		$\zeta_0 = -85.0\ a_B$	$\Delta_\zeta = 7.0\, a_B$	$\Delta_\rho = 14.0\, a_B$
Frozen-core pseudopotential parameters,[111,120] see Eq. (212)				
$Z_{Ba^{2+}} = 2\ e$		$\alpha_{Ba^{2+}} = 10.17\ E_H$	$\delta_{Ba^{2+}} = 2.06\ a_B$	
		$B_{Ba^{2+}} = 16.71\ E_H$		$b_{Ba^+} = 1.2543\ a_B$
Z_{Rb}	$= 1\ e$	$\alpha_{Rb} = 8.67\ E_H$	$\delta_{Rb} = 2.09\ a_B$	
		$B_{Rb} = 45.272\ E_H$		$b_{Rb} = 0.9941\ a_B$
M_{Rb}	$= 86.909181$ u	$N_{Rb} = 3{\times}10^6$	$\Delta_{Rb} = 5{\times}10^{-6}$ m	
DVR	type	grid points	range	
ζ	FFT	243	$-156.50\ a_B$	$+156.50\ a_B$
ρ	Generalized Laguerre $L_n^{(1)}$	125	$0.01\ a_B$	$159.77\ a_B$
φ_{Ba^+}	Periodic Exponential	15	0	2π
r_{Rb}	Generalized Laguerre $L_n^{(2)}$	125	$0.02\ a_B$	$160.43\ a_B$
$(\vartheta, \varphi_{Rb})$	Extended Legendre	7	$\ell_{Rb} \in \{0, \ldots, 6\}$	
		7	$m_{\ell_{Rb}} \in \{0, \ldots, \pm 3\}$	
$\mathscr{R}$	Generalized Laguerre $L_n^{(2)}$	122	$80.09\ a_B$	$6.98{\times}10^6\ a_B$
SPF configurations		$(9{\times}9{\times}4) \times (3{\times}4) \times 2$		
CAP		n	k	z_{cap}	η
		2	± 1	$\pm 100.0\ a_B$	$72.0 \times 10^{-6}\ E_H$

which shall be combined of two primitive angular degrees of freedom $(\vartheta, \varphi_{Rb})$ thus closely related to the spherical harmonic functions $Y_\ell^{m_\ell}$ and shall initially represent the ground state with angular momentum quantum number $\ell_{Rb} = 0$. Eventually the atom distribution of rubidium atoms is initialised by the ground state with respect to the stationary Schrödinger equation which has a vanishing eigenenergy by construction

$$\hat{h}_{\mathscr{R}} \mathfrak{R}^{(0)}_{(0,\mathscr{R})} = 0\,. \tag{222}$$

Moreover, a cylindrical volume $\mathscr{V}$ shall be defined with the barium (II) ion at the centre, which is enclosed by its boundary

$$\partial\mathscr{V} = \hat{A}_\zeta^- + \hat{A}_\rho + \hat{A}_\zeta^+ \tag{223}$$

$\partial\mathscr{V}$ being composed of a circular area $A_\zeta^\pm$ at either end of the cylinder at $\zeta = \pm\zeta_\mathscr{V}$ such that it may be expressed by the operator

$$\hat{A}_\zeta^\pm := \rho^2\ \varphi_{Ba^+}\ \ \delta(\zeta \mp \zeta_\mathscr{V})\ \ \Theta(\rho_\mathscr{V} - \rho) \tag{224}$$

and a closed lateral surface at $\rho_\mathscr{V}$ given by the operator

$$\hat{A}_\rho := \rho^2\ \varphi_{Ba^+}\ \Theta(\zeta_\mathscr{V}^2 - \zeta^2)\ \delta(\rho - \rho_\mathscr{V}) \tag{225}$$

where the cylinder dimensions have been set numerically to $\zeta_\mathscr{V} = \rho_\mathscr{V} = 100\ a_B$, $\delta(x)$ represents the Dirac delta function and $\Theta(x)$ represents the Heaviside step function

defined by $\Theta(x < 0) := 0$ and $\Theta(x \geq 0) := 1$. Then, the electron flux F_ζ^0 into the observation volume $\mathscr{V}$ may be analysed as well as the electron outflow $F_\zeta^\pm$ and F_ρ through the respective boundary area of $\partial\mathscr{V}$. The overall capture probability P_c^T of the computer experiment is then given by the large-time limit of the relative difference between integrated electron flux into and out of the volume $\mathscr{V}$,

$$P_c^T = \lim_{t\to\infty} \frac{\int dt \left(F_\zeta^0 - (F_\zeta^- + F_\rho + F_\zeta^+)\right)}{\int dt\ F_\zeta^0} \tag{226}$$

due to the continuity of electric charge in the barium subsystem. A Fourier analysis of the individual contributions of electronic flux eventually allows to resolve the electron capture probability as function of total energy E of the system by

$$P_c(E) = 1 - \frac{F_\zeta^-(E) + F_\rho(E) + F_\zeta^+(E)}{F_\zeta^0(E)}\ . \tag{227}$$

7.2 Results

The numerical implementation of a dynamical simulation involving the full system is demanding considerable computational resources owing to the extreme differences between electronic free states and bound states. The cylindrical description introduces two degrees of freedom demanding a continuum for the barium (I) subsystem which is composed of the frozen barium (II) cation and an independent electron within the effective potential field. However, for the free motion of the incident electron, the composition of the wavefunction is satisfied with a handful of single-particle functions for each degree of freedom. In contrast, an accurate composition of barium (I) eigenfunctions calls for a larger set of single-particle functions in the two continuum directions. While the relaxation of barium (I) eigenfunctions can incorporate more single-particle functions in its A-vector, the propagation of the full system is more restricted and its computability poses a technical limit to the size of the A-vector. Figure 16 shows the numerical eigenfunctions of a barium (I) cation and those of a rubidium atom at a distance of $\mathscr{R} = 100\ a_B$ in the numerical implementation used for the computations of the electron dynamics of the full system. Restricting the composition of barium (I) eigenfunctions to nine single-particle functions in longitudinal direction ζ_{Ba}, nine in transversal direction ρ_{Ba} and three in angular direction φ_{Ba}, introduces deviations of the numerical eigenenergies from the expected known experimental ones.[82,84] The numerical ground state energy of $E_{Ba^+_0} = -544.7\times10^{-3}\ E_H$ faces the experimental value of $-366.7\times10^{-3}\ E_H$.[82,84] The experimental eigenenergies are indicated by constant dark grey lines below $\rho_{Ba} = 0$ for comparison with the numerical values which can be read of at the onset of the depicted energy-shifted wavefunctions. For the scope of this study towards a first numerical model, the deviation between numerical realisation and real manifestation is acknowledged but shall not hinder the validation whether ICEC may be successfully undergone within the proposed model. The underlying black dashed line indicates the atomistic effective binding potential employed for the barium (I) subsystem and for the rubidium atom respectively. The description of the rubidium atom by a local spherical subsystem closer to the known spectral lines of rubidium.[82,83] The spherical rubidium subsystem remains separable into its describing degrees of freedom and the one-dimensional eigenfunctions of the employed binding potential are

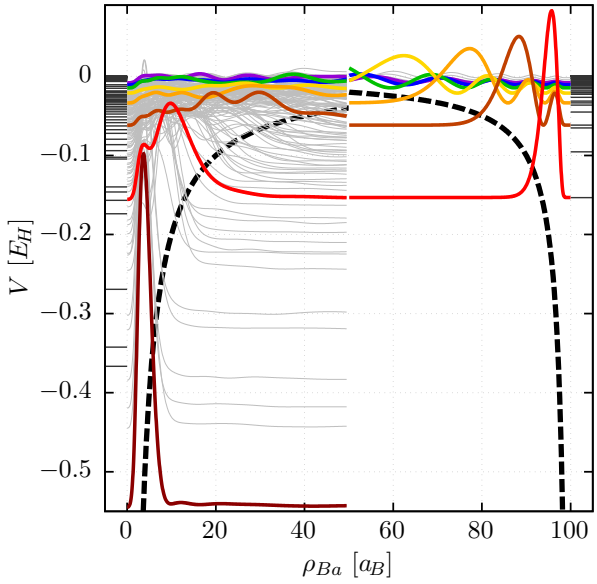

Figure 16: Comparison of the eigenvalue-shifted reduced probability densities $|\psi^{(n)}_{Ba^+}(\rho)|^2$ of wavefunctions of an electron in an approximate barium (II) binding potential with reduced probability densities $|\psi^{(m)}_{Rb}(r)|^2$ of electron eigenfunctions in an approximate rubidium (I) binding potential. The first hundred-fifty transverse wavefunctions of the barium (I) cation expressed in cylindrical coordinates are not separable in ρ which renders the reduced probability density in ρ into a superposition of states with different quantum numbers (n, ℓ, m_ℓ) and do not show a clear nodal structure which is depicted as grey lines and coloured lines on the left. The first ten radial electron wavefunctions of rubidium which is here situated at a distance of $\mathscr{R} = 100\ a_B$, are well-described by a one-dimensional wavefunction and a single quantum number n such that they show a clear nodal structure in their reduced radial probability density here depicted as grey and coloured lines on the right energetically shifted according to their eigenenergies. The experimental values for the energy levels are indicated as solid dark grey lines along the abscissa on the respective side. The black dashed line indicates the respective binding potential used in the numerical model. Matching colours on the left and the right indicate wavefunctions of comparable binding energy.

independent of the number of single-particle functions. The illustrated radial wavefunctions originating at $\rho_{Ba} = 100\ a_B$ toward the barium (I) cation thus agree well with the spectral lines indicated at larger distances. Unmet intermediate spectral lines generally belong to p and d orbitals which are not represented by the current implementation of the binding potential as the used software suite remains in want of angular momentum projection operators to successfully implement variations of binding strengths as function of the angular momentum.

In the current numerical setup, six electronic eigenstates align to comparable eigenenergies between the first one-hundred-and-fifty eigenstates of the barium (I) cation and the first ten eigenstates of the rubidium atom subsystem. These are

indicated by matching colours in Figure 16. The rubidium ground state has an energy of $E_{Rb_0} = -153.2 \times 10^{-3}\ E_H$ which is met by the fourteenth excited state $E_{Ba^+{}_{14}} = -155.5 \times 10^{-3}\ E_H$ on the barium (I) cation. The first excited state of energy $E_{Rb_1} = -61.7 \times 10^{-3}\ E_H$ on rubidium faces the fifty-third on the barium ion with energy $E_{Ba^+{}_{53}} = -61.8 \times 10^{-3}\ E_H$. Similarly, the second excited state with energy $E_{Rb_2} = -33.6 \times 10^{-3}\ E_H$ on rubidium faces an energy of $E_{Ba^+{}_{89}} = -33.7 \times 10^{-3}\ E_H$ of the eighty-ninth excited state on barium (I) whereas the third and fourth excited states of energies $E_{Rb_3} = -21.1 \times 10^{-3}\ E_H$ and $E_{Rb_4} = -14.5 \times 10^{-3}\ E_H$ meet the respective energies of $E_{Ba^+{}_{113}} = -21.1 \times 10^{-3}\ E_H$ and $E_{Ba^+{}_{129}} = -14.6 \times 10^{-3}\ E_H$ of the hundred-thirteenth and hundred-twenty-ninth excited state on the barium (I) ion. Eventually, the fifth and sixth excited state at energies $E_{Rb_5} = -10.6 \times 10^{-3}\ E_H$ and $E_{Rb_6} = -8.1 \times 10^{-3}\ E_H$ on rubidium juxtapose the energies $E_{Ba^+{}_{138}} = -10.9 \times 10^{-3}\ E_H$ and $E_{Ba^+{}_{143}} = -8.3 \times 10^{-3}\ E_H$ of the hundred-thirty-eighth and hundred-fourty-third excited state on the barium (I) cation. The number of numerical radial eigenstates of rubidium is restricted by the applied resolution of primitive basis functions such that nine eigenstates with eigenenergy below zero can be achieved for the employed computational setup. It is expected that each of these eigenstates on rubidium finds a matching state with eigenenergy on barium (I) although only the first six rubidium eigenstates found a comparable level within the first hundred-fifty relaxed eigenstates of the barium ion. Graphically, the excited states of rubidium and barium (I) of equal colouring fail to match up in their respective height at their facing point at $\rho_{Ba^+} = 50\ a_B$ because the long tail of the respective effective binding potentials results in a considerable remaining amplitude of the wavefunctions which were graphically cut-off at $50\ a_B$ from their respective binding centres.

In the following, the numerical results of the simulation of such a prospective ICEC experiment at the given typical experimental conditions shall be presented and analysed in line with the methodical analysis applied to the results presented in Figure 6. To this goal, Figure 17 presents the flux densities and spatial probability densities projected on the degrees of freedom ρ_{Ba^+} and ζ_{Ba^+} in the barium (I) subsystem and in r_{Rb} within the rubidium subsystem as functions of time t for the interatomic electron capture onto the central barium (II) cation in a cloud of ultracold rubidium atoms of dimensions in the range of several millimetres as is typical for current hybrid-trap experiments with ultracold atoms. Analogously to Figure 6 (a-c), the individual columns illustrate the full dynamics in column (a), the difference to a reference computation excluding interatomic electron-electron interaction in column (b) and the reference computation itself in column (c). Arising from the increased dimensionality of the simulation, each column presents the contributions to the outgoing electron flux density measured around the barium (II) cation or the rubidium atom in the upper panel and the projected spatial probability density onto the three individual degrees of freedom of longitudinal direction ζ_{Ba^+}, transverse direction ρ_{Ba^+} and radial direction r_{Rb} in the respective rows below. Starting with the reference simulation of to familiarise with the time evolution of the incident electron in the absence of interaction with the electron on rubidium, the time-dependent results and their graphical illustration in the figure will be described and analysed in the following paragraphs.

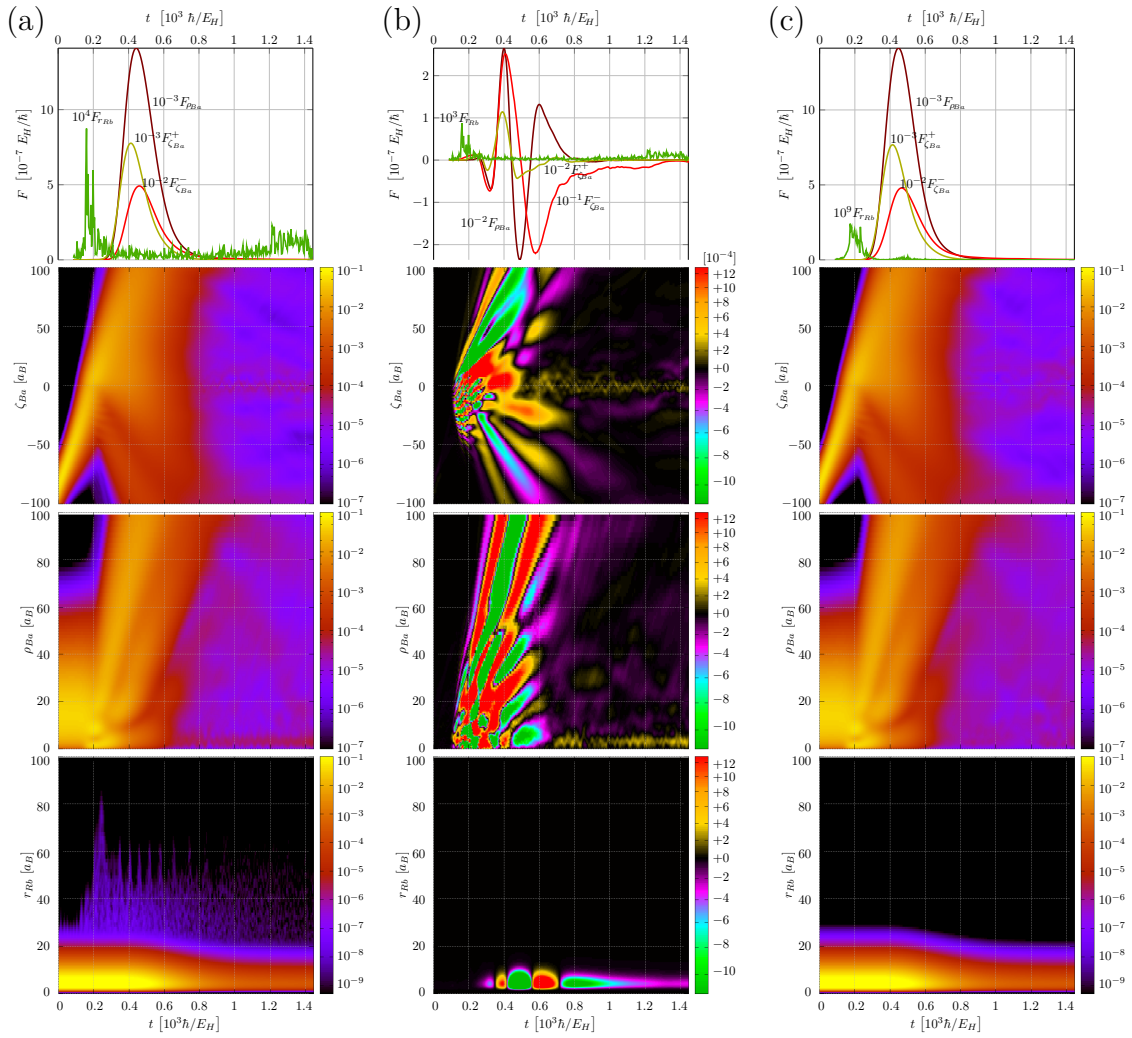

Figure 17: Dynamics of interatomic coulombic electron capture onto barium (II) through dipole-dipole interaction with the outermost valence electrons of a cloud of ultracold rubidium atoms distributed spherically around the barium (II) cation. (a) The full electron dynamics. (b) The difference between the full dynamics and a reference computation of independent electrons. (c) The simulation of independent electrons at same initial conditions but denying interatomic interaction or energy transfer.

The reference simulation of independent electrons shows that the scattering of the incident electron wavepacket on the barium (II) cation induces a quick dispersion of the wavepacket over the entire available longitudinal and transversal domain.

Most instructing, is the graph in the second row of the Figure 17 column (c) which depicts the spatial probability density in longitudinal direction ζ_{Ba^+}. The yellow colour indicates a high density of $10^{-1}\ a_B^{-1}$ and above which fades via bright orange at a density of $10^{-2}\ a_B^{-1}$ and orange at a density of $10^{-3}\ a_B^{-1}$ to red, violet and blue at respective spatial probability densities of $10^{-4}\ a_B^{-1}$, $10^{-5}\ a_B^{-1}$ and $10^{-6}\ a_B^{-1}$. For spatial probability densities at $10^{-7}\ a_B^{-1}$ and below. At initial time, the incident electron is spread in space indicated by the colouring at $t = 0$ of approximately 70 a_B below $\zeta_{Ba^+} = -50a_B$. The barium (II) cation is situated at constant $\zeta_{Ba^+} = 0\ a_B$

throughout the entire simulation. The attraction of the free wavepacket accelerates the electron toward $\zeta_{Ba^+} = 0\ a_B$ which is visible at the increasing slope $\Delta\zeta_{Ba^+}/\Delta t$ with time t of the wavepacket's forefront. Simultaneously, the wavepacket spreads over time such that its tail propagates decreasing slope with increasing time but the width of the blue region indicating low spatial density increases with time. As the forefront passes the height $\zeta_{Ba^+} = 0\ a_B$ of the barium (II) cation at time about $t \approx 100\hbar/E_H$, it disperses rapidly toward positive and negative ζ_{Ba^+} as well as toward the transverse direction of ρ_{Ba^+} indicated in the panel below. As the forefront is partially reflected in longitudinal direction and moves back to smaller ζ_{Ba^+}, it encounters parts of the wavepacket still propagating toward the barium (II) cation at $\zeta_{Ba^+} = 0\ a_B$ which induces interference between the partial waves which are visible as slightly darker ridges within the orange regions from time $t = 200\hbar/E_H$ onwards at which time the maximum of the wavepacket arrives at $\zeta_{Ba^+} = 0\ a_B$.

As the portions of the spreading wavepacket reach a longitudinal distance of $\zeta_{Ba^+} = \pm 100\ a_B$, they are registered as respective flux density $F^{\pm}_{\zeta_{Ba^+}}$ on the upper graph of Figure 17 (c) and the same holds for a transverse distance of $\rho_{Ba^+} = 100\ a_B$ which registers as flux density $F_{\rho_{Ba^+}}(t)$ as function of time. The maximum over time in longitudinally transmitted flux density of $\max_t F^{+}_{\zeta_{Ba^+}} = 768 \times 10^{-6}\ E_H/\hbar$ occurs at time $t = 413\ \hbar/E_H$ before the maximum over time is reached in the transverse direction with a flux density of $\max_t F_{\rho_{Ba^+}} = 1412 \times 10^{-6}\ E_H/\hbar$ at time $t = 446\ \hbar/E_H$. As last, the temporal maximum of the longitudinally reflected flux density of $\max_t F^{-}_{\zeta_{Ba^+}} = 48 \times 10^{-6}\ E_H/\hbar$ is reached at simulation time $t = 466\ \hbar/E_H$. Owing to the increasing spatial uncertainty with increasing time and the uncertainty in momentum, the individual flux density contributions rise quickly to their respective temporal maxima but decrease gradually more slowly with increasing time. As a result, the entire domain is covered by the incident wavepacket at time $t = 400\hbar/E_H$ and spatial probability density remains distributed from the barium (II) cation at $(\zeta_{Ba^+}, \rho_{Ba^+}) = (0, 0)$ beyond the onset of the complex absorbing potentials at $\zeta_{\text{cap}} = \pm 100\ a_B$ and at $\rho_{\text{cap}} = 100\ a_B$ respectively. However, as increasing portions of the initial wavepacket have effectively left the region of observation, the spatial probability density decreases considerably, which is indicated by the colouring changing from orange and red to violet and blue while it remains distributed over the entire observation volume surrounding the barium (II) cation. Simultaneously, the spatial probability density of the radial part around the rubidium atom is depicted in the last row of Figure 17 column (c) as function of radius r_{Rb} and time t. It remains constant until $t = 400\ \hbar/E_H$ where it begins to decay slowly. This is only marginally due to any electronic flux density leaving the rubidium atom which is of the order of $10^{-16}\ E_H/\hbar$ only as indicated in the upper panel as $F_{r_{Rb}}$. There it shows a rather random broad shoulder from $t = 150\ \hbar/E_H$ to $t = 250\hbar/E_H$ which is approximately the time interval from when the maximum of the incident wavepacket arrives at the barium (II) cation to when the forefront begins to numerically leaves the barium subsystem at distance of $100\ a_B$. The very small flux density on rubidium thus appears to be a numerical echo of large interaction which also revives at a much smaller magnitude around the time of the maximal flux density in transversal direction on barium (II). The gradual decrease of probability density around the rubidium atom is thus the numerical phenomenon of the combined two-electron

wavefunction parts of which are continuously leaving the barium subsystem.

The fully interactive electron dynamics depicted in Figure 17 column (a) appears very similar to the reference simulation but shows continuous spurts of flux density leaving the rubidium atom and at larger times an increase of spatial probability density around the barium (II) cation. While remaining orders of magnitude smaller than the flux densities seen exiting the barium (II) cation, the flux density sent out from the rubidium atom is orders of magnitude larger and more continuous over the depicted time frame than in the reference computation. This is also clearly visible as blue sprays in the graph of the spatial probability density projected onto r_{Rb} in the lowest row. The flux density measured radially around the rubidium atom is thus mainly induced by interatomic energy transfer between the electrons of at least $\Delta E_{Rb} = 142.5 \times 10^{-3}\ E_H$ necessary to excite the ground state to the fifth excited state on rubidium which is the first to extend beyond $r_{Rb} = 100\ a_B$ in its spatial probability density and lies only $10.6 \times 10^{-3}\ E_H$ below the absolute continuum. The dominating features of the flux density leaving the barium (II) cation, however, remain quantitatively similar to the reference simulation. In longitudinal direction, the temporal maximum in transmitted flux density reaches $\max_t F^+_{\zeta_{Ba^+}} = 777 \times 10^{-6}\ E_H/\hbar$ at same time $t = 413\ \hbar/E_H$ whereas the transverse flux density climaxes with $\max_t F_{\rho_{Ba^+}} = 1409 \times 10^{-6}\ E_H/\hbar$ at time $t = 442\ \hbar/E_H$ slightly faster than the reference. The longitudinally reflected flux density increases up to $\max_t F^-_{\zeta_{Ba^+}} = 49 \times 10^{-6}\ E_H/\hbar$ at time $t = 458\ \hbar/E_H$. Qualitative different, the electron-electron interaction induces a faster yet quantitatively minor spray of spatial probability arriving at the longitudinal and transversal borders of the depicted region at $t = 200\ \hbar/E_H$ while the main body of the dispersed wavepacket arrives around $t = 250\ \hbar/E_H$ as in the reference case. At the same instant in time, the spatial probability density shows the largest extension in radial direction around the assisting rubidium atom.

As the average spatial probability density decreases gradually with time around the barium (II) cation, a small portion in the order of $2 \times 10^{-5}\ a_B^{-1}$ accumulates within $7\ a_B$ around the barium (II) cation in addition to the widespread background distribution of the dispersed wavepacket. This is indicated on the one hand, by the oscillating dark-red colouring in spatial probability density around the barium position in ζ_{Ba^+} and ρ_{Ba^+} in Figure 17 column (a). It is also highlighted more clearly, on the other hand, by a yellow colouring against a black background in the difference in spatial probability densities of the interactive with respect to the non-interactive simulation which is illustrated in the two middle panels of Figure 17 column (b) after time $t = 600\ \hbar/E_H$. While surplus and lack of spatial probability is mainly leaving the observation region around the barium (II) cation in an oscillating fashion in time until approximately $t \approx 900\ \hbar/E_H$, a clearly shaped surplus probability density retains its proximity near the cation for the remaining depicted time of $\Delta t = 500\ \hbar/E_H$.

Indicating a coinciding evolution up to $t = 100\ \hbar/E_H$ in all three presented degrees of freedom, the interaction-induced deviations of the projected-probability and flux densities propagate in an intricate oscillatory fashion. The deviation in flux density

illustrated in the upper panel presents a clear yet random-looking continuous surplus in radial flux density $F_{r_{Rb}}$ on the rubidium atom. This underlines it to be a purely interactive effect. In contrast, the deviation in flux density exiting from the barium (II) cation oscillates between surplus and deficit. In transverse direction, the deviation in flux density $\Delta_I F_{\rho_{Ba^+}}$ shows three temporal extrema in surplus with the largest of $\max_t \Delta_I F_{\rho_{Ba^+}} = +26.5 \times 10^{-6}\ E_H/\hbar$ at time $t = 401\ \hbar/E_H$ and shows two temporal extrema in deficit with the largest being $\min t \Delta_I F_{\rho_{Ba^+}} = -23.6 \times 10^{-6}\ E_H/\hbar$ at time $t = 488\ \hbar/E_H$. In longitudinal transmission direction, the deviation in flux density indicates three temporal extrema in surplus with the largest reaching $\max_t \Delta_I F^+_{\zeta_{Ba^+}} = 11.4 \times 10^{-6}\ E_H/\hbar$ at time $t = 393\ \hbar/E_H$ and indicates two temporal extrema in deficit with the largest reaching $\min t \Delta_I F^+_{\zeta_{Ba^+}} = -4.3 \times 10^{-3}\ E_H/\hbar$ occuring at time $t = 475\ \hbar/E_H$. In longitudinal reflection direction, the flux-density deviation presents only two temporal extrema in surplus with the maximum measuring $\max_t \Delta_I F^-_{\zeta_{Ba^+}} = 2.5 \times 10^{-6}\ E_H/\hbar$ at time $t = 405\ \hbar/E_H$ and presents two extrema in deficit ending on the largest of $\min t \Delta_I F^-_{\zeta_{Ba^+}} = -2.2 \times 10^{-6}\ E_H/\hbar$ at time $t = 579\ \hbar/E_H$. Similarly, the deviation in spatial probability density illustrated in the three lower panels of Figure 17 column (b) oscillate between regions of surplus and deficit which flow outward in the case of the barium (II) cation and appear mainly localised within a radius of 10 a_B for the case of the rubidium subsystem. The colouring in the plot of probability-density deviation is shown in multiples of $10^{-4}\ a_B^{-1}$. While ending on a temporally extremal deficit of $\Delta_I |\langle r_{Rb}|\Psi\rangle|^2 = -148 \times 10^{-6}\ a_B^{-1}$ at radial distance $r_{Rb} = +4.387\ a_B$ and time $t = 798\ \hbar/E_H$, the radial distribution and amount of deficit decrease with time as the overall norm contained within the observation volume decrease with the exiting wavepacket on the barium subsystem.

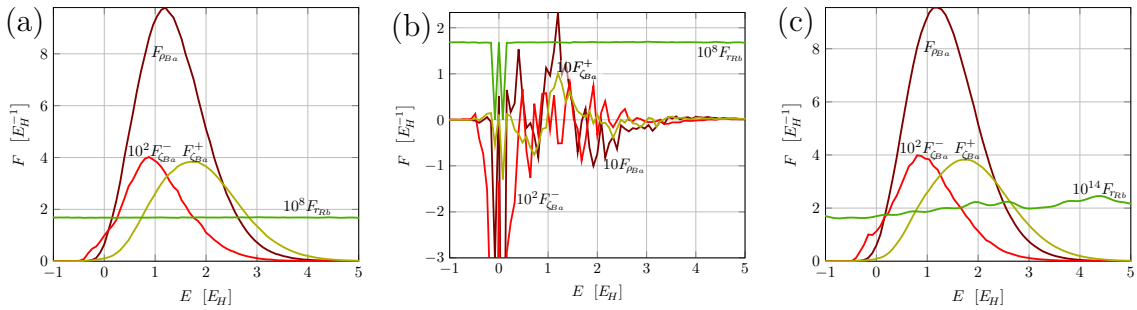

Figure 18: Electron flux density $F(E)$ as function of system energy E for an incident electron on a frozen barium (II) interacting through dipole-dipole interaction with the outermost valence electrons of a Bose-Einstein condensate of rubidium atoms distributed spherically around the cation. (a) The flux density spectrum for the full electron dynamics. (b) The deviation of the fully interactive flux density spectrum from the reference flux density spectrum of independently evolving electrons at equal initial conditions. (c) The spectrum of flux density for a reference simulation of same initial conditions but denying interatomic electron-electron interaction.

The Fourier transform with respect to time of the measured flux density $F(t)$ evaluates the spectrum of the flux density $F(E)$ as function of energy E which

is depicted in Figure 18 but shows barely any difference between the full dynamics and the reference computation. Figure 18 (a) is representing the flux density spectra of the full dynamics. Figure 18 (c) represents the flux density spectra of the interaction-free reference computation. Comparing both computations, the flux densities associated with the barium subsystem show a bell function with a single maximum each while the radial flux density measured for the rubidium subsystem shows an apparently energy independent value of $F_{r_{Rb}} = 17 \times 10^{-9}\ E_H^{-1}$ in the fully interactive case and in the case of the reference simulation a much smaller, widespread and weakly fluctuating flux density of maximally $F_{r_{Rb}} = 30 \times 10^{-15}\ E_H^{-1}$. The transverse flux density spectra juxtapose a spectral maximum of $\max_E F_{\rho_{Ba^+}} = 9.78\ E_H^{-1}$ at energy $E = 1.2\ E_H$ and full width at half maximum of $1.55\ E_H$ in the full dynamics against a spectral maximum of $\max_E F_{\rho_{Ba^+}} = 9.55$ at same energy but with full width at half maximum of $1.58\ E_H$ in the non-interactive reference case. In longitudinal direction, the transmissive flux density climaxes at flux density of $\max_E F^+_{\zeta_{Ba^+}} = 3.84\ E_H^{-1}$ at system energy $E = 1.76\ E_H$ width full width at half maximum of $1.96\ E_H$ for the full-interaction dynamics but climaxes at a flux density of $\max_E F^+_{\zeta_{Ba^+}} = 3.83\ E_H^{-1}$ with full width at half maximum of $1.98\ E_H$ at the same system energy in the reference computation. Eventually, the reflected longitudinal flux density reaches $\max_E F^-_{\zeta_{Ba^+}} = 0.402\ E_H^{-1}$ with full width at half maximum of $1.32\ E_H$ at energy of $E = 0.88\ E_H$ in the computation of the full dynamics and reaches $\max_E F^-_{\zeta_{Ba^+}} = 0.399\ E_H^{-1}$ with full width at half maximum of $1.39\ E_H$ at energy $E = 0.80\ E_H$ in the non-interactive reference.

The large agreement in both cases by their respective spectra leads to diffuse difference spectra shown in Figure 18 (b). The erratic spectra of the deviation in flux density all find their maximal deficit at a system energy of $E = 0.08\ E_H$. At this energy, the maximal deficit in transverse flux density on barium (II) reads $\min_E \Delta_I F_{\rho_{Ba^+}} = -1.01\ E_H^{-1}$, the maximal deficit in longitudinally transmitted flux density on barium (II) reaches $\min_E \Delta_I F^+_{\zeta_{Ba^+}} = -0.13\ E_H^{-1}$, the its reflected equivalent touches $\min_E \Delta_I F^-_{\zeta_{Ba^+}} = -0.13\ E_H^{-1}$, and the radial flux density on rubidium sees a deficit of $\min_E F_{r_{Rb}} = -17 \times 10^{-15}\ E_H^{-1}$. All deviations in flux density show a deficit at energies $E = \pm 0.08\ E_H$ while all except $\Delta_I F^-_{\zeta_{Ba^+}}$ are offering a surplus at $E = 0\ E_H$. Their maximal spectral surplus reaches $\max_E \Delta_I F_{\rho_{Ba^+}} = +0.23\ E_H^{-1}$ in transverse direction on barium (II) at energy $E = 1.20\ E_H$, touches $\max_E \Delta_I F^+_{\zeta_{Ba^+}} = +0.10\ E_H^{-1}$ in longitudinal transmission direction on barium (II) also at energy $E = 1.20\ E_H$, $\max_E \Delta_I F^-_{\zeta_{Ba^+}} = +8.2 \times 10^{-3}\ E_H^{-1}$ in longitudinal reflection direction on barium at energy $E = 1.44\ E_H$, and climaxes at $\max_E \Delta_I F_{r_{Rb}} = +16 \times 10^{-9}\ E_H^{-1}$ in radial direction on rubidium for an energy of $E = 3.04\ E_H$. The difference in flux density between interactive and non-interactive case is clearly too small to draw any sensible conclusions. This implies however, that the fraction of interatomically captured electron wavefunction is yet too small.

Overall, the full electron dynamics computations for prototypical ICEC experiment at macroscopic conditions proved to be very numerically demanding due to their large dimensionality and partial inseparability of coordinate subsystems but proved to successfully undergo ICEC with a surplus in spatial probability densities

at time $t = 2\,150\ \hbar/E_H$ of $\Delta_I|\langle\rho_{Ba^+}|\Psi\rangle|^2 = +47.7 \times 10^{-6} a_B^{-1}$ at transverse distance of $\rho_{Ba^+} = 3.28\ a_B$ from the centre barium (II) cation and of $\Delta_I|\langle\zeta_{Ba^+}|\Psi\rangle|^2 = +39.0 \times 10^{-6} a_B^{-1}$ at longitudinal distance of $|\zeta_{Ba^+}| = 1.29\ a_B$ from the cation. Though a winning proof of principle, several shortcomings were encountered during the implementation of the model within the frame of the employed software suite. At the current stage, the unavailability of implemented angular momentum operators, spherical or solid harmonic and Bessel functions appear the major impediments to a more robust, more accurate and potentially faster implementation. This would allow on the one hand, to describe the various potentials more efficiently and more accurately, and would possibly enable a transfer of the barium subsystem into spherically symmetric coordinates by a more opportune description of the initial wavepacket. This would allow to reduce the amount of primitive basis functions and single-particle functions at the same time which might free numerical resources to be employed on better accuracy or potentially on the transfer from a barium (II) cation to a barium (I) cation by adding an additional valence electron to the system. This step would have considerable significance in light of the fact that current realisations of hybrid traps for ultracold atoms solely work with the singly charged cations. Moreover, the here used effective two-electron model neglects the possibility of consecutive dissipation pathways through intra-atomic energy down-conversion or dielectronic excitations which could in turn enhance the ICEC rate. In a exclusively two-electronic model, an intermediate interatomic energy transfer which may have bound the incident electron temporarily but has not sufficed to ionise the assisting electron on the neighbour will be able to transfer energy back to the incident electron. If a third electron were present within the model, this would open up additional dielectronic reaction pathways to stabilise the interatomic coulombic electron capture.

Part IV
Conclusion

On the one hand, interatomic coulombic electron capture is a fundamental yet novel process. On the other hand, theoretical descriptions are challenging and experimental investigations have not yet been conducted. Starting from the established numerical model of quantum confinements within a nanowire, this dissertation appended to existing observations on dynamics computations within the effective-two-electron treatment of the model from which it drew model-independent hypotheses for future investigations. Introducing a second application, it adapted the model to test whether the effective-two-electron treatment suffices to successfully undergo ICEC in the experimentally motivated system of a barium (II) cation engulfed in a Bose-Einstein-condensate of neutral rubidium atoms. The electron dynamics were computed in the framework of the multi-configurational time-dependent Hartree approach employing the software suite of same name and resulted partially in an environment-assisted electronic attachment of an incident free electron. The outgoing electronic flux density was then analysed in correlation with available electronic states within the confinement region and with respect to the directional dependence of the outbound flux. Moreover, the effects arising from the dynamical energy transfer between the two treated electrons was referenced against their otherwise independent motion through the system.

Arisen Conjectures on Prospective Investigations

This work discussed the full state-resolved spectra of reflected and transmitted contributions to the outgoing flux density and related ICEC probability at a particular set-up, then presented the quantum size effect on the reflected and transmitted maximum of the spectrum of ICEC flux density, as well as maximum and expectation value of the ICEC probability spectrum over a range of set-ups with varying capture lengths, before analysing the maximum of the transmitted ICEC probability spectrum over a domain of sizes and confinement energies of the capturing quantum dot at various distances between the quantum confinements in comparison to trends in two available states localised within the capturing confinement. Providing an extensive addition to the presently published findings on the dynamics of this system, the numerical results suggest that the interatomic coulombic electron capture is primarily governed by two distinct reaction pathways. Appearing to be associated to differing electronic states of the confinement region, the two subprocesses can show individual preference over spatial directions and different resonant energies. For the investigated range of parameters, the energy levels of these associated states suggest to provide a starting point for a more comprehensive description beyond the particular parameters of an individual model. The optimal ICEC efficiency for the sampled setups exceeded 55 %.

Overall, the presented data supports the following conjectures for prospective directed investigations. An arbitrary confinement including atoms, molecules or quantum-dots may be modified through any available control parameter, may it

be size, element, material, applied local fields, various media or other. The eigenenergies of associated electron states of the involved confinements can be used as independent descriptors to comprehend ICEC beyond the underlying model, set-up or parameters. The dependence on the distance between the capturing confinement and the interaction partner remains a significant modifier to the associated resonant energies though.

Benefits and Impediments of a Bielectronic Model

Successful for pairs of effective-mass approximated electrons in artificial confinements, the established model was then adapted to treat a prototypical electron capture by a barium (II) cation aided through a surrounding cloud of ultracold rubidium atoms. Whereas lower valence and core-electron excitations were neglected together with the asymmetric contribution from different electronic angular momenta, a rather simple electric dipole-dipole coupled model was able to successfully show environment-assisted electron attachment in typical experimental conditions. Many-particle interactions in a semiconducting medium can thus be averaged at least conceptually to a particle with adapted effective mass, macroscopic confinements can lead to artificial discrete energy levels not unlike those in much smaller single atoms or theoretical equivalents of even lower degrees of freedom, and multicharged nuclei and lower lying electrons may be averaged under certain conditions to an effective frozen core pseudopotential for outer valence electrons. In the case of an environment of distributed ultracold interaction partners for an interatomic coulombic electron capture, it appears a reasonable first approach to treat the cumulative environment effectively.

The main advantages of this treatment are twofold. On the one hand, the cumulated potential over the large number of interaction partners counters the numerically quickly vanishing interaction potential of the individual partner at typically rather large distances to the capturing atom. This allows to consider macroscopic distributions of typical experimental conditions which would otherwise lie beyond numerically possible accuracy and feasibility. On the other hand, the treatment as single effective interaction partner with macroscopic spatial uncertainty offers the opportunity to limit the increase in degrees of freedom to a single additional variable and still conceptually account for the cumulative effect of the surrounding atoms. This allows to keep the demand on numerical resources in check.

There are two apparent disadvantages of this effective bielectronic model. First, it does not allow additional electronic responses neither to aid nor to hinder the electron capture. Transferred energy between electrons on different sites may dissipate through local energy conversion which is not possible in this treatment such that it excessively transfers back in lack of other channels. Second, barium (I) cations are used in hybrid trap experiments, not barium (II) cations. These involve an additional outer valence electron experiencing the same pseudopotential from the frozen core as the incident electron while interacting with it. This is not treated in this two-electron model. Simultaneously, arriving at an experimental realisation with barium (II) cations will demand considerably more effort.

Apart from the advantages and disadvantages of the effective two-electron approximation, some aspects of the current implementation of the model could profit from a different realisation but lack the necessary features in the currently available software suites. Among these are a more accurate description of the frozen-core pseudopotential by additional dependence on the electronic angular momentum involving angular momentum projection operators, a more advanced description of the Coulomb potential or an alternative description of the barium subsystem in a spherical coordinate system both involving the introduction of Bessel functions.

In conclusion, the implementation of the introduced model within the chosen method presented a compromise over an already high demand of computational resources. Increasing the number of or the resolution in the chosen degrees of freedom as well as reducing the level of approximations will quickly render the problem non-computable. Several adaptations to the model suggest improving the accuracy at a small computational cost but are not implemented in the available software suites and would demand considerable effort in their adaptation. Nevertheless, the current implementation of the model by an effective two-electron treatment was successful in undergoing interatomic coulombic electron capture at typical macroscopic experimental conditions. On the other hand, the derived model allowed, however, to bridge the gap between the atomic scale interaction and the three orders of magnitude larger average distance to the first available partner atom for an interatomic coulombic electron capture in ultracold atoms. Furthermore, the extended investigative revision of ICEC in nanowire-embedded quantum dots revealed in a methodological approach that interatomic coulombic electron capture can lead to a release of the assisting nearby electron in the direction masked by the reflection of the incident electron. The previously relied upon ionisation flux density measured in direction of transmission thus presents only one but often dominant part of the actual overall fraction of interatomic coulombic capture of the incident electronic wavepacket. A previously unavailable extent of computational data proved consistently throughout the sampled range of confinement parameters that the electron dynamics and capture efficiency are dominantly following significant single-electron eigenenergies of the system. The simulations strongly support recent related studies[2,64] and suggest these dominant two energy levels are respectively related to two different reaction pathways one of which engages ICD. Concluding, it has been hypothesised that future investigations of ICEC dynamics are probable to profit from a resolution of their findings in terms of the single-electron eigenstates and interatomic distance rather than the employed model parameters of the specific confinement. This will eventually allow to make the description and analysis of interatomic coulombic electron capture dynamics model-independent and the observations portable to other theoretical and experimental realisations.

References

[1] K. Gokhberg, and L. S. Cederbaum, 'Environment assisted electron capture', J. Phys. B **42**, 231001 (2009) 10.1088/0953-4075/42/23/231001.

[2] A. Molle, E. R. Berikaa, F. M. Pont, and A. Bande, 'Quantum size effect affecting environment assisted electron capture in quantum confinements', Journal of Chemical Physics **150**, 224105 (2019) 10.1063/1.5095999, tables and figures reprinted with the permission of AIP Publishing.

[3] F. M. Pont, A. Bande, and L. S. Cederbaum, 'Controlled energy-selected electron capture and release in double quantum dots', Phys. Rev. B **88**, 241304(**R**) (2013) 10.1103/PhysRevB.88.241304.

[4] The Royal Swedish Academy of Sciences, *The Nobel Prize in Physics 2001*, https://www.nobelprize.org/prizes/physics/2001/press-release/, Press Release, Stockholm, 9th Oct. 2001.

[5] The Royal Swedish Academy of Sciences, *The Nobel Prize in Physics 1989*, https://www.nobelprize.org/prizes/physics/1989/press-release/, Press Release, Stockholm, 12th Oct. 1989.

[6] M. A. Kastner, 'Artificial atoms', Physics Today **46**, 24–31 (1993) 10.1063/1.881393.

[7] ICD refbase, *Interatomic (intermolecular) coulombic decay and related phenomena*, (2019) https://www.pci.uni-heidelberg.de/tc/usr/icd/ICD.refbase.html (visited on 30/04/2019).

[8] F. M. Pont, A. Bande, and L. S. Cederbaum, 'Electron-correlation driven capture and release in double quantum dots', J. Phys. Condens. Matter **28**, 075301 (2016) 10.1088/0953-8984/28/7/075301.

[9] A. Bande, F. M. Pont, K. Gokhberg, and L. S. Cederbaum, 'Interatomic coulombic electron capture in atomic, molecular, and quantum dot systems', EPJ Web of Conferences **84**, 07002 (2015) 10.1051/epjconf/20158407002.

[10] B. Boudaïffa, P. Cloutier, D. Hunting, M. A. Huels, and L. Sanche, 'Resonant formation of DNA strand breaks by low-energy (3 to 20 eV) electrons', Science **287**, 1658–1660 (2000) 10.1126/science.287.5458.1658.

[11] L. Sanche, 'Interaction of low energy electrons with DNA: applications to cancer radiation therapy', Radiation Physics and Chemistry **128**, 36 (2016) j.radphyschem.2016.05.008.

[12] U. Hergenhahn, 'Production of low kinetic energy electrons and energetic ion pairs by intermolecular coulombic decay', Int. J. Radiat. Biol. **88**, 871 (2012) 10.3109/09553002.2012.698031.

[13] K. Gokhberg, and L. S. Cederbaum, 'Interatomic coulombic electron capture', Phys. Rev. A **82**, 052507 (2010) 10.1103/PhysRevA.82.052707.

[14] M. D. Eisaman, J. Fan, A. Migdall, and S. V. Polyakov, 'Invited review article: single-photon sources and detectors', Rev. Sci. Instrum. **82**, 071101 (2011) 10.1063/1.3610677.

[15] G. Fève, A. Mahé, J.-M. Berroir, T. Kontos, B. Plaçais, D. C. Glattli, A. Cavanna, B. Etienne, and Y. Jin, 'An on-demand coherent single-electron source', Science **316**, 1169–1172 (2007) 10.1126/science.1141243.

[16] Bureau International des Poids et Mesures, 'Resolution 1 on the revision of the international system of units (si)', 26th meeting of the General Conference on Weights and Measures (CGPM) (2018).

[17] J. P. Toennies, A. F. Vilesov, and K. B. Whaley, 'Superfluid helium droplets: an ultracold nanolaboratory', Physics Today **54**, 31–37 (2001) 10.1063/1.1359707.

[18] I. Ferrier-Barbut, 'Ultradilute quantum droplets', Physics Today **72**, 46–52 (2019) 10.1063/pt.3.4184.

[19] C. R. Cabrera, L. Tanzi, J. Sanz, B. Naylor, P. Thomas, P. Cheiney, and L. Tarruell, 'Quantum liquid droplets in a mixture of bose-einstein condensates', Science **359**, 301–304 (2018) 10.1126/science.aao5686.

[20] T. Jahnke, 'Interatomic and intermolecular coulombic decay: the coming of age story', J. Phys. B: At. Mol. Opt. Phys. **48**, 082001 (2015) doi.

[21] N. Sisourat, T. Miteva, J. D. Gorfinkiel, K. Gokhberg, and L. S. Cederbaum, 'Interatomic coulombic electron capture from first principles', Phys. Rev. A Rapid. Comm. **98**, 020701(**R**) (2018) 10.1103/PhysRevA.98.020701.

[22] A. Krükow, A. Mohammadi, A. Härter, and J. Hecker Denschlag, 'Reactive two-body and three-body collisions of Ba^+ in an ultracold rb gas', Phys. Rev. A **94**, 030701 (2016) 10.1103/PhysRevA.94.030701.

[23] T. Sikorsky, Z. Meir, R. Ben-shlomi, N. Akerman, and R. Ozeri, 'Spin-controlled atom-ion chemistry', Nature Communications **9**, 920 (2018) 10.1038/s41467-018-03373-y.

[24] A. Bahrami, M. Müller, M. Drechsler, J. Joger, R. Gerritsma, and F. Schmidt-Kaler, 'Operation of a microfabricated planar ion-trap for studies of a yb+-rb hybrid quantum system', physica status solidi (b) **256**, 1800647 (2019) 10.1002/pssb.201800647.

[25] U. Hergenhahn, 'Interatomic and Intermolecular Coulombic Decay: The Early Years', J. Electron Spectrosc. Relat. Phenom. **184**, 78 (2011) http://dx.doi.org/10.1016/j.elspec.2010.12.020.

[26] E. Alizadeh, T. M. Orlando, and L. Sanche, 'Biomolecular damage induced by ionizing radiation: the direct and indirect effects of low-energy electrons on DNA', Ann. Rev. Phys. Chem. **66**, 379 (2015) 10.1146/annurev-physchem-040513-103605.

[27] H. H. Mitchell, T. S. Hamilton, F. R. Steggerda, and H. W. Bean, 'The chemical composition of the adult human body and its bearing on the biochemistry of growth', Journal of Biological Chemistry **158**, 625–637 (1945).

[28] R. M. Forbes, H. H. Mitchell, and A. R. Cooper, 'Further studies on the gross composition and mineral elements of the adult human body', Journal of Biological Chemistry **223**, 969–975 (1956).

[29] R. H. Dicke, 'Coherence in spontaneous radiation processes', Phys. Rev. **93**, 99–110 (1954) 10.1103/PhysRev.93.99.

[30] M. Gross, and S. Haroche, 'Superradiance: an essay on the theory of collective spontaneous emission', Physics Reports **93**, 301–396 (1982).

[31] J. D. Bekenstein, and M. Schiffer, 'The many faces of superradiance', Phys. Rev. D **58**, 064014 (1998) 10.1103/PhysRevD.58.064014.

[32] M. Scheibner, T. Schmidt, L. Worschech, A. Forchel, G. Bacher, T. Passow, and D. Hommel, 'Superradiance of quantum dots', Nature Physics **3**, 106 (2007) 10.1038/nphys494.

[33] R. Friedberg, and S. Hartmann, 'Superradiant damping and absorption', Physics Letters A **37**, 285–286 (1971) 10.1016/0375-9601(71)90672-4.

[34] S. Yi, M. Zhou, Z. Wang, and Z. Yu, 'Superradiant absorption in multiple optical nanoresonators', Physical Review B **89** (2014) 10.1103/physrevb.89.195449.

[35] M. Maragkou, 'Superabsorption', Nature Photonics **8**, 813–813 (2014) 10.1038/nphoton.2014.265.

[36] H. Gleiter, 'Nanostructured materials: basic concepts and microstructure', Acta Materialia **48**, 1–29 (2000) 10.1016/s1359-6454(99)00285-2.

[37] J. Jeevanandam, A. Barhoum, Y. S. Chan, A. Dufresne, and M. K. Danquah, 'Review on nanoparticles and nanostructured materials: history, sources, toxicity and regulations', Beilstein Journal of Nanotechnology **9**, 1050–1074 (2018) 10.3762/bjnano.9.98.

[38] J. P. Reithmaier, P. Petkov, W. Kulisch, and C. Popov, eds., *Nanostructured materials for advanced technological applications* (Springer Netherlands, 2009), 10.1007/978-1-4020-9916-8.

[39] G. Moore, 'Moore's law at 40', in *Understanding moore's law: four decades of innovation*, edited by D. Brock, (Chemical Heritage Foundation, location, 2006) Chap. 7, pp. 67–84.

[40] P. H. Lewis, 'The executive computer; the race to market a 486 machine', New York Times, 003010 (1989).

[41] W. Lambrechts, S. Sinha, J. A. Abdallah, and J. Prinsloo, *Extending moore's law through advanced semiconductor design and processing techniques* (CRC Press / Taylor and Francis Group, Boca Raton, 2019).

[42] S. Natarajan, M. Agostinelli, S. Akbar, M. Bost, A. Bowonder, V. Chikarmane, S. Chouksey, A. Dasgupta, K. Fischer, Q. Fu, T. Ghani, M. Giles, S. Govindaraju, R. Grover, W. Han, D. G. Hanken, E. Haralson, M. Haran, M. Heckscher, R. Heussner, P. Jain, R. James, R. Jhaveri, I. Jin, H. Kam, E. Karl, C. L. Kenyon, M. Y. Liu, Y. Luo, R. Mehandru, S. Morarka, L. Neiberg, P. Packan, A. Paliwal, C. Parker, P. Patel, R. Patel, C. Pelto, L. C. Pipes, P. Plekhanov, M. Prince, S. Rajamani, J. Sandford, B. Sell, S. Sivakumar, P. Smith, B. Song, K. Tone, T. Tröger, J. Wiedemer, M. Yang, and K. Zhang, 'A 14nm logic technology featuring 2nd-generation finfet, air-gapped interconnects, self-aligned double patterning and a 0.0588 μm^2 sram cell size', IEEE International Electron Devices Meeting (IEDM), 3.7.1 (2014).

[43] A. Kelly, and M. Wyman, *Apple introduces iphone xr*, (12th Sept. 2018) https://www.apple.com/newsroom/2018/09/apple-introduces-iphone-xr/ (visited on 21/02/2019), Press Release.

[44] Huawei Technologies Co., Ltd., ed., *Title*, (31st Aug. 2018) https://consumer.huawei.com/en/press/news/2018/huawei-launches-kirin-980-the-first-commercial-7nm-soc/ (visited on 21/02/2019).

[45] S. Datta, 'Ten nanometre cmos logic technology', Nature Electronics **1**, Through some unconventional approaches to improving transistor density and performance, the latest logic technology from Intel delivers 100 million transistors per square millimetre ? and in the process, reaffirms Moore?s law., 500 (2018) 10.1038/s41928-018-0137-6.

[46] E. Vogel, 'Technology and metrology of new electronic materials and devices', Nature Nanotechnology **2**, Review Article, 25 (2007) 10.1038/nnano.2006.142.

[47] F. Kuemmeth, K. I. Bolotin, S.-F. Shi, and D. C. Ralph, 'Measurement of discrete energy-level spectra in individual chemically synthesized gold nanoparticles', Nano Lett. **8**, 4506–4512 (2008) 10.1021/nl802473n.

[48] L. Brus, 'Electronic wave functions in semiconductor clusters: experiment and theory', J . Phys. Chem. **90**, 2555–2560 (1986).

[49] R. Rossetti, J. L. Ellison, J. M. Gibson, and L. E. Brus, 'Size effects in the excited electronic states of small colloidal cds crystallites', J. Chem. Phys. **80**, 4464 (1984) 10.1063/1.447228.

[50] A. P. Alivisatos, 'Perspectives on the physical chemistry of semiconductor nanocrystals', J. Phys. Chem. **100**, 13226 (1996) 10.1021/jp9535506.

[51] A. P. Alivisatos, 'Semiconductor clusters, nanocrystals, and quantum dots', Science **271**, 933 (1996).

[52] M. Mansuripur, 'The role of nano-technology in data storage devices and systems', Nonlinear Optics, OMA2 (2011) 10.1364/ISOM_ODS.2011.OMA2.

[53] H.-W. Chen, J.-H. Lee, B.-Y. Lin, S. Chen, and S.-T. Wu, 'Liquid crystal display and organic light-emitting diode display: present status and future perspectives', Light-Sci. Appl. **7**, 17168 (2018) 10.1038/lsa.2017.168.

[54] N. N. Ledentsov, 'Quantum dot laser', Semicond. Sci. Technol. **26**, 014001 (2011).

[55] Z. Qian, S. Kang, V. Rajaram, C. Cassella, N. E. McGruer, and M. Rinaldi, 'Zero-power infrared digitizers based on plasmonically enhanced micromechanical photoswitches', Nature Nanotech. **12**, 969 (2017) 10.1038/nnano.2017.147.

[56] F. Meinardi, H. McDaniel, F. Carulli, A. Colombo, K. A. Velizhanin, N. S. Makarov, R. Simonutti, V. I. Klimov, and S. Brovelli, Nature Nanotech. **10**, 878 (2015).

[57] N. Singh, A. Agarwal, L. K. Bera, T. Y. Liow, R. Yang, S. C. Rustagi, C. H. Tung, R. Kumar, G. Q. Lo, N. Balasubramanian, and D. .-.-. Kwong, 'High-performance fully depleted silicon nanowire (diameter /spl les/ 5 nm) gate-all-around cmos devices', IEEE Electron Device Letters **27**, 383–386 (2006) 10.1109/LED.2006.873381.

[58] R. Huang, R. Wang, J. Zhuge, C. Liu, T. Yu, L. Zhang, X. Huang, Y. Ai, J. Zou, Y. Liu, J. Fan, H. Liao, and Y. Wang, 'Characterization and analysis of gate-all-around si nanowire transistors for extreme scaling', in 2011 ieee custom integrated circuits conference (cicc) (Sept. 2011), pp. 1–8, 10.1109/CICC.2011.6055334.

[59] D. B. Suyatin, V. Jain, V. A. Nebol?sin, J. Trägårdh, M. E. Messing, J. B. Wagner, O. Persson, R. Timm, A. Mikkelsen, I. Maximov, L. Samuelson, and H. Pettersson, 'Strong schottky barrier reduction at au-catalyst/gaas-nanowire interfaces by electric dipole formation and fermi-level unpinning', Nature Communications **5**, 3221 (2014) 10.1038/ncomms4221.

[60] R. Leturcq, C. Stampfer, K. Inderbitzin, L. Durrer, C. Hierold, E. Mariani, M. G. Schultz, F. von Oppen, and K. Ensslin, Nature Phys. **5**, 327 (2009).

[61] J. Salfi, S. Roddaro, D. Ercolani, L. Sorba, I. Savelyev, M. Blumin, H. E. Ruda, and F. Beltram, 'Electronic properties of quantum dot systems realized in semiconductor nanowires', Semicond. Sci. Technol. **25**, 024007 (2010) 10.1088/0268-1242/25/2/024007.

[62] S. Roddaro, A. Pescaglini, D. Ercolani, L. Sorba, and F. Beltram, 'Manipulation of electron orbitals in hard-wall InAs/InP nanowire quantum dots.', Nano Lett. **11**, 1695 (2011).

[63] W. G. van der Wiel, S. De Franceschi, J. M. Elzerman, T. Fujisawa, S. Tarucha, and L. P. Kouwenhoven, 'Electron transport through double quantum dots', Rev. Mod. Phys. **75**, 1 (2002) 10.1103/RevModPhys.75.1.

[64] F. M. Pont, A. Molle, E. R. Berikaa, S. Bubeck, and A. Bande, 'Predicting the performance of the inter-Coulombic electron capture from single-electron quantities', Journal of Physics: Condensed Matter **32**, 065302 (2019) 10.1088/1361-648x/ab41a9.

[65] L. S. Cederbaum, J. Zobeley, and F. Tarantelli, 'Giant intermolecular decay and fragmentation of clusters', Phys. Rev. Lett. **79**, 4778–4781 (1997) 10.1103/PhysRevLett.79.4778.

[66] U. Hergenhahn, 'Interatomic and Intermolecular Coulombic Decay: The Early Years', J. Electron Spectrosc. Relat. Phenom. **184**, 78 (2011) 10.1016/j.elspec.2010.12.020.

[67] R. A. Wilhelm, E. Gruber, J. Schwestka, R. Kozubek, T. I. Madeira, J. P. Marques, J. Kobus, A. V. Krasheninnikov, M. Schleberger, and F. Aumayr, 'Interatomic Coulombic Decay: The Mechanism for Rapid Deexcitation of Hollow Atoms', Phys. Rev. Lett. **119**, 103401 (2017) 10.1103/PhysRevLett.119.103401.

[68] A. C. LaForge, M. Shcherbinin, F. Stienkemeier, R. Richter, R. Moshammer, T. Pfeifer, and M. Mudrich, 'Highly efficient double ionization of mixed alkali dimers by intermolecular Coulombic decay', Nature Phys. **15**, 247 (2019) 10.1038/s41567-018-0376-5.

[69] X. Ren, E. Wang, A. D. Skitnevskaya, A. B. Trofimov, K. Gokhberg, and A. Dorn, 'Experimental evidence for ultrafast intermolecular relaxation processes in hydrated biomolecules', Nature Phys. **14**, 1062 (2018) 10.1038/s41567-018-0214-9.

[70] S. Xu, D. Guo, X. Ma, X. Zhu, W. Feng, S. Yan, D. Zhao, Y. Gao, S. Zhang, X. Ren, Y. Zhao, Z. Xu, A. Dorn, L. S. Cederbaum, and N. V. Kryzhevoi, 'Damaging Intermolecular Energy and Proton Transfer Processes in Alpha-Particle-Irradiated Hydrogen-Bonded Systems', Angew. Chem. Int. Ed. **57**, 17023 (2018) http://dx.doi.org/10.1002/anie.201808898.

[71] V. Averbukh, and L. S. Cederbaum, 'Interatomic Electronic Decay in Endohedral Fullerenes', Phys. Rev. Lett. **96**, 4, 053401 (2006) http://dx.doi.org/10.1103/PhysRevLett.96.053401.

[72] A. Bande, K. Gokhberg, and L. S. Cederbaum, 'Dynamics of interatomic coulombic decay in quantum dots', J. Chem. Phys. **135**, 144112 (2011) 10.1063/1.3646205.

[73] I. Cherkes, and N. Moiseyev, 'Electron relaxation in quantum dots by the interatomic coulombic decay mechanism', Phys. Rev. B **83**, 113303 (2011).

[74] A. Bande, F. M. Pont, P. Dolbundalchok, K. Gokhberg, and L. S. Cederbaum, 'Dynamics of interatomic coulombic decay in quantum dots: singlet initial state', EPJ Web Conf. **41**, 04031 (2013).

[75] T. Goldzak, L. Gantz, I. Gilary, G. Bahir, and N. Moiseyev, 'Interatomic coulombic decay in two coupled quantum wells', Phys. Rev. B **91**, 165312 (2015) 10.1103/PhysRevB.91.165312.

[76] T. Goldzak, L. Gantz, I. Gilary, G. Bahir, and N. Moiseyev, 'Vertical currents due to interatomic Coulombic decay in experiments with two coupled quantum wells', Phys. Rev. B **93**, 045310 (2016) http://dx.doi.org/10.1103/PhysRevB.93.045310.

[77] P. Dolbundalchok, D. Peláez, E. F. Aziz, and A. Bande, 'Geometrical control of the interatomic coulombic decay process in quantum dots for infrared photodetectors', J. Comput. Chem. **37**, 2249–2259 (2016) 10.1002/jcc.24410.

[78] F. Weber, E. F. Aziz, and A. Bande, 'Interdependence of icd rates in paired quantum dots on geometry', Journal of Computational Chemistry **38**, 2141 (2017) 10.1002/jcc.24843.

[79] P. R. Brooks, and E. F. Hayes, eds., *State-to-state chemistry* (AMERICAN CHEMICAL SOCIETY, June 1977), 10.1021/bk-1977-0056.

[80] J. Wolf, M. Deiß, A. Krükow, E. Tiemann, B. P. Ruzic, Y. Wang, J. P. D'Incao, P. S. Julienne, and J. H. Denschlag, 'State-to-state chemistry for three-body recombination in an ultracold rubidium gas', Science **358**, 921–924 (2017) 10.1126/science.aan8721.

[81] M. Faraday, 'VIII. experimental researches in electricity. — thirteenth series', Philosophical Transactions of the Royal Society of London **128**, 125–168 (1838) 10.1098/rstl.1838.0009.

[82] A. Kramida, Yu. Ralchenko, J. Reader, and and NIST ASD Team, NIST Atomic Spectra Database (ver. 5.6.1), [Online]. Available: https://physics.nist.gov/asd [2019, September 25]. National Institute of Standards and Technology, Gaithersburg, MD. 2018, https://doi.org/10.18434/T4W30F.

[83] J. E. Sansonetti, 'Wavelengths, transition probabilities, and energy levels for the spectra of rubidium (Rb I through Rb XXXVII)', Journal of Physical and Chemical Reference Data **35**, 301–421 (2006) 10.1063/1.2035727.

[84] J. J. Curry, 'Compilation of wavelengths, energy levels, and transition probabilities for Ba I and Ba II', Journal of Physical and Chemical Reference Data **33**, 725–746 (2004) 10.1063/1.1643404.

[85] N. V. Kryzhevoi, V. Averbukh, and L. S. Cederbaum, 'High activity of helium droplets following ionization of systems inside those droplets', Phys. Rev. B **76**, 094513 (2007) 10.1103/PhysRevB.76.094513.

[86] R. Jones, 'Density functional theory: its origins, rise to prominence, and future', Reviews of Modern Physics **87**, 897–923 (2015) 10.1103/revmodphys.87.897.

[87] W. Kohn, 'Nobel lecture: electronic structure of matter — wave functions and density functionals', Reviews of Modern Physics **71**, 1253–1266 (1999) 10.1103/revmodphys.71.1253.

[88] A. J. Cohen, P. Mori-Sánchez, and W. Yang, 'Challenges for density functional theory', Chemical Reviews **112**, 289–320 (2011) 10.1021/cr200107z.

[89] J. Tennyson, 'Electron-molecule collision calculations using the R-matrix method', Physics Reports **491**, 29 (2010) 10.1016/j.physrep.2010.02.001.

[90] H.-D. Meyer, U. Manthe, and L. S. Cederbaum, 'The multi-configurational time-dependent hartree approach', Chem. Phys. Letters **165**, 73 (1990).

[91] U. Manthe, H.-D. Meyer, and L. S. Cederbaum, 'Wave-packet dynamics within the multiconfiguration hartree framework: general aspects and application to nocl', J. Chem. Phys. **97**, 3199 (1992).

[92] M. H. Beck, A. Jäckle, G. A. Worth, and H.-D. Meyer, 'The multiconfiguration time-dependent hartree (mctdh) method: a highly efficient algorithm for propagating wavepackets', Phys. Reports **324**, 1 (2000).

[93] H.-D. Meyer, F. Gatti, and G. A. Worth, eds., *Multidimensional quantum dynamics* (Wiley-VCH, Weinheim, 2009).

[94] R. P. Feynman, R. B. Leighton, and M. Sands, *The Feynman lectures on physics*, The New Millennium Edition 2011, Vol. III: Quantum Mechanics (Basic Books, New York, 1965).

[95] T. Lancaster, and S. J. Blundell, *Quantum field theory for the gifted amateur*, Reprinted 2018 (with corrections) (Oxford University Press, Oxford, 2014).

[96] H. Kleinert, *Particles and quantum fields* (World Scientific, Nov. 2015), 10.1142/9915.

[97] D. E. Weeks, and D. J. Tannor, 'A time-dependent formulation of the scattering matrix using møller operators', Chemical Physics Letters **207**, 301–308 (1993) 10.1016/0009-2614(93)89004-2.

[98] C. Cohen-Tannoudji, B. Diu, and F. Laloë, *Quantenmechanik*, 4. Auflage 2009 (Walter de Gruyter, Berlin, 1977).

[99] I. N. Bronstein, K. A. Semendjajew, G. Musiol, and H. Mühlig, *Taschenbuch der Mathematik*, 5. Auflage (Verlag Harri Deutsch, Frankfurt (Main), 2001).

[100] *NIST Digital Library of Mathematical Functions*, http://dlmf.nist.gov/, Release 1.0.21 of 2018-12-15, F. W. J. Olver, A. B. Olde Daalhuis, D. W. Lozier, B. I. Schneider, R. F. Boisvert, C. W. Clark, B. R. Miller and B. V. Saunders, eds.

[101] G. Wentzel, 'Eine verallgemeinerung der quantenbedingungen für die zwecke der wellenmechanik', Zeitschrift für Physik **38**, 518–529 (1926) 10.1007/BF01397171.

[102] H. A. Kramers, 'Wellenmechanik und halbzahlige quantisierung', Zeitschrift für Physik **39**, 828–840 (1926) 10.1007/BF01451751.

[103] L. Brillouin, 'La mécanique ondulatoire de schrödinger: une méthode générale de resolution par approximations successives', Comptes Rendus de l'Académie des Sciences **183**, 24–26 (1926).

[104] H. Jeffreys, 'On certain approximate solutions of linear differential equations of the second order', Proceedings of the London Mathematical Society **23**, 428–436 (1924) 10.1112/plms/s2-23.1.428.

[105] J. Liouville, 'Sur le développement des fonctions et séries', Journal de Mathématiques Pures et Appliquées **1**, 16–35 (1837).

[106] G. Green, 'On the motion of waves in a variable canal of small depth and width', Transactions of the Cambridge Philosophical Society **6**, 457–462 (1837).

[107] B. C. Hall, 'The wkb approximation', in *Quantum theory for mathematicians* (Springer New York, New York, NY, 2013), pp. 305–331, 10.1007/978-1-4614-7116-5_15.

[108] J. Jackson, *Classical electrodynamics*, 5. überarb. Auflage 2014 (de Gruyter, Berlin, 1999).

[109] L. D. Landau, and E. M. Lifshitz, *Quantum mechanics – non-relativistic theory*, Second edition, revised and enlarged (Pergamon Press, Oxford, 1965).

[110] M. Abramowitz, and I. A. Stegun, *Handbook of mathematical functions, With formulas, graphs, and mathematical tables*, Tenth Printing, December 1972, with corrections (National Bureau of Standards, Washington, D.C., 1964).

[111] P. Fuentealba, 'On the reliability of semiempirical pseudopotentials: dipole polarisability of the alkali atoms', Journal of Physics B: Atomic and Molecular Physics **15**, L555–L558 (1982) 10.1088/0022-3700/15/16/002.

[112] J. Adamowski, M. Sobkowicz, B. Szafran, and S. Bednarek, 'Electron pair in a gaussian confining potential', Physical Review B **62**, 4234–4237 (2000) 10.1103/physrevb.62.4234.

[113] B. Szafran, S. Bednarek, and J. Adamowski, 'Parity symmetry and energy spectrum of excitons in coupled self-assembled quantum dots', Physical Review B **64** (2001) 10.1103/physrevb.64.125301.

[114] S. Bednarek, B. Szafran, T. Chwiej, and J. Adamowski, 'Effective interaction for charge carriers confined in quasi-one-dimensional nanostructures', Phys. Rev. B **68**, 045328 (2003) 10.1103/PhysRevB.68.045328.

[115] R. Kosloff, and D. Kosloff, 'Absorbing boundaries for wave propagation problems', J. Comput. Phys. **63**, 363 (1986) 10.1016/0021-9991(86)90199-3.

[116] D. Neuhauser, and M. Baer, 'The time-dependent schrödinger equation: application of absorbing boundary conditions', J. Chem. Phys. **90**, 4351 (1989) 10.1063/1.456646.

[117] U. V. Riss, and H.-D. Meyer, 'Calculation of resonance energies and widths using the complex absorbing potential method', J. Phys. B: At. Mol. Opt. Phys. **26**, 4503 (1993) 10.1088/0953-4075/26/23/021.

[118] U. V. Riss, and H.-D. Meyer, 'Investigation on the reflection and transmission properties of complex absorbing potentials', J. Chem. Phys. **105**, 1409 (1996) 10.1063/1.472003.

[119] M. Jones, M. Harvey, W. Bertsche, G. Xia, S. Chattopadhyay, A. J. Murray, and R. Appleby, 'The AC-MOT cold atom electron source (CAES)', Journal of Physics: Conference Series **875**, 052020 (2017) 10.1088/1742-6596/875/6/052020.

[120] P. Fuentealba, L. von Szentpaly, H. Preuss, and H. Stoll, 'Pseudopotential calculations for alkaline-earth atoms', Journal of Physics B: Atomic and Molecular Physics **18**, 1287–1296 (1985) 10.1088/0022-3700/18/7/010.

[121] M. H. Beck, A. Jäckle, G. A. Worth, and H.-D. Meyer, 'The multiconfiguration time-dependent hartree (mctdh) method: a hichly efficient algorithm for propagating wavepackets', Phys. Rev. **324**, 1 (2000).